The Impact of Saharan Dust on the North Atlantic Circulation

Dissertation

Zur Erlangung des Doktorgrades der Naturwissenschaften
im Department Geowissenschaften
der Universität Hamburg.

vorgelegt von

Nidia Martínez Avellaneda

aus
Buenos Aires, Argentinien

Hamburg
2010

Universität Hamburg

Als Dissertation angenommen vom Department Geowissenschaften der Universität Hamburg

Auf Grund der Gutachten von Prof. Dr. Detlef Stammer
und Prof. Dr. Hartmut Graßl

Hamburg, den 03. Februar 2010

Prof. Dr. Oßenbrügge
Leiter des Department Geowissenschaften

Abstract

The erosion of Saharan soil is the World's largest annual source of mineral dust aerosols, resulting in a deposition of more than 40% of the global atmospheric dust into the North Atlantic. By changing the atmospheric opacity, mineral dust can alter the shortwave radiative forcing at the surface of the ocean, altering the ocean mixed layer heat budget and therefore affecting the sea surface temperature (SST), which plays an important role in the regional and global climate. Moreover, changes of the total amount of energy received at the ocean surface have an impact on the ocean circulation.

In this thesis we combine several satellite observations, in-situ radiation measurements, a one-dimensional mixed layer model of the ocean, and various versions of a three-dimensional general ocean circulation model, to study the impact of Saharan dust on the circulation and transport of properties in the North Atlantic. A buoyancy source generated by realistic dust-induced shortwave flux anomalies is imposed in the eastern North Atlantic and the differences between this simulation and an unperturbed one are investigated in terms of the ocean dynamical adjustment and changes in the Atlantic Meridional Overturning Circulation (AMOC) and Meridional Heat Transport (HT).

A joint analysis of aerosol optical depth retrievals from the MODIS sensor and SST from the TMI sensor for the period 2000-2006 shows a decrease in SST of 0.2°to 0.4°C simultaneously with, or shortly after, strong dust outbreaks, which is consistent with an independent estimate of SST decrease simulated by a local 1D mixed layer model. A comparison between observed TMI SST fields and simulated SSTs with an eddy-permitting model of the North Atlantic suggests a local cooling of about 0.5°C on sub-seasonal to interannual time-scales. A regression analysis suggests that about 9% of SST variance could be explained by dust-induced cooling in this region which is not represented in existing AVHRR sensor SST fields nor represented in surface heat fluxes from current atmospheric reanalyses, with which the model was forced. Results of the 3D eddy-permitting simulations show that an advection of the ocean properties ocurs in response to the buoyancy source in the eastern subtropical North Atlantic. These ocean anomalous signals are generally advected by eddies that arise from the instability of ocean currents. Their spatial pattern depends on the ocean local density structure, the time/space distribution of dust and the mean circulation in the Atlantic. The anomalies leave the perturbed area and take part in the equatorial circulation. The eddies and baroclinic instabilities present in the ocean advect the signal towards the west and back towards the east reaching the easternmost part of the original perturbed area in 10 months. Once they have reached the African coast at about 20°N, they trigger westward propagating Rossby waves. As a result of a realistic dust-induced perturbation in the shortwave flux in the subtropical eastern North Atlantic, the time-mean differences of AMOC between the perturbed and unperturbed simulations show an increased meridional transport at 38°N and 43°N of 0.55 and 0.45 Sv, respectively, and a decreased AMOC at 40°N and 45°N of 0.2 Sv. We observe a decrease of the total time-mean HT of 7 TW between

10°N and 35°N, which is a result of the balance between a decrease in the overturning component of 15 TW and an increase of the horizontal gyre component of 8 TW. The total HT is observed to increase everywhere else.

In addition, we have shown changes in the amplitude of ocean properties and generation of westward propagating Rossby waves off the African coast, which are triggered by the anomalous signals generated on the east that are advected by the existing eddies following the main circulation path. We conclude that the effect of Saharan dust should be incorporated in ocean numerical simulations, specially under the frame of climate change studies when a changing dust load of the atmosphere in response to a changing climate could be possible.

KEYWORDS: Saharan dust, SST, SSH, aerosol radiative forcing, North Atlantic circulation, Rossby waves, AMOC, meridional heat transport, ocean modeling.

Contents

Chapter 1

Introduction

Mineral dust and aerosols originating from wind-induced erosion of soil in arid regions can impact the climate system in many ways, e.g., by altering weather or by affecting atmospheric chemistry. As an example, mineral dust and the very dry Saharan Air Layer (SAL), with which it is associated, have been shown to affect the development of clouds and precipitation, as well as modulating thunderstorm activities and tropical cyclogenesis (*Sassen et al.*, 2003; *Dunion and Velden*, 2004; *Yoshioka et al.*, 2007; *Wu*, 2007; *Evan et al.*, 2008). Mineral dust, in particular, by increasing the attenuation (scattering and absorption) of solar radiation in the atmosphere, leads to a redistribution of radiative heating from the surface upward into the dust layer (e.g., *Miller and Tegen*, 1999) and to a decreased shortwave irradiance at sea level. By changing the atmospheric opacity, mineral dust can thus alter the shortwave radiative forcing at the surface of the ocean (*Jickells et al.*, 2005; *Evan et al.*, 2009); in addition, thermal emissions from dust aerosols can increase the surface longwave forcing (*Vogelmann et al.*, 2003; *Zhu et al.*, 2007). Both processes play a role in the ocean mixed layer heat budget and can therefore affect the climatologically important sea surface temperature (SST).

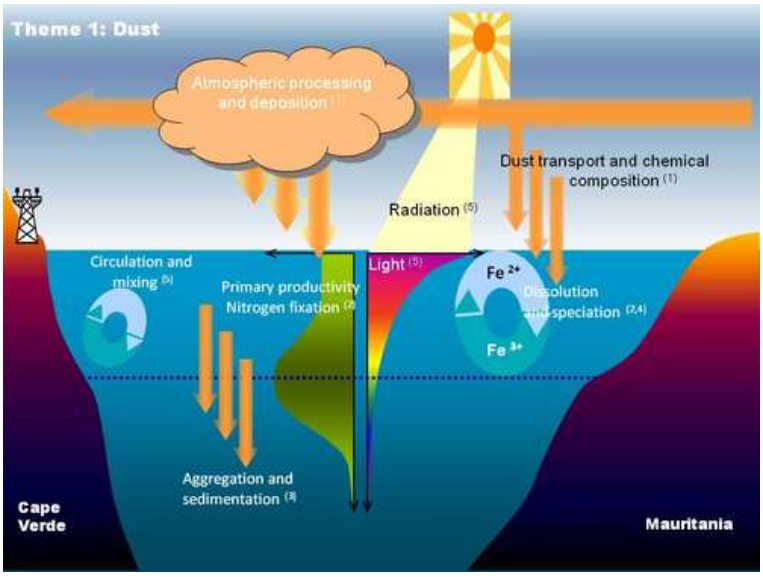

Figure 1.1: Schematic of the biogeochemical and physical response to dust deposition from the project "Surface Ocean Processes in the Anthropocene (SOPRAN)" (SOPRAN proposal, unpublished, 2006).

In principle, the ocean circulation and transport properties can also change in response to enhanced mineral dust or aerosol concentrations. The inhomogeneous distribution of dust aerosols in the atmosphere will lead to a differential heating at the surface. As a result, horizonal gradients of density would be generated, which in turn would change the ocean currents and ultimately, the ocean circulation (*Marzeion et al.*, 2005).

Moreover, once settled to the oceans surface, mineral dust can act as a fertilizer, either directly or via stimulation of nitrogen fixation (*Mills et al.*, 2004; *Moore et al.*, 2009), and potentially can enhance biological productivity and thereby potentially can change the composition of phytoplankton (*Erickson et al.*, 2003; *Coale*, 2004; *Boyd*, 2007; *Blain et al.*, 2007). Changes in productivity can, in turn, feed back on the atmosphere through altered trace gas emissions. Hence atmospheric impacts on the ocean represent Earth System linkages with potentially major implications for future atmospheric CO2 levels, marine ecosystem behaviour and atmospheric chemistry. See Fig. 1.1 for a schematic representation.

As compared to the rest of the World, the erosion of the Saharan soil is by far the largest annual source of mineral dust aerosols (*Prospero et al.*, 2002; *Washington et al.*, 2003). Fig. 1.2 shows the distribution of the dust fluxes to the Earth surface published by *Jickells et al.* (2005). The figure is based on a composite of three published modeling studies that match satellite aerosol optical depth, *in-situ* concentrations, and deposition observations of dust (*Ginoux et al.*, 2001; *Mahowald and Luo*, 2003; *Tegen et al.*, 2004) and appears to match observations well. The dust inputs to the oceans result in a deposition of more than 40% (200-260 $Tg\ yr^{-1}$) of the global dust into the North Atlantic Ocean (see also, *Kaufman et al.*, 2005; *Mahowald et al.*, 2005, and references therein). Dust transport over the ocean affects atmospheric radiation transfer and hence the quantity and quality of light entering the surface ocean.

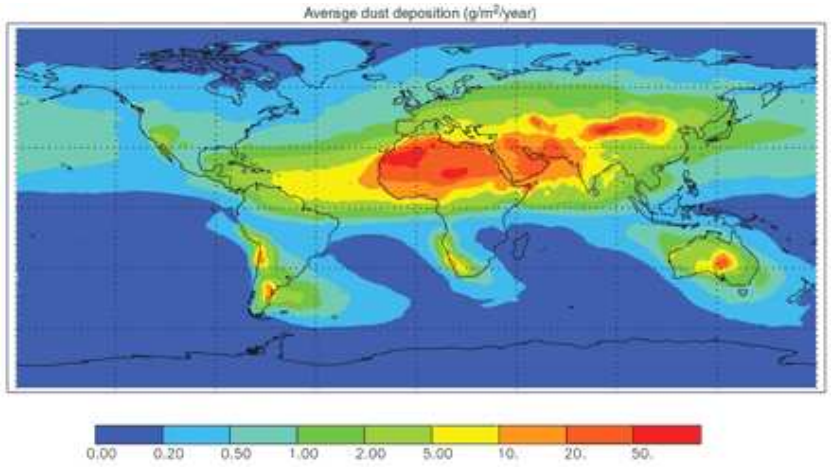

Figure 1.2: Dust fluxes to the world oceans from *Jickells et al.* (2005). Total atmospheric dust inputs to the oceans = 450 Tg $year^{-1}$. Percentage inputs to ocean basins based on this figure are as follows: North Atlantic, 43%; South Atlantic, 4%; North Pacific, 15%; South Pacific, 6%; Indian Ocean, 25%; and Southern Ocean, 6%.

There is plenty of bibliography describing the properties of Saharan dust (see for ex-

ample *Schepanski et al.*, 2009a, and references therein). What matters to this work are its seasonality and its storms/outbreaks, which are also in close relation with its horizontal distribution. Fig. 1.3 shows an example of a dust plume over the Sahara Desert and expanding over the Atlantic Ocean and Canary Islands, from the Total Ozone Mapping Spectrometer (TOMS[1]). The land sources of this dust plume are clearly visible, with the main source coming from Western Sahara, Mauritania and the Sahel. There are several potential inland source areas for the dust over the ocean. These areas show seasonal changes dust source activity that are related to seasonal changes in meteorological conditions (*Schepanski et al.*, 2009b). For example, the Bodélé depression is the most active source during winter and accounts for up to 50% of the dust found in the Cape Verde archipelago (*Koren et al.*, 2006; *Schepanski et al.*, 2009a) During the dust transport towards the Atlantic Ocean, the dust plume can remain near the surface and be observed as a dust storm (Fig. 1.3), or can be transported as elevated layer (*Kalu*, 1979). The elevation of the dust layers in turn, depends on the season. In winter/spring the dust transport occurs mostly in near-surface layers, while in summer the transport is at higher layers. Remote sensing retrievals can be used to determine dust fluxes into the North Atlantic. The Aerosol Optical Depth (AOD) is a measure of the degree to which aerosols prevent the transmission of light. It is a measure of radiation extinction due to aerosol scattering and absorption and is available at different spectral bands from different instruments. We use here AOD at 550 *nm* from the Moderate Resolution Imaging Spectroradiometer (MODIS[2], more details are provided in Chapter 2). While AOD values of 0.2 correspond to a clear day, for AOD values of about 4 one would have difficulty seeing the sun in the middle of the day.

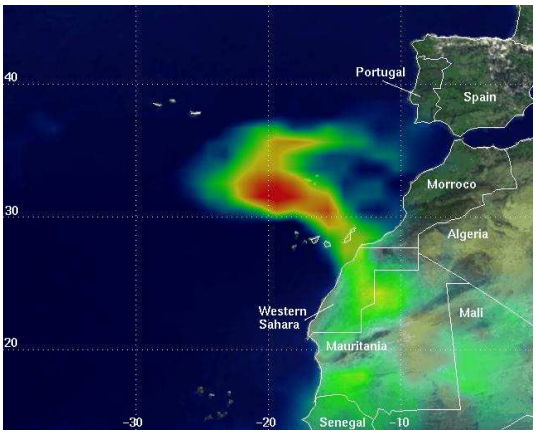

Figure 1.3: Aerosol Index (AI) distribution in the eastern North Atlanic, from February 26, 2000, obtained from the Total Ozone Mapping Spectrometer (TOMS). The green to red false colors represent increasing amounts of aerosol. The AI is an adimensional quantity.

The time-mean distribution of MODIS AOD averaged over the period 2000-2006 for the summer months and the winter months of the northern hemisphere displayed in

[1]http://jwocky.gsfc.nasa.gov/aerosols/africa/canary.html
[2]http://gdata1.sci.gsfc.nasa.gov/daac-bin/G3/gui.cgi?instance_id=MODIS_DAILY_L3

Fig. 1.4, shows obvious differences in amplitude and in the horizontal path between the seasons. We can identify: 1) the high-dust summer plume located between 15° N and 25° N, and 2) the low-dust winter plume extending between 5° S and 15° N. The Saharan dust's annual variability is even more obvious from the time series taken right off the African coast shown in Fig. 1.4c. Superposed to the seasonal variability of the dust, are the dust outbreaks. These are characterized by high concentrations of dust in the atmosphere lasting over a short period, from only a couple of days up to one week. The Saharan dust outbreaks over the North Atlantic are usually seen right off the African Coast from the Cape Verde archipelago up to 35° N (see Fig. 1.3 as an example).

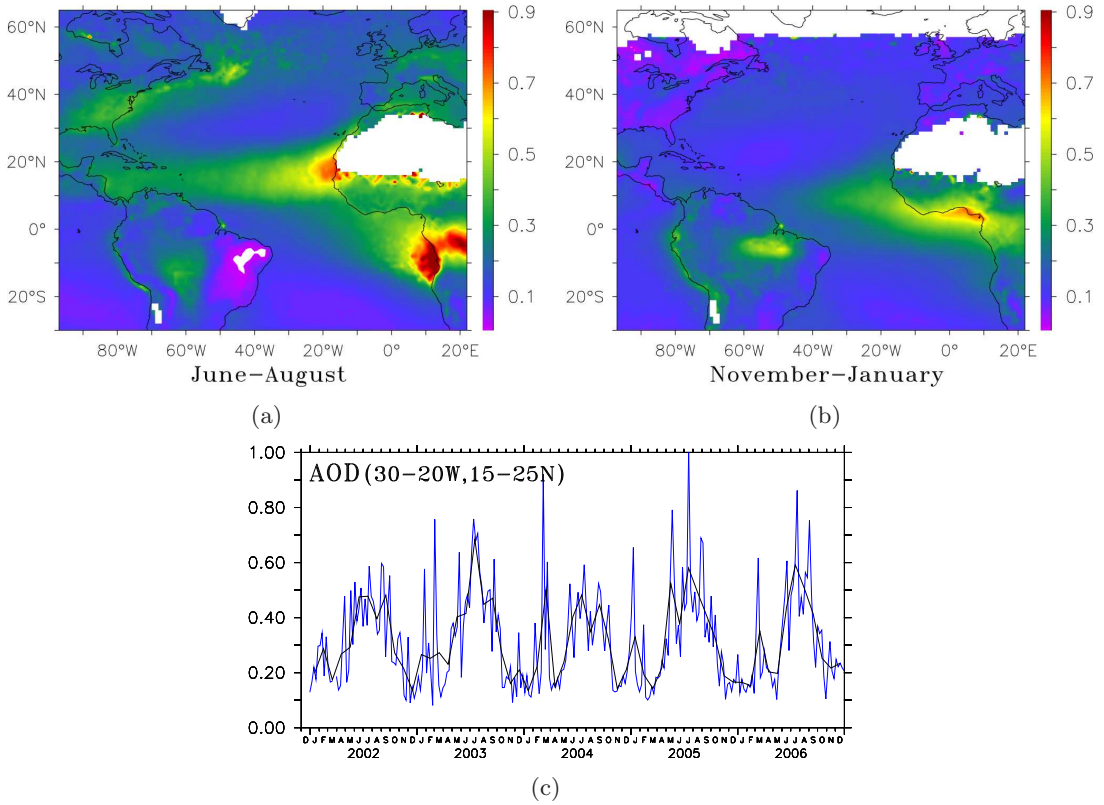

Figure 1.4: Mean geographical distribution of MODIS Aerosol Optical Depth (2000-2006) for (a) the high-dust months June/July/August, (b) the low-dust months November/December/January and (c) time series of weekly AOD (in blue) jointly with monthly means (in black), for the period 2002 - 2006, averaged over 30° W - 20° W; 15° N - 25° N. The white areas correspond to values of AOD outside the color scale.

Hot dry Saharan air, known as the Sahara Air Layer (SAL), can be traced far over the western Atlantic (*Prospero and Carlson*, 1981; *Colarco et al.*, 2003) and associated with this layer are often enhanced concentrations of mineral dust. As an example, *Lau and Kim* (2007) reported a significant increase in Saharan dust over the western North Atlantic during 2006 and argued that this enhanced dust concentration might have been responsible for a cooling of the ocean's surface there, during the same year, by scattering

more solar radiation to space and depriving the surface of some solar heating.

The combined effects of the inhomogeneous distribution of dust in the atmosphere, and the dust-induced cooling in the eastern subtropical North Atlantic, can generate local sub-surface density gradients which, through the thermal wind relation, can result in a changed circulation. In principle, changes from a sub-basin to a basin scale could be possible.

In addition, a cooling in the subtropical eastern North Atlantic can act as a buoyancy source for changes in the transport of mass and heat in the Atlantic. *Köhl* (2005) investigated the mechanisms and controlling regions that influence the Atlantic Meridional Overturning Circulation (AMOC) by using adjoint sensitivities. The author found the AMOC to be sensitive to anomalies in the eastern part of the Atlantic and, moreover, that changes in temperature, salinity and surface buoyancy in the Canary Basin are of great importance to detect changes in the AMOC. Detecting changes in the AMOC is of interest because this secondary circulation is related to the meridional heat transport in the ocean, which greatly influences the mid- and high-latitude climate in Northern Europe (*Hall and Bryden*, 1982). In our model work we impose dust-induced density changes at the eastern side of the North Atlantic and seek to study their impact on the AMOC and on the meridional heat transports.

The work presented in this thesis is part of the SOPRAN (Surface Ocean Processes in the Anthropocene, http://sopran.pangaea.de) and international SOLAS (Surface Ocean Lower Atmosphere Study, http://www.solas-int.org/) projects. SOPRAN's sub-projects consist in the following:

- Theme 1: The oceanic response to atmospheric dust.
- Theme 2: Effect of high CO_2 on marine ecosystems and sea-to-air gas fluxes.
- Theme 3: Reduction and emission of radiatively and chemically active gases in the Tropical Oceans.
- Theme 4: Inter-phase transfer at the sea surface.

Our work is developed in the frame of Theme 1. Fig. 1.1 shows a scheme of the biogeochemical response to dust deposition that summarizes the potential impacts of atmospheric dust in the oceans that are being investigated within SOPRAN-Theme 1, and have been discussed above.

Knowing the impact of Saharan dust on the circulation of the eastern subtropical Atlantic and on associated transports of nutrients is therefore specifically important for understanding the climatic relevance of Saharan dust in terms of ocean circulation, air-sea interaction, and biological productivity.

1.1 Aims

The main goals and questions addressed in this thesis can be described as follows:

- Look for evidence of ocean surface dust-induced local cooling in the eastern subtropical North Atlantic, by using AOD and SST information from satellite observations.
- Compare SST retrievals to estimate the ocean surface cooling below a dust cloud (TMI, AMSR-E, AVHRR), in order to choose the appropriate one.
- Estimate how much of the observed changes in SST during strong dust outbreaks are dust-related. To this end, a one-dimensional local mixed layer model is forced with the dust-induced anomalies of the shortwave fluxes. Such anomalies are constructed from radiation and AOD measurements taken on board of the trans-Atlantic Aerosol and Ocean Science Expeditions I (AEROSE-I) cruise, so that a realistic simulation is obtained.
- Use of a three-dimensional eddy-permitting general circulation model, to see whether the differences between the observed and simulated SST can be related to Saharan dust, with special focus on its seasonal variability.
- Force a three-dimensional eddy-permitting numerical model of the ocean by perturbations in solar shortwave flux fields, and compare it to an unperturbed model run.
- Perform a sensitivity study of the MOC reacting to density changes imposed at the eastern subtropical North Atlantic.

1.2 Structure

This thesis is organized in two main chapters where we develop our work, and a final chapter that includes our general conclusions and outlook. Chapters 2 and 3 are structured with introduction, data and methods, results and conclusion sections.

Chapter 2 includes a combined analysis of satellite AOD and SST in the subtropical eastern North Atlantic, and two numerical simulations: (1) a 1D ocean mixed layer model; and (2) a 3D eddy-permitting general ocean circulation model. The simulation (1) is used to estimate the impact of the dust-induced radiative forcing in the local SST during dust outbreaks in the subtropical eastern North Atlantic. Radiative *in-situ* measurements taken during a hydrographic cruise in that region are used to estimate the aerosol radiative forcing with which the 1D simulations are forced. The output from the simulation (2) is used to discrimiate dust-induced SST anomalies from dynamically-induced SST anomalies in time- and spatial-scales that (1) is not able to simulate, by comparing it to the TMI SST observations. In addition, a validation of the chosen SST database is carried out by comparing it with other SST satellite products from AMSR-E and AVHRR. The main results shown in this chapter have been submitted to the Journal of Geophysical Research Oceans (see *Martínez Avellaneda et al.*).

In Chapter 3, we present a sensitivity experiment of the ocean circulation to density changes imposed at the eastern subtropical North Atlantic by the dust-induced anomalies on the shortwave fluxes. By forcing a 3D eddy-permitting numerical model with realistic dust-induced perturbation in solar shortwave flux fields, and comparing these model results with an unperturbed simulation, the dust effects on the circulation and transport of ocean properties, the AMOC and meridional heat transport are investigated.

Chapter 2

Response of the eastern subtropical North Atlantic sea surface temperature to Saharan dust

2.1 Introduction

To identify the eastern Atlantic response to Saharan mineral dust one should combine atmospheric information about dust concentrations with *in situ* observations of the ocean surface temperature. Unfortunately, direct measurements of sea surface temperature (SST) in the eastern North Atlantic in the form of surface drifter measurements or ARGO near surface measurements are too sparse to come to statistically significant conclusions. Until now, measurements of radiative forcing are available only at very few locations, e.g., from island stations and some ships, and observations of biological productivity are only now becoming available in that region through programs like SOLAS (*http://www.uea.ac.uk/env/solas/*). On the other hand, dust clouds over the ocean can be detected from satellite measurements at visible wavelengths. Analyzing the existing satellite database with respect to dust-induced SST anomalies in the eastern North Atlantic seems therefore an obvious and necessary step to be taken.

An example of a Saharan dust outbreak is shown in Fig. 2.1, illustrating an intense dust storm lasting 5 days during early March 2004, as seen by the Moderate Resolution Imaging Spectroradiometer (MODIS) on board of the US NASA Earth Observing System (EOS) Terra satellite. The figure clearly reveals the large spatial extent of a dust layer, which typically can cover an area of about 550 km in the zonal direction and 1750 km meridionally between the African coast and the Canary Islands. Radiometric measurements taken quasi-simultaneously underneath this dust layer during the trans-Atlantic Aerosol and Ocean Science Expeditions (AEROSE) suggest surface radiative forcing anomalies of approximately -100 Wm^{-2} (*Morris et al.*, 2006), equivalent to a 40% reduction of shortwave heating at the surface. Given these strong negative shortwave heating anomalies, a strong thermal response of the upper ocean to Saharan dust should be expected (a radiative forcing anomaly of -100 Wm^{-2} over 15 days would cool a 30 m thick mixed layer by approximately 1° C).

Previously, atmospheric model simulations had suggested that underneath dense atmospheric mineral dust layers the SST may decrease by as much as 1° C (*Miller and Tegen*, 1998). In addition, recent works from *Yoshioka et al.* (2007), *Foltz and McPhaden* (2008) and *Evan et al.* (2008) observe that changes in aerosol cover have a significant impact on the Atlantic SST. Yet, using the existing observational database, a quantitative esti-

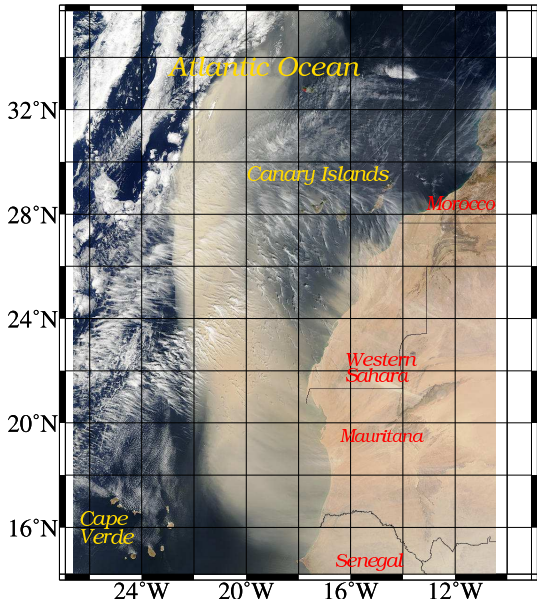

Figure 2.1: MODIS Rapid Response System 2-km resolution true color image off the West Coast of Africa, acquired on March 4, 2004 at 11:55 UTC on board the EOS Terra platform.

mation of how much of the observed ocean surface cooling is dust-induced is still missing.

In this chapter we:

1. Perform a simultaneous analysis of several satellite datasets to investigate whether Saharan mineral dust leads to a cooling of SST of the eastern North Atlantic both during strong storms and at seasonal time scales.

2. Quantify how much of the observed SST changes are dust-induced, using for that purpose:

   – a 1-dimensional local mixed layer model of the upper ocean;
   – a full 3-dimensional eddy-permitting circulation model of the North Atlantic.

   While the eddy-permitting model will give us the full perspective of the dynamical changes in SST that can be expected in our study area, the 1D perspective will be used to provide a measure of a local change in SST that can be expected in response to a local dust-induced perturbation.

The remainder of this chapter is organized as follows: In Section 2.2 we describe the data used in the present work. Aerosol radiative forcing anomalies will be shown in Section 2.3. The relation between the observed SST and Aerosol Optical Depth (AOD) anomalies will be discussed in Section 2.4 and numerical simulations of SST anomalies as they should result from observed dust loads are presented in Section 2.5. A joint interpretation of observed AOD and SST anomalies and model simulations of SST is provided in Section 2.6. The concluding remarks are given in Section 2.7.

2.2 Data and Methodology

Our study is based on a suite of parameters measured from satellites between 2000 and 2006, such as all-weather microwave SST measurements and AOD of the atmosphere. In addition, we used several parameters measured during the AEROSE expedition conducted from aboard the NOAA Ship *Ronald H. Brown* in the eastern subtropical North Atlantic.

2.2.1 MODIS AOD

AOD time series provide a measure of Saharan mineral dust concentrations and can be used to compute the anomaly of solar shortwave irradiance at sea level underneath the dust layer. Daily estimates of AOD are available from the MODIS instrument on board the Terra and Aqua satellites (*Remer et al.*, 2005, 2006). These data are used here to determine the frequency and intensity of Saharan dust outbreaks over the eastern subtropical North Atlantic, as well as to estimate the associated anomalies in solar forcing of the ocean. For our study we used the daily gridded AOD Level-3 MODIS Terra Collection 5 product, available on a 1° x 1° spatial resolution for the period February 2000 to December 2006 (*ftp://ladsweb.nascom.nasa.gov*). During the beginning of the dust outbreak event shown in Fig. 2.1, AOD values as large as 4.5 were observed; during its further evolution the main axis of the plume travelled less than a few degrees westward, while its optical depths decreased to 0.5 on March 9, suggesting primarily dry deposition of dust onto the ocean surface (*Kaufman et al.*, 2005; *Schepanski et al.*, 2009a).

Daily global fields of AOD contain gaps that arise due to various reasons (e.g., sun glint, clouds and/or bright underlying surfaces). Dealing with those gaps in our analysis is difficult and to avoid them we produced weekly composites, which still preserve the major Saharan dust outbreaks. The composites were computed by area-weighted averaging of all observations within each of the 1° x 1° grid cells over a weekly period.

We identified Saharan dust outbreaks, from the daily MODIS AOD product and from the computed weekly AOD anomalies (relative to a climatological seasonal cycle), when values exceeded the AOD time-mean plus twice the local standard deviation ($< AOD > +2\sigma > 0.85$ and > 0.30, for daily and weekly fields, respectively). From Fig. 2.2, several strong dust outbreaks can be detected during the period 2000-2006 between Cape Verde and the Canary Islands (4 in summer, 7 in winter, 1 in spring and 2 in autumn). It is also obvious from the figure that daily data would lead to much higher AOD values during dust storm events and that some of those are eliminated in the weekly averages. However, because our focus here is primarily on the ocean's long-term response to dust, the outbreaks with longer duration are the more relevant events and these will still be captured in the weekly averages.

2.2.2 TMI SST

While AVHRR (Advanced Very High Resolution Radiometer) and MODIS infrared (IR) SST retrievals are significantly impacted by the presence of mineral dust in the atmosphere, SST retrievals from microwave (MW) radiometry are not (*May et al.*, 1992; *Wentz et al.*, 2000; *Chelton and Wentz*, 2005). For our study, microwave SST retrievals from

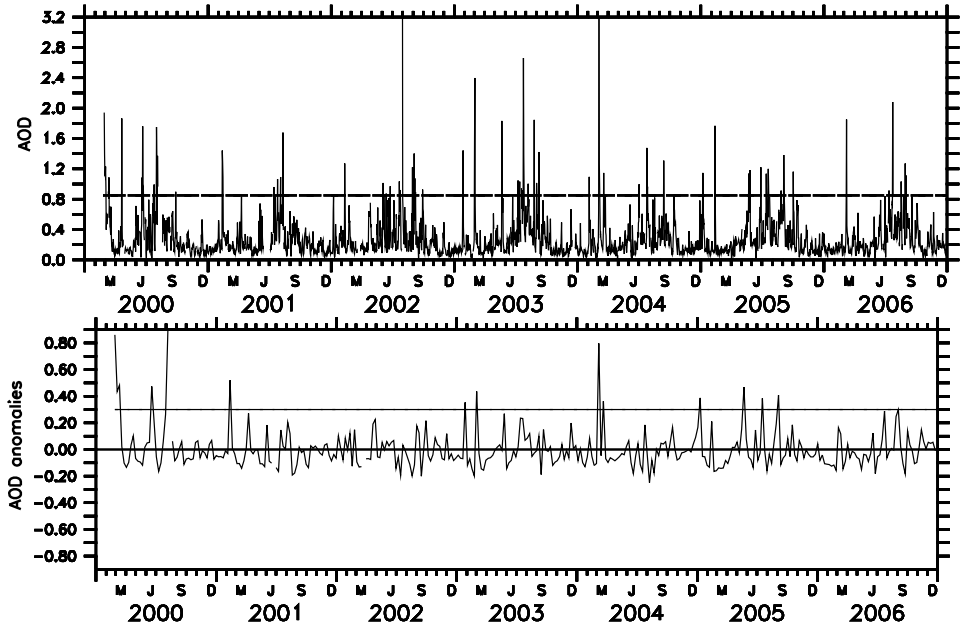

Figure 2.2: Daily retrievals of AOD (top) and their anomalies for weekly composites for 2000-2006 (bottom) from MODIS, averaged over 21° W - 27° W; 19° N - 26.5° N. The horizontal lines represent the $< AOD > +2\sigma$ threshold value, respectively.

the TRMM Microwave Imager (TMI) radiometer on board the Tropical Rainfall Measuring Mission (TRMM) satellite were used as weekly SST fields at a spatial resolution of 0.25° over the period January 1998 to December 2006. The dataset is described in detail by *Wentz* (1998). In addition to the TMI dataset, and partly to test results from TMI, we used version-5 of the SST data available from the Advanced Microwave Scanning Radiometer-EOS (AMSR-E, *Kawanishi et al.*, 2003) on board of the EOS-Aqua satellite.

We are interested in the question whether Saharan dust (outbreaks and/or seasonal cycle) and its associated cooling can lead to cold SST anomalies in the eastern North Atlantic and to what extent they can be detected in existing satellite SST datasets. To answer both questions one needs a reliable satellite SST database that is not affected in its retrieval procedure by the dust. This holds for microwave SST observations and what follows is therefore mostly based on the TMI SST dataset. *Stammer et al.* (2003) tested the quality of TMI data by comparing them against *in situ* measurements on a global scale and found a standard deviation difference of about 0.45° C.

To obtain further confidence of the quality of the TMI SST fields, we show in Fig. 2.3a a comparison between SST anomalies as inferred from the TMI (red) and AMSR-E (black) microwave radiometers for the period 2002-2005 averaged over the region (18° W - 25° W; 15° N - 22° N). In both cases the SST anomalies were calculated with respect to a climatological seasonal cycle computed from 9 years (1998-2006) of TMI data. The MW SST anomalies are about the same albeit somewhat smaller in amplitude for AMSR-E. Arrows in the figure mark seasonally high dust loads (in summer, purple arrows) and the strongest dust events in winter (black arrows), as identified from the AOD time series.

A first visual comparison reveals that both MW SST time series decrease simultaneously to most of those events, as it would result from cooling.

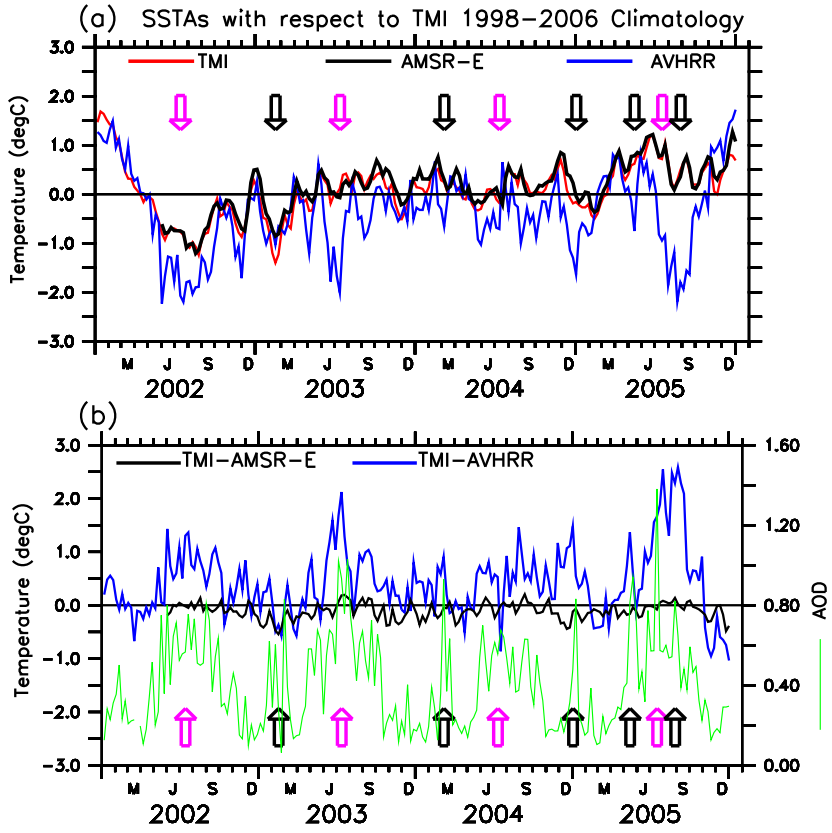

Figure 2.3: (a) Time series of SST anomalies obtained from the TMI (red), AMSR-E (black), and AVHRR (blue) sensors, for the period 2002-2005. In all cases, the SST anomalies were calculated relative to a climatological seasonal cycle computed from TMI data over the 9-year period 1998-2006, and averaged subsequently over 25° W - 18° W; 15° N - 22° N. (b) Differences between TMI and AMSR-E data (black) and between TMI and AVHRR data (blue). Also shown (in green) is the time series of weekly averaged MODIS AOD data representing the same area and including the seasonal cycle. Red arrows in both panels indicate seasonal high dust loads (centered in July 15, in purple) and black arrows indicate strong dust events in winter (larger than 0.8 for weekly averages, in black).

Also shown in the figure is a time series of SST anomalies from the AVHRR Pathfinder data (*Kilpatrick et al.*, 2001), after subtracting the same TMI climatological seasonal cycle for comparison purposes. Differences between the SST from TMI and AMSRE and from TMI and AVHRR (shown in Fig. 2.3b) indicate that the two MW SST products stay close together (within a 0.5° C range; rms(TMI-AMSRE)=0.17° C). In contrast, the AVHRR SST estimates deviate substantially from both MW observations (rms(TMI-AVHRR)=0.78° C), sometimes by as much as 2° C or more during strong dust events, with a clear seasonality also present in the difference. This suggests that AVHRR data

is biased cold by as much as 1° C or more in this region during summer months.

It is known that both clouds and aerosol can lead to biases between IR and MW SST (*Chelton and Wentz*, 2005). In our study region, clouds and Saharan dust have both seasonal cycles connected to the seasonal movement of the ITCZ and, in principle, the differences shown in Fig. 2.3 could therefore result from either effect. However, *Corlett et al.* (2006) previously showed differences between SSTs from the dual view Advanced Along-Track Scanning Radiometer (AATSR) and SSTs from MODIS and AVHRR of about 1° C in our study area and argued that they result from dust impact on MODIS and AVHRR retrievals. This conclusion was backed up by *Vázquez-Cuervo et al.* (2004) who demonstrated that AATSR is less sensitive to aerosols due to the dual view. They also report negative correlations between aerosols and AATSR SST minus AVHRR SST (as well as with in-situ comparisons) in our studied region.

Those earlier results suggested to compare the SST differences shown in Fig. 2.3 with the weekly averaged AOD (Fig. 2.3b). A visual inspection shows a clear relationship between periods of enhanced AOD and associated dust concentrations and periods of large TMI minus AVHRR SST differences, suggesting that the impact of dust clouds on the AVHRR retrieval is the primary agent for causing the AVHRR SST to be biased cold. This applies for dust content on a seasonal cycle as well as for strong dust outbreaks on time scales of up to a few days. These effects are consistent with the earlier findings from *Vázquez-Cuervo et al.* (2004) and are therefore the consequence of the AVHRR atmospheric correction algorithm failing to adequately compensate for the dust and the dry SAL. We conclude therefore that AVHRR datasets are not appropriate for the study intended here. At the same time it is obvious that microwave SST data have an important role to play in such studies of climate change, especially if there is an expected changing dust load of the atmosphere in response to a changing climate (see *Mahowald and Luo*, 2003).

2.3 Aerosol Radiative Forcing during AEROSE-I

To understand the impact of Saharan mineral dust on SST of the eastern Atlantic, an important quantity to know is the shortwave (SW) radiative forcing anomaly at sea level associated with a specific dust load of the atmosphere, referred to below as aerosol radiative forcing anomaly flux (ARF in Wm^{-2}). ARF associated with dust in the SAL is usually computed from AOD fields according to:

$$ARF = f_e \cdot AOD \tag{2.1}$$

where f_e is the aerosol surface forcing efficiency coefficient (in units of $Wm^{-2}AOD^{-1}$, see *Ramanathan et al.*, 2001) and AOD is the aerosol optical depth from MODIS discussed above. A few estimates of f_e are available (*Li et al.*, 2004; *Yoon et al.*, 2005; *Zhu et al.*, 2007).

Fig. 2.4, provides an example of an ARF field that resulted from the March 2004 dust event shown in Fig. 2.1.

In order to estimate the ARF, forcing efficiencies for that month, year and region are needed. *Yoon et al.* (2005) provide monthly values of f_e obtained from observations during the period October 1994 - December 2003. Even though the year 2004 is not

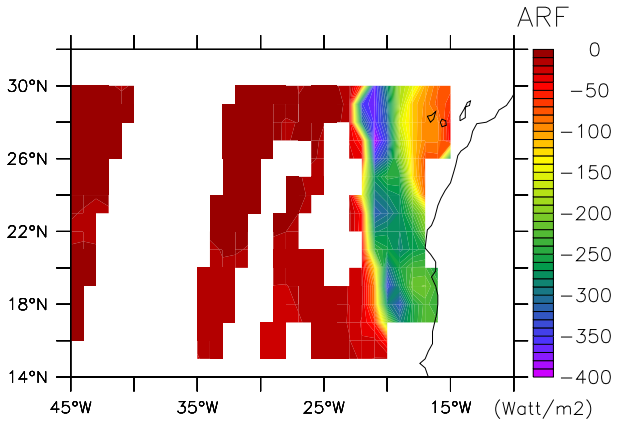

Figure 2.4: Aerosol-induced Shortwave Radiation Forcing anomaly at sea level, inferred from MODIS-AOD field for March 4, 2004 and results from *Li et al.* (2004) and *Yoon et al.* (2005).

included, their results are based on a 9-year climatology, so it seems quite reasonable to use their estimation for March 2004. But, the region for which these results are valid (called Cape Verde in their manuscript) includes a large portion of the African continent (see brown box on Fig. 2.5, left panel) which will lead to misleading results when applying for the oceanic region that is being investigated in this thesis.

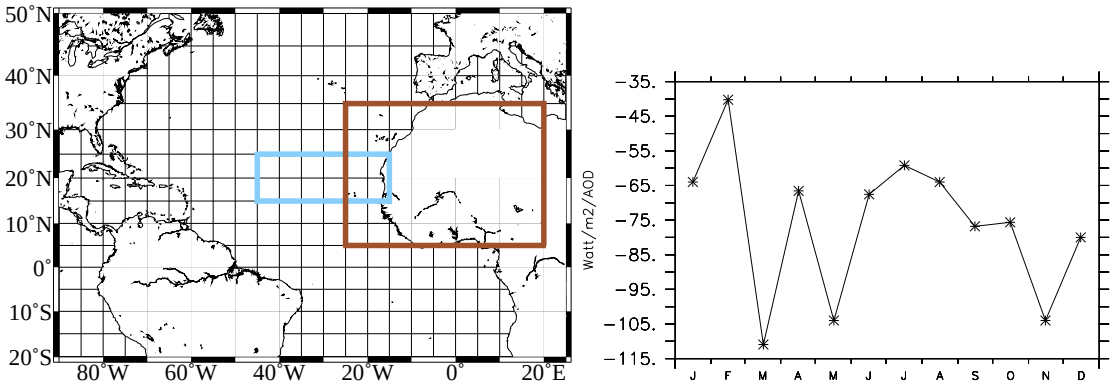

Figure 2.5: (right) Areas for which *Li et al.* (2004) and *Yoon et al.* (2005) calculated their f_e are shown in blue and brown respectively. (right) Time series of f_e extrapolated into the present studied region.

The surface f_e obtained by *Li et al.* (2004), was calculated for a region over the Atlantic Ocean near the African coast (blue box shown on the Fig. 2.5 map), but only values for the high-dust season (June/July/August) and the low-dust season (November/December/January) were provided.

These two results are then combined to obtain monthly surface f_e values on the oceanic region that is of interest of this work. The results are shown on the right panel of Fig. 2.5.

Using the corresponding forcing efficiency value for March (f_e = 80 Wm^{-2}/AOD),

associated ARF amplitudes of up to -300 Wm^{-2} can be inferred from the MODIS AOD data in some regions during that day (Fig. 2.4). However, a detailed knowledge of f_e on this region is missing and it is part of this study to revisit the question of what is the actual amplitude of f_e and what its wavelength sensitivity is. With this purpose, data available from the AEROSE expedition will be used.

The AEROSE project consisted of a series of intensive field experiments conducted aboard the U.S. National Oceanic and Atmospheric Administration (NOAA) research vessel, the *Ronald H. Brown* (*Nalli et al.*, 2005, 2006; *Morris et al.*, 2006; *Hawkins et al.*, 2007). The present analysis is based on data obtained during the first cruise (AEROSE-I) which took place during spring of 2004, departing from Bridgetown, Barbados, on February 29 and returning to San Juan, Puerto Rico on March 26, 2004, after crossing the Atlantic twice in zonal direction (see left panel Fig. 2.6). During the cruise, the ship encountered two significant Saharan dust events off the African coast in the period 9-18 March underneath which radiometric and ocean observations were obtained (Fig. 2.6, right panel). The column-integrated optical depth observations were obtained by two up-ward looking, handheld commercial Microtops sunphotometers in five different bands and AOD estimates were derived from these measurements according to *Knobelspiesse et al.* (2004). The concept of Microtops sunphotometer is rather simple. UTC time and GPS location determine how much solar energy can be expected. The measured sun-light provides information, by how much the aerosol has attenuated the direct sun-light. This sun-light sampling is done at specific solar sub-spectral regions to avoid interference by trace-gas absorption. The challenge in operating the instrument is to find cloud (and specially cirrus) free views of the sun and to point the instrument during sampling directly into the sun, with the help of a visual device on top of the instrument.

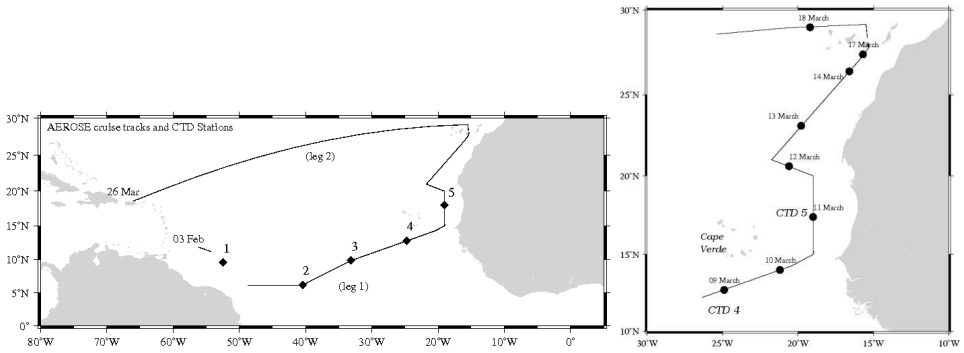

Figure 2.6: Ship track and positions of CTD stations conducted during the 2004 AEROSE-I cruise from 9 to 18 March, for the complete cruise (left) and for our studied region (right). Black dots indicate the location where AOD measurements were performed on board the ship several times per day.

In Fig. 2.7 we show respective AOD measurements taken at sea level at wavelengths of 380 nm and 870 nm (Fig. 2.7a, see Fig. 2.6 for locations). Also shown in the figure are SW radiation fluxes measured quasi-continuously at sea leavel (Q_{SL}, Fig. 2.7b) from aboard the ship. Apparent from both panels is the impact of clouds on the measurements, especially after March 11. In the solar SW radiation measurements, clouds usually

lead to reduced radiation fluxes; however, in some instances, surface SW fluxes are also enhanced due to forward scattering from the broken clouds when the cloud fraction is small and the sun is in a cloud-free sky (e.g., *Pfister et al.*, 2003). The baselines of the AOD measurements are indicative of dust concentration changes under cloud-free conditions (Fig. 2.7c). Cloud impacts lead to significant variability in the AOD observations. Because the ARF is defined as the difference between the incident radiative flux calculated under clear-sky conditions with and without aerosols (*Won et al.*, 2004; *Yoon et al.*, 2005), we have to eliminate the effect of cloud contamination on the radiation measurements, before f_e and ARF can be estimated from the AEROSE-I data.

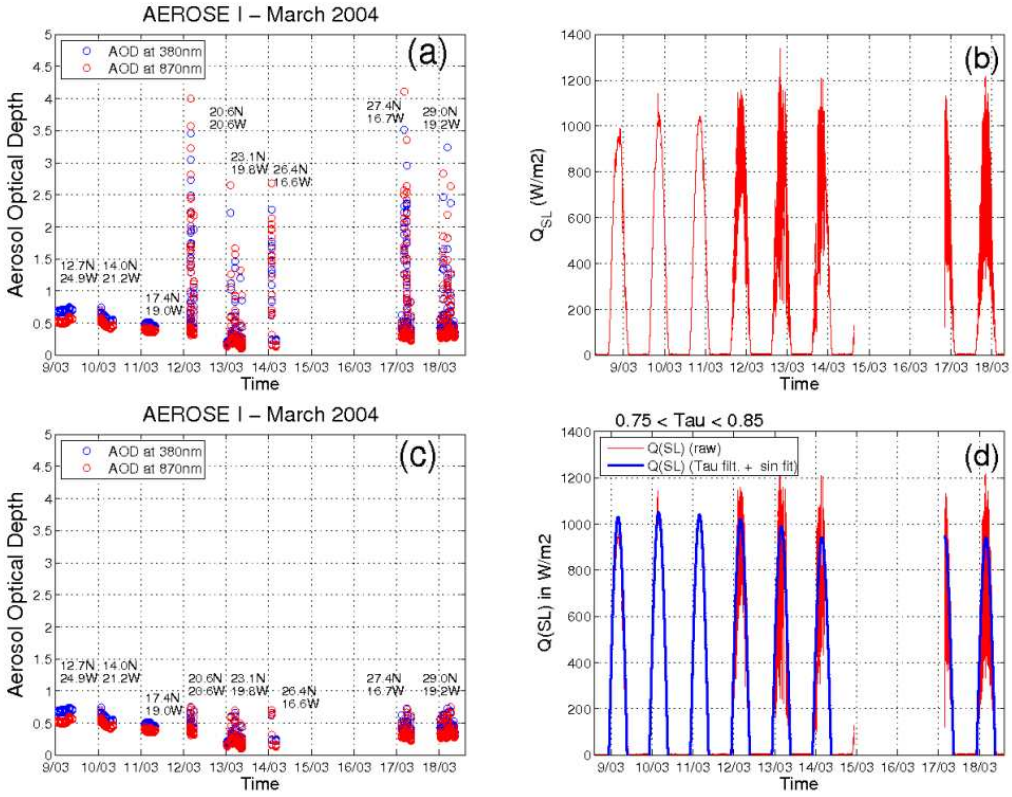

Figure 2.7: (a) AOD measurements at 380 *nm* (red) and 870 *nm* (blue) and (b) short-wave radiation fluxes, Q_{SL}, measured at sea level during the AEROSE-I cruise from 9 to 18 March, 2004 (see Fig. 2.6 for locations). In the bottom row the same two fields are shown after eliminating the effects of clouds. Panel (c) shows cloud-free AOD measurements at 380 *nm* (red) and 870 *nm* (blue) at sea level, and panel (d) the time series of Q_{SL} for clear sky conditions (in blue) superimposed to the cloud-contaminated values (in red; see also text for details).

To identify cloud-free conditions, we use the amplitudes of the normalized short wave atmospheric transmissivity, τ, which is the fraction of incident solar energy incident at the top of atmosphere (TOA, Q_{TOA}) that would reach the surface with the sun overhead, and defined as Eq. 2.2 (Fig. 2.8a). Low values of τ result from the presence of clouds,

and anomalously high values occur when the sensor is in the direct beam of the sunlight with additional energy scattered by the clouds.

$$Q_{SL} = Q_{TOA} \times \tau^{1/cos(solar\ zenith\ angle)} \tag{2.2}$$

To eliminate cloud-contaminated data, the first step was to discard all measurements for which τ is higher than 0.85 and lower than 0.75 (Fig. 2.8d and 2.8e). The high threshold was chosen to be somewhat lower than the clear-sky normalized atmospheric transmissivity measured in the clear polar atmospheres (*Minnett*, 1999; *Hanafin and Minnett*, 2001; *Key and Minnett*, 2006), and cases with values below the lower threshold were clearly influenced by the presence of clouds.

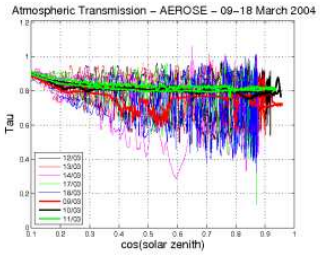

(a) Atmospheric transmissivity τ plotted against the cosine of zenith angle.

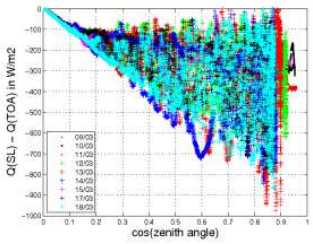

(b) Difference between Q_{SL} and Q_{TOA} plotted against the cosine of zenith angle.

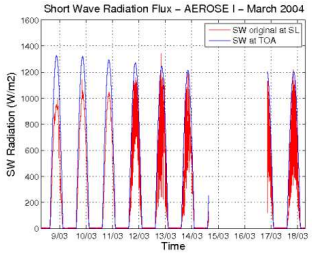

(c) Time series of measured Q_{SL} (red) and estimated Q_{TOA} (blue)

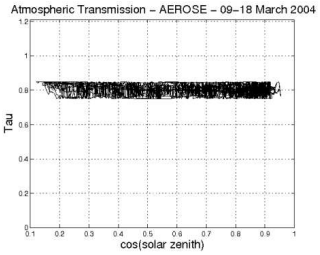

(d) Same as (a) but only values corresponding to $0.75 < \tau < 0.85$ are retained.

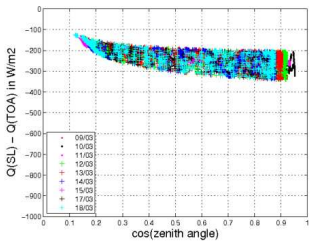

(e) Same as (b) but only values corresponding to $0.75 < \tau < 0.85$ are retained.

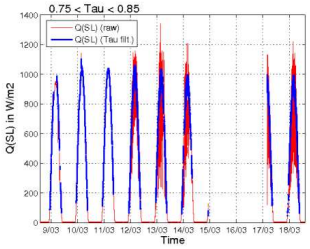

(f) Time series of Q_{SL} for clear sky conditions (in blue), superimposed to measured Q_{SL} (in red)

Figure 2.8: Measured and estimated parameters from AEROSE-I used to calculate the forcing efficiency f_e.

A 'cleaner' Q_{SL} signal is already visible from the Fig. 2.8f (plotted in blue). As a second step of the cloud detection and elimination process, we fitted a sinusoidal function to the resulting SW radiation (Fig. 2.7d) Because March 11 was essentially cloud-free, we used the radiation profile from that day to simulate the cloud-free daily cycle in solar radiation during the following days. But because AOD is varying with time, the cloud-free noon radiation also varies from day to day. To account for this we used a scaled version of the daily radiation cycle from March 11 and superimposed on it the measured shortwave radiation data of all other days.

An estimate of the efficiency factor, f_e, was obtained from the differences between the Q_{SL} and the shortwave fluxes at TOA (Q_{TOA}). These are plotted in Fig. 2.9 as a function

of AOD at 380 nm and 870 nm, considering all cloud-free values from 9 to 18 March 2004 and only the AEROSE-I AOD measurements between 0.1 and 0.75 (see Fig. 2.7c). Values of Q_{TOA} were calculated for the position of the sun at the location of the ship at the times of the measurements using the equations given in the Astronomical Almanac (*Astronomical Applications Department*, 1990) and for the refraction of the atmosphere as given by *Zimmerman* (1981). Using the results from the 380 nm channel, a linear regression between Q_{SL}-Q_{TOA} and AOD leads to values of f_e of:

$$f_e = (Q_{SL} - Q_{TOA})/AOD = -73.5 \pm 7.1 \;\; Wm^{-2}AOD^{-1} \tag{2.3}$$

with a correlation coefficient of -0.41. The slope is smaller ($-57.9 \pm 8.9 \;\; Wm^{-2}AOD^{-1}$) when using the 870 nm channel (correlation of -0.27) and using an average of both channels would result in a value of $f_e = -69.1 \pm 8.0 \;\; Wm^{-2}/AOD$. We note, for a later interpretation, that the AOD measurements were taken between 13h and 19h local time, and that the f_e estimate therefore corresponds to the afternoon situation, rather than to a daily mean field. Compared to previous estimates available from *Li et al.* (2004), *Yoon et al.* (2005) and *Zhu et al.* (2007) ($f_e \approx 80 Wm^{-2}AOD^{-1}$, during winter), our results are somewhat lower, although still close. Considering the offset for AOD = 0 as a further consistency check, the estimates lead to values of -212.2 ± 3.6 Wm^{-2} and -225.3 ± 3.6 Wm^{-2}, for 380 and 870 nm, respectively. In comparison, the theoretical value is -180 Wm^{-2}, which exists for the global ocean. Our estimates are larger, and this can partially be related to regional variations.

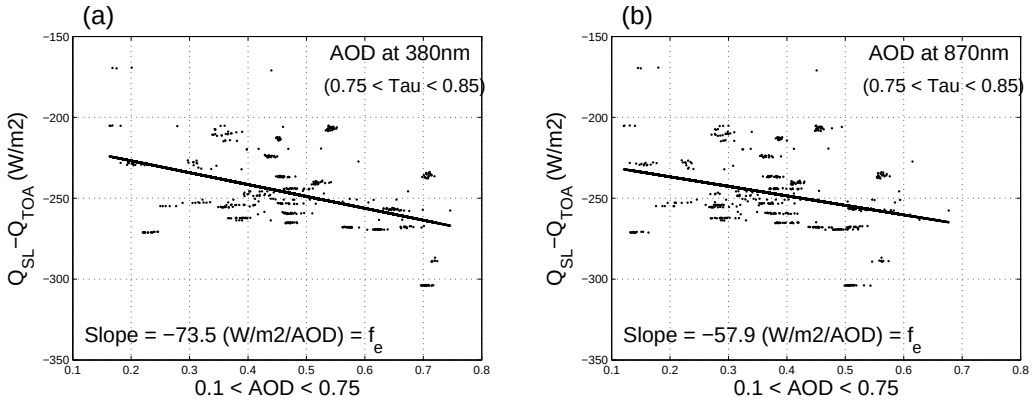

Figure 2.9: Difference between Q_{SL} and Q_{TOA} for 'cloud-free' conditions plotted as a function of AOD 380 nm (a) and 870 nm (b). The slope of a least-squares fitted line represents the value of the f_e in units of $Wm^{-2}AOD^{-1}$ (Eq. 2.3).

2.4 Observed SST and AOD anomalies

Examples of weekly-averaged AOD time series during strong dust events and contemporaneous weekly-averaged TMI SST anomalies (relative to a climatological seasonal cycle), are provided in Fig. 2.10 for the years 2002 to 2005, both averaged over the region 27° W - 21° W, 19° N -26.5° N. The figure reveals several intense dust periods lasting several

days. It appears that during or after some of those dust events, the SST shows downward tendencies (either as cooling or as reduced warming) as would be consistent with dust-related cooling.

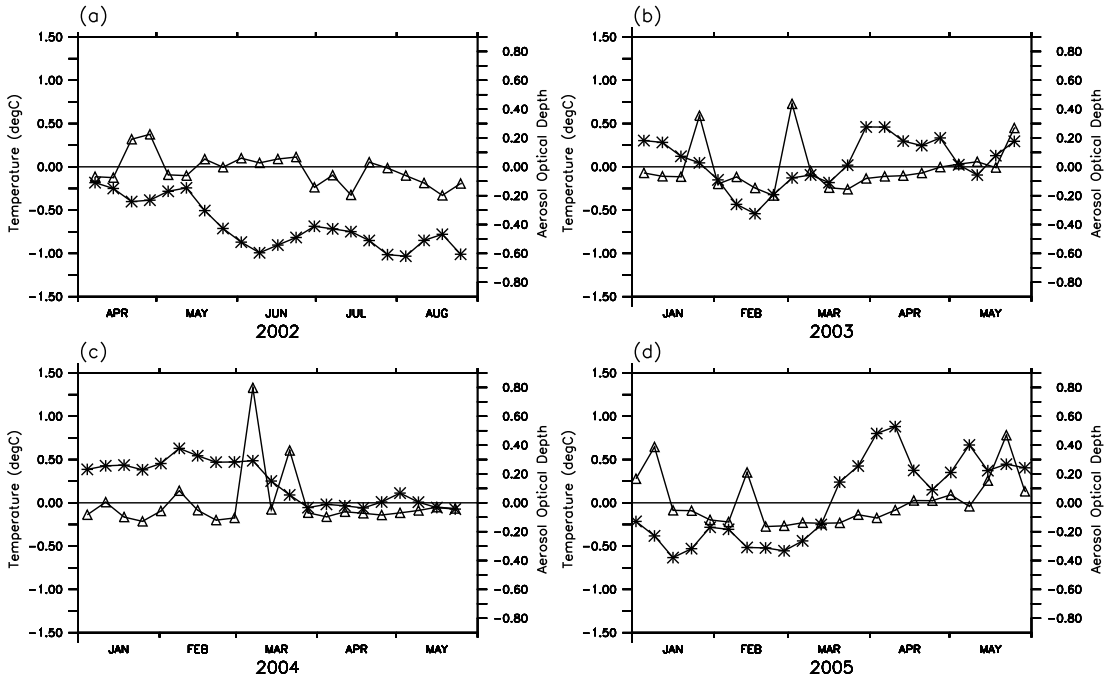

Figure 2.10: Time series of weekly anomalies of MODIS AOD (triangles) and of TMI SST (stars), averaged over 27° W - 21° W; 19° N - 26.5° N, for the periods: April - August 2002 (a) and January - May for years 2003 (b), 2004 (c) and 2005 (d).

Fig. 2.10a reveals an intense dust period during late April and beginning of May 2002. A second (although weaker) dust event occurs in the July/August time frame. After the first dust period, SST declines over a one and a half months period by as much as 1° C. The SST subsequently recovers until the end of June, however, consistent with the second dust period, the SST declines again during late July. Similarly, a drop in SST up to about 1.4° C is observed in mid-February 2003 (Fig. 2.10b), after one strong dust event occurs in the preceding weeks. SST starts increasing during a subsequent low dust period but shows a new drop after a further strong event at the beginning of March. During 2004 (Fig. 2.10c) two high AOD events occurred in March. Even though this seems to be a period with background positive SST anomalies, the strong dust event in March 4 clearly coincides with a reduction in SST. Finally in 2005 (Fig. 2.10d) the situation is somewhat different in that two dust outbreaks can be observed only at the beginning and at the end of the January-May period (both accompanied by a downward tendency of the SST), while in the rest of the period SST shows strong intermittent SST variability seemingly unrelated to dust outbreaks. So, from a visual inspection of Fig. 2.10 one can hypothesize that during several instances a plausible relation exists between enhanced atmospheric dust loads, associated attenuation of solar irradiance and resulting cooling (or reduced warming) of SST.

Assuming for the moment that any observed change in SST is related to a dust-induced variation in surface heat flux forcing, according to a simple bulk mixed layer relation, given as

$$\frac{d(SST)}{dt} = \frac{ARF(t)}{\rho \cdot c_p \cdot h(t)}, \tag{2.4}$$

we should be able to find a relation between changes in AOD and tendencies in SST. In Eq. 2.4, ARF(t) could be taken from Eq. 2.1, ρ is a typical density of the upper ocean, c_p is the specific heat of seawater and h would be a typical, but known, mixed layer depth (MLD). If, for simplicity, we take the MLD and the f_e to be constant with time, then we should expect a linear relationship between the accumulated AOD and the SST. This is consistent with the scatter plot between the weekly anomalies of SST observations and the accumulated AOD for the entire period 2000-2006 (Fig. 2.11), which shows positive (negative) values of accumulated AOD anomalies to be associated with negative (positive) anomalies of SST. The coefficient of correlation (r) is significant at 95% of confidence level and was found to be maximum ($r = 0.55$) when the anomalies of AOD lead those of SST by 1 week. The slope of the linear regression (-0.27° C AOD^{-1}) leads to an estimate of the mean value for the mixed layer depth of about 22m. This is somehow shallower than those values of *de Boyer Montégut et al.* (2004) and our findings in the next section. Nevertheless, the value is plausible and supports the validity of a relation between SST trends and AOD.

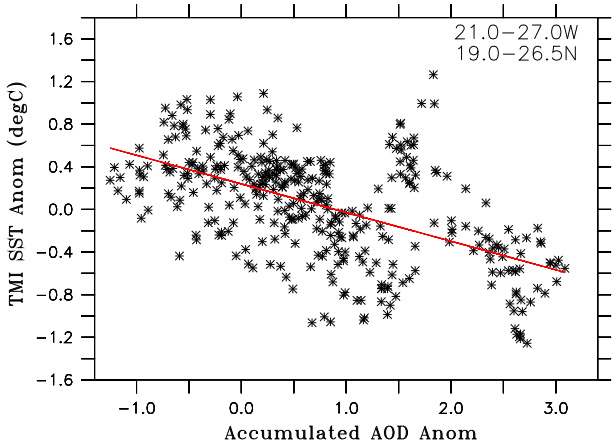

Figure 2.11: Scatter plot between accumulated weekly anomalies of MODIS AOD and weekly anomalies of TMI SST, for the region 27° W - 21° W; 19° N - 26.5° N and for the period 2000-2006. The AOD is leading the SST for 1 week. The red line represents the fitted least-squares linear regression. The resulting coefficient of correlation and slope are 0.55 and -0.27, respectively.

The results shown in Fig. 2.11 suggest that about 30% (i.e.: r^2) of the SST variance could be explained by those of the accumulated AOD in our study region. However, the remaining 70% of SST variance occur on all time scales because many processes lead to SST changes, most of which are not related to dust events at all. Accordingly, dust-induced SST anomalies will always be superimposed, or even masked, by SST changes

associated with ocean dynamics or remote forcing. Separating local dust effects from dynamical SST variations (e.g., resulting from mechanical-wind stirring, upwelling and/or eddies and planetary waves) remains a challenge in any study based on (satellite) data alone, implying that more information from ocean dynamics is needed in any quantitative investigation.

We conclude that a quantitative and unambiguous connection between Saharan dust outbreaks and surface cooling as hypothesized by *Miller and Tegen* (1999) cannot be made convincingly from the data at hand, but that additional information is necessary, e.g., as available from ocean dynamics embedded in circulation models. Nevertheless, a significant relation between SST changes and dust appears to be present.

2.5 Simulated SST anomalies in the ocean mixed layer

To simulate the response of SST to dust-induced cooling, an approach based on a simple bulk mixed layer model would be an oversimplification, since the MLD, taken to be constant and known in Eq. 2.4, in reality is highly variable in space and time due to its dependence on many parameters, including surface wind stress. To further aid the investigation of dust effects on SST we use here a local mixed layer model to determine the amplitudes of SST anomalies that can be expected during individual dust events. In the next section, the use of a three-dimensional circulation model will help to identify dynamical SST features.

The state-of-art 1-D mixed layer model of the upper ocean is based on the coupled KPP mixed layer model (*Large et al.*, 1994) (the model will be referred to as KPP-1D henceforth). The philosophy of this conceptual study is to neglect advective processes and thereby to investigate the magnitude of SST anomalies that can be forced locally by strong dust events.

Two distinct vertical mixing schemes in the oean are considered: mixing in the ocean's surface boundary layer (OBL) and in the ocean's interior.

Mixing in the OBL near the surface happens under various surface forcing conditions (buoyancy and momentum). It consists of the 1-D upper ocean mixing parameterization in which a bulk Richardson number is used to determine the depth of the OBL (h), and a non-local KPP is applied subsequently as the vertical mixing scheme in the OBL.

The expression for the vertical turbulent fluxes of momentum $\overline{wx}$ and tracer properties (X) throughout the OBL is given by:

$$\overline{wx} = -K_x \left(\frac{\partial X}{\partial z} - \gamma_x \right), \quad X = \{U, \theta, S, T\} \tag{2.5}$$

where d is the distance from the boundary, and $d = -z$ in the OBL. It consists on the sum of a down-gradient flux ($\partial X/\partial z$) and a non-local transport term (γ_x) that enhances the gradient-flux mixing coefficient (K_x) further where the water column is unstable. In other words, it has a diffusivity component and a non-local transport component. The model works as follows: the external forcing is prescribed, h is determined and the difussivity and non-local transport profiles are computed. The profile of the diffusivity is defined as follows:

$$K_x(\sigma) = hw_x(\sigma)G(\sigma) \tag{2.6}$$

where w_x is a depth dependent turbulent velocity scale, $G(\sigma)$ is non-dimensional vertical shape function [1], and $\sigma = d/h$ is a dimensionless vertical coordinate. The non-local transport term (γ_x) is non-zero for scalars in convective forcing conditions (i.e., salt and temperature, see *Large et al.* (1994)).

In the interior, mixing is due to internal wave activity, shear instability (dependent on a local gradient Richardson number [2]), and double diffusion (molecular). Eq. 2.6 is matched (itself and the first derivate) to the interior, and $\gamma_x = 0$.

In the runs performed, the vertical resolution is 1 m over the top 100 m. To run the KPP-1D model, initial temperature and salinity profiles were used as provided by CTD profiles collected during AEROSE-I at the location 19.0° W, 18.0° N (Station 5 in Fig. 2.6).

To simulate the effect of Saharan dust cooling of the sea surface, two simulations were performed: a control run and a perturbed run. The control run was driven by net forcing fields provided every 6 hours by the National Center for Environmental Prediction/National Center for Atmospheric Research (NCEP/NCAR) Reanalysis-1 (*Kalnay et al.*, 1996). This version of the KPP-1D model can be forced either with the state of the atmosphere, or directly with the fluxes. In this case, we prescribed NCEP reanalysis surface fluxes which included wind stress, sensible heat flux, evaporation, radiative fluxes and precipitation. The evaporation was estimated with the latent heat fluxes from NCEP/NCAR Reanalysis-1 and the enthalpy of vaporization. Fields were linearly interpolated every 30 min. from the available 6-hourly values. Because the NCEP forcing does not include any impact of Saharan dust on the surface SW forcing (*Lacis and Hansen*, 1974), this run is not affected by any dust-related cooling. The perturbed run incorporated the dust effect inferred from the MODIS-based AOD time series as shown below.

The effect of dust loads was incorporated into the model through a reduction of the NCEP SW forcing by the ARF forcing. To this end, the following steps were performed:

1. The MODIS daily AOD time series was evaluated at the station location and converted into daily ARF according to Eq. 2.1, with f_e values provided by Eq. 2.3.

2. In a second step a modified SW forcing was constructed that included the effect of Saharan dust according to:

$$\tilde{SW}(t) = SW(t)(1 - ARF/SW_{max}), \tag{2.7}$$

   where ARF was provided every day, $SW(t)$ was available every 6h and SW_{max} is the maximum noon radiation value. In this way, the night values are not altered and a maximum reduction of the SW is obtained at noon of every day.

3. No other dust effect on the surface radiative forcing was accounted for, such as enhanced incident longwave radiation. This step is justified by *Vogelmann et al.*

[1] See Fig. 2 from *Large et al.* (1994) for examples of $G(\sigma)$ and $w_x(\sigma)$ profiles.
[2] The gradient Richardson number is defined as: $Ri(z) = N^2(z)/(dU/dz)^2$. See *Kundu* (1990).

(2003), who showed that the respective forcing would only be of the order of $\pm$10W m^{-2} which can be confidently neglected here.

The decrease in surface temperature resulting from the difference between the perturbed and unperturbed runs is therefore due only to the SW flux anomalies derived from the presence of dust in the atmosphere. Because what matters to our analysis here is the resulting ocean temperature at the uppermost level of the model, in the following we will only show the top level temperature anomaly, assuming it is equivalent to the SST anomaly. Results are shown in Fig. 2.12, for strong dust outbreak periods during winter 2003 and 2004. Shown in the top row of the figure are SST anomalies as they result for the periods February 1 through March 31, 2003 (left) and February 1 through March 31, 2004 (right) with a temporal resolution of 30 min. Also shown are MODIS daily AOD observations at the same position. Because in our study dust impacts only the SW solar irradiance, SST anomalies show a clear daily cycle with maximum negative amplitudes occurring during mid-day and close to zero changes during night time. Moreover, an overall decrease due to the general presence of dust during the entire considered period is observed.

Focusing first on the left panel, two dust events are apparent from the AOD time series during early 2003, with peak AOD values of about 1.9 occurring during February 11. A second and somewhat longer event was observed since the beginning of March ($0.7 <$ AOD < 1.7). In both cases, SST decreases are simulated during and shortly after peak dust concentrations. This is specially obvious during the second event lasting for about 5 days in early March, when SST decreases by about 0.3° C. Even though a quantitative connection was not possible from our analysis of Fig. 2.10, the decrease observed at the beginning of March 2003 (Fig. 2.10b) agrees with the magnitude simulated here. We note that only weekly averages were shown in Fig. 2.10, which inevitably lead to smaller amplitudes in the SST anomaly and temporal shifts of the maximum response. We also note that the first dust event, ocurring on February 11, has a smaller signature in SST, yet the forcing amplitude appears larger compared to the March event.

To understand why this is so we show, in the middle row of Fig. 2.12, anomalies of the SW forcing together with the absolute value of wind forcing. Moreover, shown in the bottom row of the figure are time series of the SST and MLD for the perturbed and unperturbed runs. The MLD is fairly deep during the beginning of February (around 40 m). A decline of MLD occurs during early March, when the wind stress suddenly drops to a minimum, leading to a MLD of less than 15 m. The same holds during 2004 (right column): a shallow MLD is present only at the end of March (neglecting the two intermittent shoaling events), while the major dust event occurred 20 days before. Accordingly, the SST response simulated during 2004 is likewise moderate and only of the order of 0.1° C.

The experiments suggest that, if applied only over short periods, dust-induced cooling of the surface strongly depends on the structure of the upper ocean and especially the thickness of the surface mixed layer. To have a measurable impact on SST, a shallow mixed layer is required simultaneously to enhanced dust loads. Wind stirring tends to deepen the mixed layer through mixing and would thereby eliminate the signal. Amplitudes of SST anomalies, simulated with the KPP-1D model, are comparable to those observed in Fig. 2.10 shortly after strong dust events. However, while observed changes

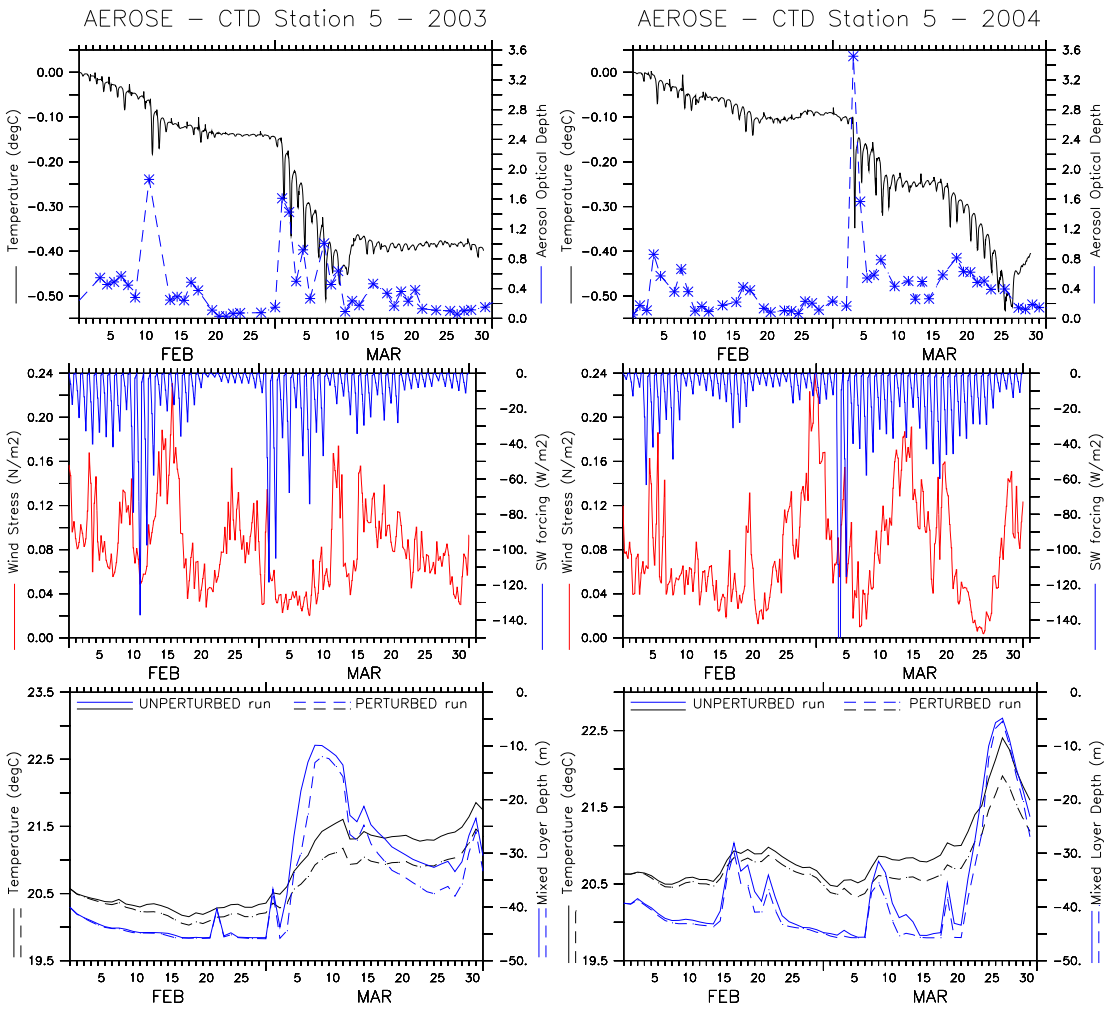

Figure 2.12: Results from the KPP-1D simulations for the years 2003 (left column) and 2004 (right column) at the position of CTD Station 5 (19° W, 18° N, see Fig. 2.6). Top row: Daily MODIS AOD (blue) plotted together with the 30 min. SST difference between perturbed and unperturbed runs (black). Middle row: ARF (blue) and wind stress magnitude (red). The wind forcing was the same for perturbed and unperturbed runs, and the heat flux shown is the difference between the forcing for the perturbed runs and the forcing for the unperturbed runs, i.e., the anomaly associated to ARF. Bottom row: Daily SST (black) and mixed layer depth (blue) for the perturbed and unperturbed runs. Solid and dashed lines in the bottom row panels represent unperturbed and dust-perturbed runs, respectively.

are plausible, both in terms of amplitude and phase, a definitive proof of them being generated by dust cannot be given from the 1D simulation; instead a full ocean circulation model is needed (next section). Nevertheless, the results provide the important information that a strong response of SST due to Saharan dust can be expected only during periods of low wind stirring (and associated low mixed layer depth) and that

therefore more emphasis needs to be put on the impact of dust on SST on the seasonal time scale, discussed in the next section.

2.6 Isolating dust-induced SST anomalies

To further discriminate dust-induced SST anomalies from dynamically-induced SST anomalies, the output from an ocean circulation model simulation of the North Atlantic is analyzed. The model description and the setup of the simulation are presented first.

2.6.1 Model description

The model chosen to carried out this work, is the Massachusetts Institute of Technology General Circulation Model (MITgcm). The model, code, documentation and papers charting its development can be found at http://mitgcm.org/. The MITgcm is designed to study both large-scale/global and small-scale processes of the atmosphere and ocean. It is widely portable and highly efficient on a wide range of computational platforms (*Marshall et al.*, 1997b; *Adcroft et al.*, 2004b). The MITgcm achieves this capability with a number of novel aspects:

(1) Its non-hydrostatic capability (*Marshall et al.*, 1997a)

(2) The use of a finite volume numerical method allowing an intuitive discretization and support for the treatment of irregular geometries (*Adcroft et al.*, 1997)

(3) The layered approach to software and computer technology (*Hill et al.*, 1999)

(4) The use of one hydrodynamical kernel to simulate both atmosphere and ocean (*Marshall et al.*, 2004)

(5) The maintenance of MITgcm adjoint model (*Marotzke et al.*, 1999; *Heimbach et al.*, 2002)

The equations of the MITgcm are:

$$\rho_0 \frac{d\vec{v}}{dt} + 2\vec{\Omega} \times \rho_0 \vec{v} + g\rho\hat{k} + \vec{\nabla} p = \mathbf{F} \quad \text{MOMENTUM} \tag{2.8}$$

$$\rho_0 \vec{\nabla}.\vec{v} = 0 \quad \text{CONTINUITY} \tag{2.9}$$

$$\frac{\partial \eta}{\partial t} + \vec{\nabla}.(H + \vec{\eta})\vec{v}_h = \mathbf{P} - \mathbf{E} \quad \text{FREE-SURFACE} \tag{2.10}$$

$$\frac{D\theta}{Dt} = \mathbf{Q}_\theta \quad \text{HEAT} \tag{2.11}$$

$$\frac{Ds}{Dt} = \mathbf{Q_s} \quad \text{SALT} \tag{2.12}$$

$$\rho = \rho(s, \theta, p) \quad \text{STATE} \tag{2.13}$$

where ρ_0 is a constant reference density (in this case: 1029 $kg\ m^{-3}$), $\vec{v}$ is the three-dimensional velocity vector, $\vec{\Omega}$ is the planetary angular velocity vector ($|\Omega| = 7.3 \times$

$10^{-5} rad\ s^{-1}$), g is the gravitational constant, p is pressure, η is the displacement of the free-surface from the resting sea level and H is the bottom depth. $\mathbf{F}$, $\mathbf{Q}_\theta$ and $\mathbf{Q_s}$ represent the wind-stress, the net and shortwave heat and the net freshwater forcing fluxes.

Note that these are the equations for an incompressible ocean ($D\rho/Dt << \rho\nabla.\vec{v}$) and the Boussinesq approximation $\rho\vec{v} \longrightarrow \rho_0\vec{v}$ has been made. The Boussinesq approximations, attributed to *Boussinesq* (1903), can be summarized as follows:

(a) The fluctuations of density are primarily due to thermohaline effects.

(b) In the momentum and mass conservation equations, density variations may be neglected, except in terms related to buoyancy force. In other words, the density variations due to dynamics are much smaller than the reference density and thus $\rho \longrightarrow \rho_0$, except when there is a multiplying factor g in the momentum equations (*Gill*, 1982).

The MITgcm has a non-hydrostatic (NH) capability which means that all the terms from the incompressible Navier-Stokes equations (Eq. 2.8 to 2.13) are retained. Because of the large-scale nature of the processes studied in this work, such an approximation is not necessary and the hydrostatic version is used instead. The reader can find more details on the NH capability and algorithm description of the MITgcm in *Marshall et al.* (1997a,b).

In this thesis, we use only the ocean part of the MITgcm. The interaction with the atmosphere can be prescribed either through fluxes of momentum (τ), sensible and latent heat (Q_s, Q_l), fresh water (evaporation minus precipitation minus continental run-off: S_{flux}), or via using bulk formulae that use parameters measured in the atmospheric surface layer, such as wind velocity (u, v), air temperature (T_a), air humidity (q) and precipitation. Downward longwave and shortwave fluxes are needed in both cases. In this work, the state of the atmosphere is prescribed and bulk formulae are used to compare it with the fluxes of momentum, sensible and latent heat, the latter two as follows:

$$\begin{aligned} Q_s &= \rho_{air} C_{p_{air}} u_{sfc} C_u C_T (T_{ref} - T_{sfc}) \\ Q_l &= \rho_{air} L u_{sfc} C_u C_q (q_{ref} - q_{sfc}) \end{aligned} \tag{2.14}$$

where ρ_{air} is the surface air density, the subscript "sfc" indicate the values at the surface, L is the latent heat constant, which depends on the state of the surface: vaporization for open water or formation and evaporation of ice; $C_{p_{air}}$ the specific heat capacity of dry air; and C_u, C_T and C_q are the turbulent exchange coefficients estimated following *Bryan et al.* (1996) and the numerical scheme of *Hunke and Lipscomb* (2002) (see MITgcm manual).

The MITgcm runs were performed on a high performance computer called Tornado located at the German Climate Computing Centre (Deutsches Klimarechenzentrum GmbH, DKRZ) in Hamburg. The Tornado system is a cluster, which means that it is a collection of independent computer nodes that are connected to a common (high-speed) network. It is built to use MPI libraries so that the model computations can be distributed over many processors. The Linux-cluster has 256 compute nodes and 32 GB memory per node. The storage of files used and/or produced by the computations is provided by a high-capacity parallel file-system, accessible by all nodes.

2.6.2 Model setup

The run is described in detail by *Serra et al.* (2009) and is based on the coupled sea ice-ocean MIT general circulation model (*Marshall et al.*, 2004) configured for the Atlantic Ocean north of 33° S including the Mediterranean Sea, the Nordic Seas and the Arctic Ocean. The model features a curvilinear grid with one pole situated over North America and a second pole over Europe, this way solving the singularity at the North Pole.

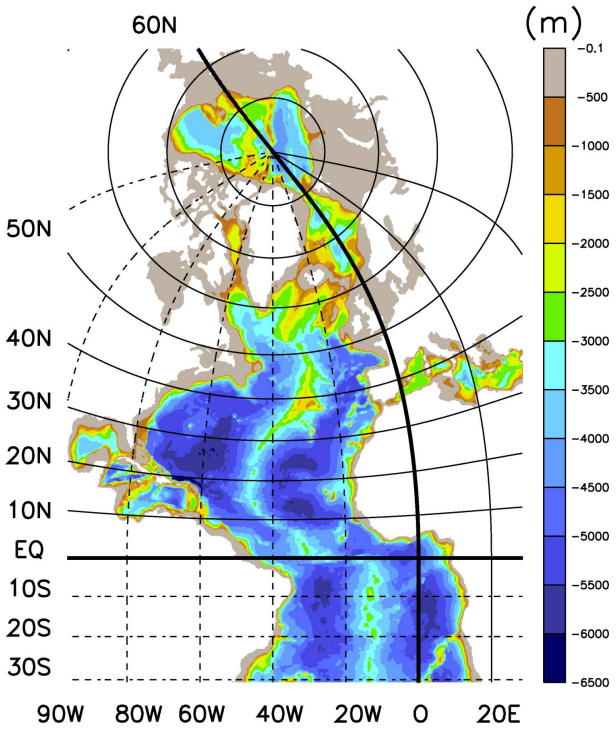

Figure 2.13: Model domain and bathymetry from the *Smith and Sandwell* (1997) dataset.

The model is eddy-permitting with a horizontal resolution of about 15 km throughout the entire domain and 50 levels with vertical resolution varying from 10 m in the upper ocean to 550 m in the deep ocean. The model bottom topography derives from ETOPO2 and the initial temperature and salinity conditions from the World Ocean Circulation Experiment (WOCE) Global Hydrographic Climatology (*Gouretski and Koltermann*, 2004). The model is forced at the surface by fluxes of momentum, heat and freshwater computed using bulk formulae and the 6-hourly atmospheric state from the NCEP/NCAR Reanalysis-1 (*Kalnay et al.*, 1996). At the volume-balanced open northern and southern boundaries, the model is forced by a 1° resolution global version of the MITgcm forced by the same NCEP dataset. The model SST is relaxed to the monthly Extended Reconstructed SST V3 database (*Smith et al.*, 2008) and the model sea surface salinity to the World Ocean Climatology 2005 monthly climatology (*Boyer et al.*, 2005) with a relaxation time scale of 1 month. Vertical mixing is parameterized by the KPP formulation of *Large et al.* (1994). Background coefficients of vertical diffusion and viscosity

are $10^{-6}m^2s^{-1}$ and $10^{-5}m^2s^{-1}$, respectively, and the coefficients of horizonal diffusion and viscosity are both $10^{11}m^4s^{-1}$. The model domain and bathymetry are shown in Fig. 2.13.
The model output is available over the period 1948-2008. For our work, the period 1998-2006 is used when performing comparisons with the observed SST, and the period 2000-2006 when the AOD is included in the analysis.

2.6.3 Results from 3D eddy-permitting simulation

We use the model SST in the area of our study to see if the differences between the observed (with the microwave satellite sensor) and simulated (by the model) SST can be brought in closer relation with Saharan dust than we have been able to do with the KPP-1D model. We recall that the NCEP reanalysis forcing does not include the effect of Saharan dust on the surface radiative forcing of the eastern North Atlantic, but otherwise leads to a realistic estimate of air-sea interaction, i.e., the model results can be used as an estimate of the local and non-local SST anomalies forced by ocean dynamics as well as by changes in the surface fluxes of heat, freshwater and momentum, all not related to dust.

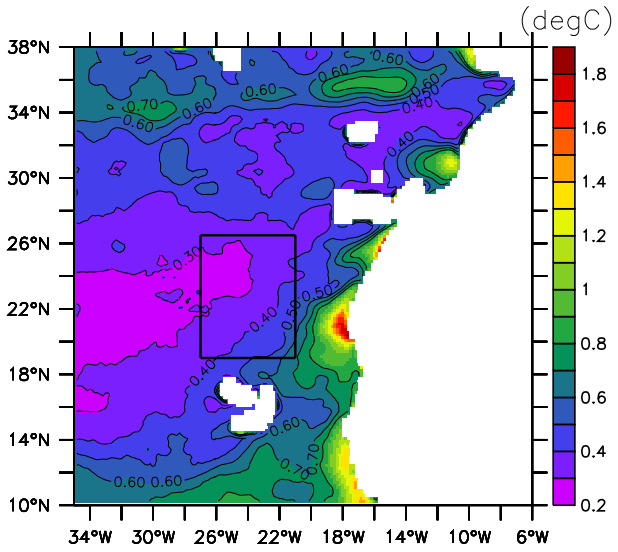

Figure 2.14: Distribution of the difference between the root mean square (rms) of the TMI SST and the simulated SST (in ° C). Contours are drawn between 0.2 and 0.8° C (C.I. = 0.1° C). The black square indicates the area where the time series averaging is performed.

Before using simulated SST fields to identify dynamical SST anomalies, we need to test the model's skill against observed SST variations derived from microwave radiometry. To proceed in this direction we show in Fig. 2.14 the differences in the root-mean-square (rms) SST variability between the TMI SST and the simulated SST for the period 1998-2006 (we show the difference in the rms variability rather than the rms SST difference, because any phase shift in SST would immediately result in a big SST difference). The

large differences in *rms* SST variability, occurring close to the coast and extending offshore at about 18° N, might be attributable to the inability of the model (due to lack of resolution and/or spatial variability in surface wind forcing) to simulate correctly the coastal upwelling filament off Cape Blanc (*Kostianoy and Zatsepin*, 1996; *Marchesiello and Estrade*, 2009). We also note that this region shows a good correlation between the weekly means of AOD and the differences between the TMI SST and the simulated SST (Fig. 2.15a), but this result is likely not related to dust-induced anomalies in SST but to model biases. As a consequence, we will exclude it from the further inter-comparisons involving model fields.

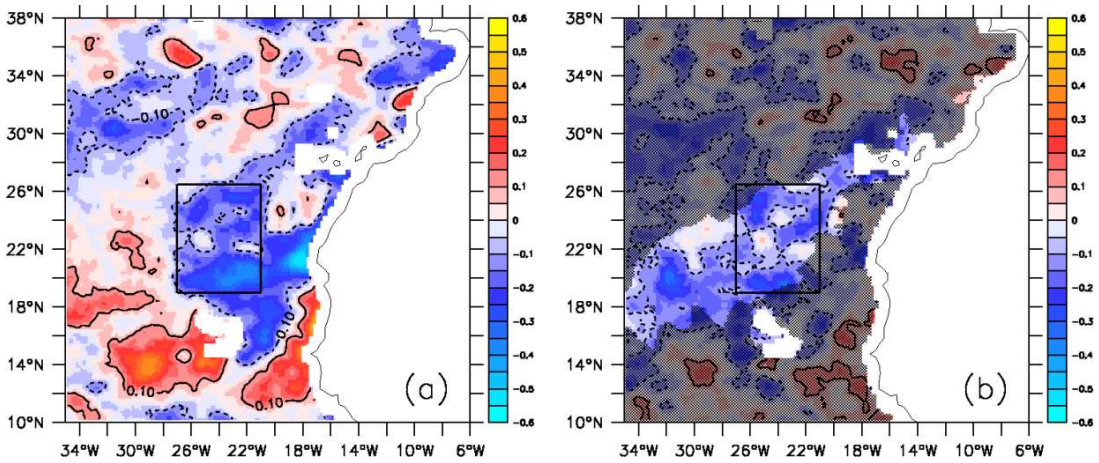

Figure 2.15: Distribution of local correlations between: (a) AOD and TMI SST minus simulated SST; (b) anomalies of AOD (relative to AOD seasonal cycle) and anomalies of TMI SST (relative to TMI seasonal cycle) minus anomalies of simulated SST (relative to the simulated SST seasonal cycle). Correlation coefficients larger than ±0.1 are significant with 95% confidence level and denoted with the full and dashed black contours. The hatched area (b) corresponds to a superposition of the following: pixels where the percentage of the MODIS AOD retrievals is less than 55%; pixels where the AOD anomalies are smaller than 0.5 more than 35 times (i.e: days); areas where the SST *rms* difference of Figure 10 is higher than 0.45°C. The black box in both cases indicates the region where the spatial averages are performed.

However, outside the immediate coastal vicinity, SST *rms* differences quickly reduce to small values (< 0.3° C), suggesting that the model is well capable to simulate the observed SST variations outside the immediate shelf regions. The correlation between the SST differences and AOD is high offshore, showing significant negative correlations in the main dust deposition area (see box in Fig. 2.15a). The positive correlations further south are likely due to other processes unrelated to dust. High correlations between SST differences and AOD time series can also be observed in the main dust area (indicated by absence of hatching in Fig. 2.15b) after removing a climatological seasonal cycle from both time series, which suggests a statistically significant relationship between the AOD and the (observed - simulated) SST differences. Correlation coefficients larger than ±0.1 are significant at a 95% confidence level.

To further highlight the data-model differences and their relation to dust, we show in Fig. 2.16, as a function of time, the difference between the observed SST and those simulated by the model (black line) together with the weekly averages of MODIS AOD, after averaging both fields over 21° W - 27° W; 19° N - 26.5° N (black box in Fig. 2.15a. We note that the SST difference in this box shows only a small regular seasonal cycle and primarily interannual variability superimposed to sub-seasonal changes. The same holds for the AOD time series and both are correlated (see Fig. 2.15a). A closer inspection of the SST differences reveals that, in the region enclosed in our box, they are not related to the SST differences evolution in the coastal region, suggesting again that the SST differences we are seeing in Fig. 2.16 are not contaminated by model biases close to the coast but do provide a reasonable estimate of dust-induced SST cooling.

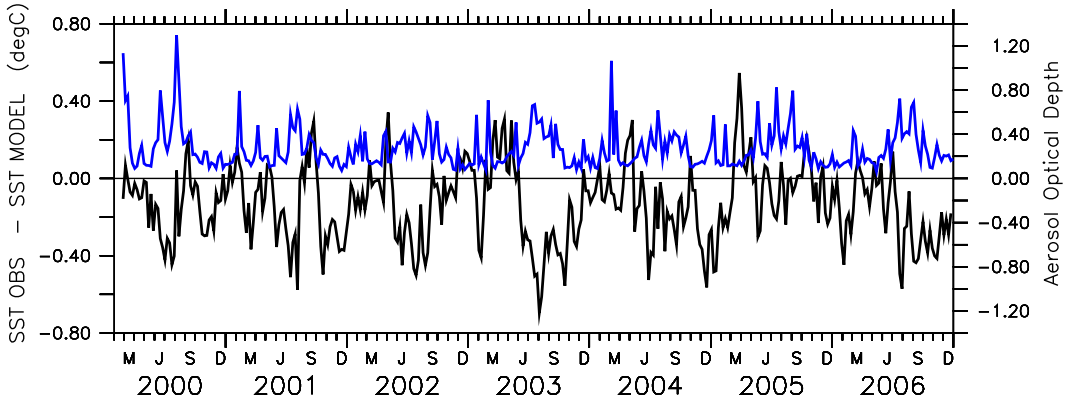

Figure 2.16: Time series of weekly AOD from MODIS (blue) and TMI SST minus simulated SST (black), averaged in the box (27° W - 21° W; 19° N - 26.5° N) for the period 2000-2006.

2.7 Concluding remarks

We have identified several indications of Saharan dust impact on SST in the eastern subtropical North Atlantic. Findings from the previous sections in this chapter can be summarized as follows:

- The comparison between AVHRR and two microwave SST products (TMI and AMSR-E) in a region in the subtropical eastern North Atlantic, showed the AVHRR to be biased cold by as much as 2° C. We found those differences to be associated with periods of enhanced AOD (seasonal or outbreaks), which suggests the dust clouds to be the primary agent for causing the AVHRR SST biases.

- A reduction of SST of 0.2° to 0.4° C simultaneous or shortly after enhanced aerosol loads. This result is consistent with an estimate of SST decrease simulated with a 1D local mixed layer model, during low wind conditions and shallow mixed layer.

- An inspection of the data suggests that about 30% of SST variance could be explained by dust-induced cooling in our study region.
- The integration of a 3D eddy-permitting model of the North Atlantic showed that most of the dynamical SST anomalies present in TMI observations can be simulated and that after removing them from the model output, remaining SST anomalies are consistent with dust-induced cooling not present in the simulations.
- A comparison between our model results and the TMI SST observations suggests a cooling of about 0.5° C on the local SST on sub-seasonal to interannual time scale, which is significantly correlated and consistent with a dust-induced cooling.
- A regression analysis suggests that about 9% of SST variance could be explained by dust-induced cooling in the studied region that is not represented in existing AVHRR SST fields nor represented in reanalysis centers provided surface heat fluxes with which the model is forced.

From our results it appears that the model simulations are biased warm by about 0.5° C in the eastern subtropical North Atlantic due to the neglect of dust loading in the used NCEP atmospheric forcing fields. Moreover, because our model hindcast was relaxed towards the AVHRR SST fields (see also *O'Neill et al.*, 2003, their Fig. 1) that also appear biased cold in our study area (due to dust impact on the retrieval), the still present warm model bias therefore has to be considered a lower bound. It can therefore be expected that the real cooling effect of dust on SST to be even larger than estimated through the model-data comparison shown in Fig. 2.15.

We conclude that significant support was found for a SST decrease associated with the cooling effect of Saharan dust through a comparison of TMI SST observations with results from a numerical simulation not affected by dust-induced cooling.

Chapter 3

Impact of Saharan Dust on the North Atlantic Circulation

3.1 Introduction

Changes of solar radiative transfer into the ocean due to the presence of aerosols alter the forcing of the ocean circulation. It was shown in the previous chapter that an enhanced content of Saharan dust in the atmosphere leads to a cooling at the sea surface due to scattering and absorption of solar radiation in the dust layer. Aerosols in the atmosphere alter the downward shortwave radiation and thus the amount of energy received at the sea surface. Spatial inhomogeneities in the dust content and the consequent induced anomalies in solar radiance, will lead to differential heating of the surface. These spatial inhomogeneities can thereby lead to spatial gradients in the near-surface density of the ocean which, through the thermal wind relation, will cause the ocean circulation to change. In addition, changes of the vertical stratification associated with dust-induced cooling can lead to vertical mixing which by itself can change also the deep density structure and the geostrophic flow field.

We will here investigate the amplitude and time and spatial scales of the local to basin-scale ocean adjustment response, to dust-induced density changes in the subtropical eastern North Atlantic.

In the first part of this thesis we identified several indications of Saharan dust impact in the eastern subtropical North Atlantic SST, using satellite data, a 1-D mixed layer model and a 3-D numerical model (*Martínez Avellaneda et al.*). The 3-D ocean circulation model output was used in an attempt to eliminate dynamical signals in the SST observations to further isolate the dust-induced sea surface cooling. However, we faced difficulties related to model biases, in particular near the African coast, caused by the lack of spatial resolution.

In order to isolate completely the dust-induced effects from the other existing dynamical signals and from model artifacts, we study the impact of dust in the circulation using differences between a control run and a second run, in which a dust-induced perturbation in the shortwave fluxes is imposed in the eastern North Atlantic.

Such perturbation can generate a significant horizontal pressure gradient with subsequent changes in the velocity fields and further changes in meridional transport of heat and volume. In this regard, changes in the Atlantic Meridional Overturning Circulation (AMOC) and Meridional Heat Transport (MHT) are investigated.

The main goals for this second part of this thesis are to investigate:

1. Changes in the local circulation of the subtropical eastern North Atlantic due to differential heating of the surface;

2. Changes in the basin-scale horizontal circulation due to the imposed perturbation in the eastern North Atlantic;

3. Changes in the transport of mass and heat in a basin-scale due to an enhanced east-west pressure gradient.

The chapter is organized as follows: In Section 3.2 we include the experiment setup, results from a coarse resolution simulation and the construction of the dust-induced realistic perturbation. The results for the control run are presented in Section 3.3 and for the perturbed run in Section 3.4. Finally, a discussion and conclusions are presented in Section 3.5.

3.2 Methods

This study is based on the ocean MITgcm discussed in the previous chapter. We perform two eddy-permitting ($1/6^\circ$ spatial resolution) simulations: a control run and a perturbed run. The control run is based on the simulation of *Serra et al.* (2009) described in Chapter 2, with some modifications that will be explained next. The perturbed run incorporates the dust effect by reducing the shortwave fluxes, with which the model is forced, in a region in the subtropical eastern North Atlantic. Our approach is then to investigate the response in the ocean circulation to the dust-induced anomalies by analyzing the differences between the perturbed and unperturbed runs. In this section details of the setup of both runs, the results of a pilot coarse resolution run using a Green's-function method, and the construction of the realistic dust-induced perturbation, are presented. The pilot simulation serves as a starting point when developing the realistic perturbation.

3.2.1 The experimental setup

The model configuration described in Chapter 2, which was available only on a monthly time basis, was restarted from the end of December 1999 and ran until the end of 2003 (this simulation will be referred to as "run1" from here onwards). The net shortwave fluxes (Q_{sw})[1], net heat (Q_{net}), net freshwater (evaporation minus precipitation minus continental run-off) and meridional and zonal wind stress fluxes produced by run1 were written at 6-hour interval and served as forcing for the control run (referred to as "run2" from here onwards).

In brief, the approach to investigate the impact of dust on the ocean was to perform two simulations: an (unperturbed) control run and a perturbed run. The perturbed run incorporates the dust effect by reducing Q_{sw} with which the model is forced (to be explained in detail in Section 3.2.2). We can expect the first order impact of the reduced net Q_{sw} to be a cooling of the ocean surface. The run described in Chapter 2

[1] In the MITgcm the Q_{net} is the sum of all the heat fluxes (i.e.:$Q_{net} = Q_s + Q_l + Q_{lw} + Q_{sw}$) and as such, it includes the Q_{sw}. So one needs to remove Q_{sw} from Q_{net} when using Q_{sw} as a separate forcing (e.g: to make a perturbation).

used a relaxation of temperature and salinity at the surface to the 1948-2008 monthly ERSST V3 and WOA2005 monthly climatology, respectively, which would have the effect of suppressing the perturbation that we want to impose. To have a successful perturbed experiment, the heat and freshwater fluxes have to either account for the extra relaxation fluxes (a), or the relaxation has to be switched off (b):

(a) A relaxation term is added to the prescribed heat (latent + sensible + shortwave + longwave: H_{flux}) and freshwater (S_{flux}) fluxes:

Step 1. The model is forced by fluxes, uses relaxation and the simulated sea surface temperature and salinity (i.e.: SST_{model} and SSS_{model}) are written every time step.

Step 2. New fluxes of heat (H^c_{flux}) and freshwater (S^c_{flux}) are constructed according to:

$$\begin{aligned} H^c_{flux} &= H_{flux} + \rho c_p \Delta h \frac{(SST_{model} - SST_{relax})}{t_{relax}} \\ S^c_{flux} &= S_{flux} - \frac{\Delta h}{35}.\frac{(SSS_{model} - SSS_{relax})}{t_{relax}} \end{aligned} \tag{3.1}$$

where c_p is the specific heat at surface pressure, and $c_p(S = 35, T = 22, p = 0) = 3996 Jkg^{-1}K^{-1}$ (*Gill*, 1982), t_{relax} is the time scale of the relaxation (i.e: 1 month) and Δh is the thickness of the first model layer (10 m). The factor (-1) in the fresh water flux correction is needed because of the sign convention of the NCEP forcing: the flux is positive (negative) for an increase (decrease) in salinity.

Step 3. The relaxation is switched off and the model experiments are forced with the corrected fluxes.

(b) The model runs without relaxation and is forced with the fluxes that run1 produced before using bulk formulae:

Step 1. The model runs with no relaxation and the simulated fluxes are written every 6-hours. Even though the relaxation is switched off, this simulation is forced with the state of atmosphere and bulk formulae, so a large drift in temperature is not likely to be observed.

Step 2. The bulk formulae and the sea-ice package are switched off and a second simulation is conducted forced with the fluxes obtained in Step 1b.

The method (b) was the one applied to the $1/6^\circ$ simulation. Because of the absence of bulk formulae and the sea ice-package in run2, a validation against the results produced in run1 was carried out. No significant drift was observed in any of the oceanic variables tested (i.e., temperature, salinity, sea surface height) in run2. The simulated period corresponds to January 2000 to December 2003.

The method (a) was applied to a coarse resolution simulation which served as a pilot experiment and it is discussed next.

Pilot Simulation

In this case, the MITgcm was configured for the Atlantic Ocean between 30° S and 65° N including the Mediterranean Sea. The spatial resolution is 1° x 1° and it has 50 levels in the vertical with a resolution of 10-m in the upper layers to 456-m in the deepest layer. The topography was also derived from the same data base as used in the 1/6° simulation. In this simulation, fluxes of momentum, shortwave, longwave, sensible and latent heat and freshwater fluxes are prescribed from the NCEP RA1 reanalysis (*Kalnay et al.*, 1996) and so bulk formulae were not used. The open southern and northern boundaries were forced with a global solution of the MITgcm at 1° resolution (ECCO, iteration 69). The sea surface temperature and salinity were relaxed to the monthly Levitus World Ocean Atlas 2001 (WOA2001 *Conkright et al.*, 2002) dataset. The model was initialized from rest and with the annual mean temperature and salinity from WOA2001, and was run for a period of 5 years (1992-1996).

The aim of this simulation was to test the sensitivity of the North Atlantic ocean circulation to an analytical Gaussian perturbation imposed in the eastern basin. The perturbation represents a reduction (in %) of the forcing shortwave fluxes and is displayed in Fig. 3.1. The philosophy of this experiment is similar to that of a Green's-function (GF) method (*Wunsch*, 1996; *Menemenlis and Wunsch*, 1997; *Menemenlis et al.*, 2005). A GF is the gradient of the ocean state with respect to a parameter, in this case the shortwave flux, and represents the sensitivity of the ocean state to it. The perturbation was applied for a month (i.e.: July 1992) and then switched off.

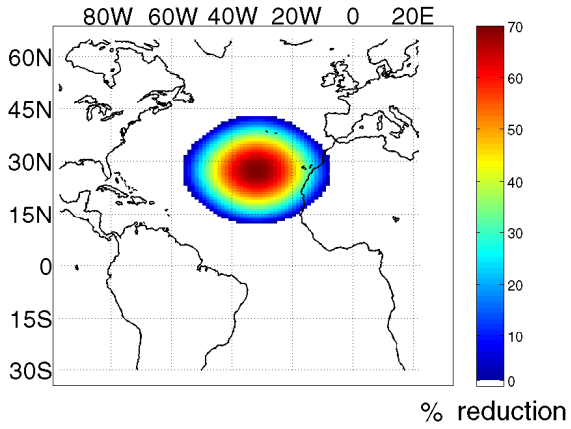

Figure 3.1: Gaussian perturbation in the Northeastern Atlantic in a coarse resolution run of the MITgcm. Units are in % indicating maximum reduction of 70% in the center and decreasing to 0 at the periphery.

The resulting differences in sea surface height between the perturbed and unperturbed runs are shown in Fig. 3.2 for different dates. The first order impact is to depress the ocean surface (Fig. 3.2a). A week after the perturbation was switched off, we can observe Kelvin waves propagating along the coast of Portugal and United Kingdom, and a signal propagating towards the western basin. After 5 months, an advection towards

the west and the southeast is observed, and a weaker signal seems to have reached the eastern coast again after propagating around the basin. The ocean state after one year (Fig. 3.2d) shows the initial perturbation being advected westward following the main patterns of the general circulation and an eddy-like activity shows up in the Gulf Stream region.

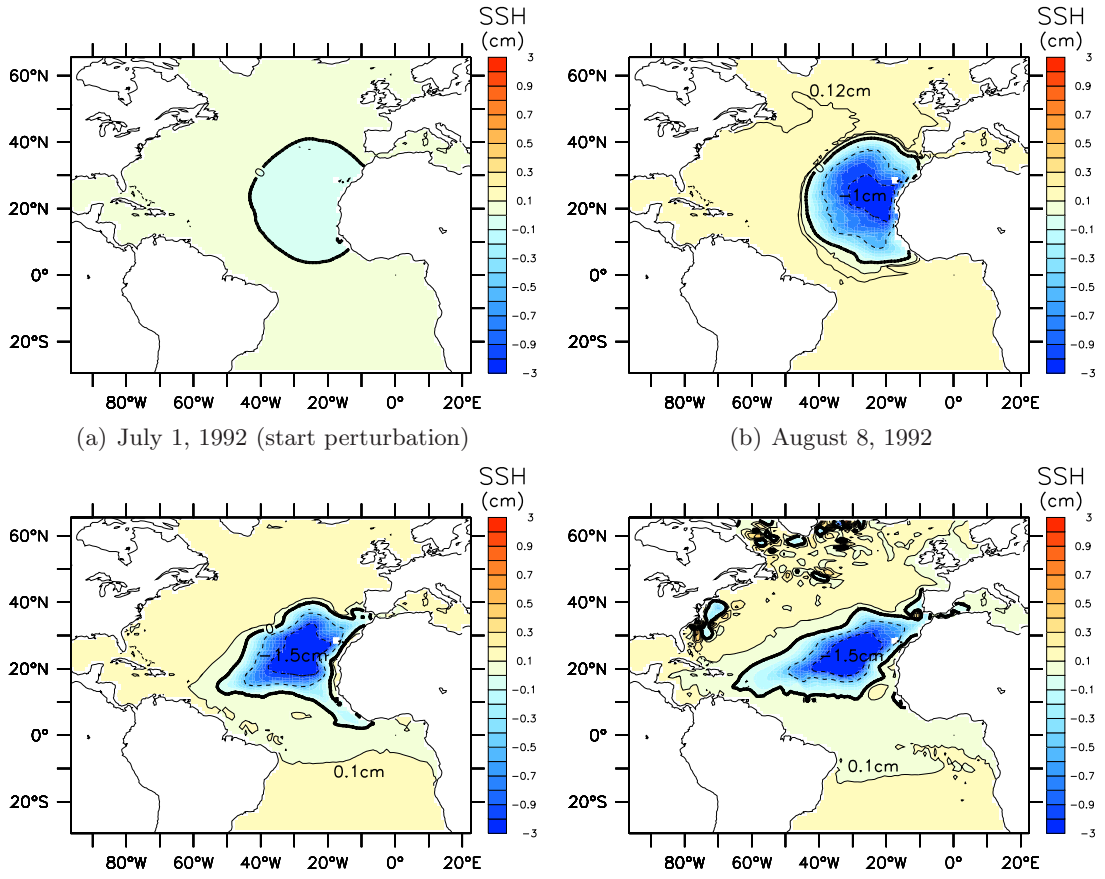

(a) July 1, 1992 (start perturbation)

(b) August 8, 1992

(c) December 31, 1992

(d) July 1, 1993

Figure 3.2: Distribution of sea surface height differences (in cm) between the perturbed (Fig. 3.1) and the control runs of the 1° MITgcm simulation. The color scale varies between ±0.95cm and the last level corresponds to values between ±0.95cm and ±3cm.

The results of this pilot simulation suggest that a response in the ocean circulation due to a perturbation in the subtropical eastern North Atlantic can be expected. In this example, however, a coarse resolution model with prescribed fluxes was used, and the perturbation was analytical and switched off after a month (i.e., a delta pulse). The challenge was then to perform simulations with a 1/6° resolution eddy-permitting version of the MITgcm and to perturb it with time series of realistic dust-induced shortwave flux anomalies.

3.2.2 Construction of a realistic perturbation

The 1/6° perturbed run (referred here to as "run3") incorporated the dust effect by reducing the Q_{sw} fluxes with which the model is forced.

The dust-induced shortwave perturbated fluxes ($\tilde{Q}_{sw}$) are estimated according to:

$$\begin{aligned} \tilde{Q}_{sw}(t) &= Q_{sw}(t)(1 - ARF(t)/Q_{sw_{max}}(t)), \\ \text{with} \quad ARF(t) &= f_e \times AOD(t) \end{aligned} \tag{3.2}$$

where AOD is the product from MODIS, f_e is the radiative forcing efficiency, $Q_{sw}(t)$ is available every 6-hour from run1 and $Q_{sw_{max}}$ is the radiation value at noon (see also the Section 2.5 from the previous chapter).

The f_e has a known seasonal variability in the eastern subtropical North Atlantic (*Li et al.*, 2004; *Yoon et al.*, 2005; *Zhu et al.*, 2007), therefore, in principle, it should be time dependent. Monthly means of f_e are not available at present and can only be obtained by extrapolating in time and space those provided in the bibliography, such as shown in Fig. 2.5. However, even if we take such interpolation to be acceptable, we would have to interpolate monthly means to 6-hourly data and we do not have enough information about the f_e behavior in order to choose a proper interpolation method. We decided to simply use a constant value of f_e=-40 $Wm^{-2}AOD^{-1}$, which is accepted to represent well the annual mean of f_e (Ina Tegen, personal communication). Therefore, $\tilde{Q}_{sw}$ depends only on the AOD concentration in the atmosphere.

Fig. 3.3 shows an example of MODIS-AOD distribution in the North Atlantic. The gaps in the distribution of the daily AOD retrievals would generate discontinuities in the forcing, and thus, an artifical response to the ocean circulation. So firstly, we constructed weekly composites of AOD (Fig. 3.3e), and secondly we performed a linear interpolation in the zonal direction to fill the gaps that were still present in the weekly means. Finally, the resulting AOD was interpolated to 6-hourly time series and $\tilde{Q}_{sw}$ calculated through Eq. 3.2.

The goal of our work it to study the response of the Atlantic to a perturbation in the eastern side of the basin. Hence a mask is applied to the distribution of AOD, as indicated on the left panel of Fig. 3.4. On the right panel, the figure displays the resulting distribution of the spatially and temporally interpolated AOD for March 1, 2000.

Fig. 3.5 shows an example of the calculation for March 1, 2000 on the model grid. In (a) we can see the distribution of the Q_{sw} fluxes at noon on the entire grid (i.e., 750 x 864 grid points). The mask is applied in the remaining panels. Fig. 3.5b, d and e show the distribution of the maximum Q_{sw}, the MODIS-AOD, and the reduction in Q_{sw}, respectively. It can be seen from the figures that the spatial patterns between (d) and (e) are, as expected, the same and that the dust-induced forcing can account for a reduction of about 85 Wm^{-2}.

An example of the daily cycle of the forcing in the control and the perturbed runs can be observed in Fig. 3.5c for a region off the African coast and, in Fig. 3.5f), for the western Atlantic. The maximum difference between the runs ($\sim$ -50 Wm^{-2}) off the African coast is, as expected, observed at noon. The time series of Q_{sw} in (f) shows no difference on that date, given that it was extracted from a location that is not directly affected by the perturbation.

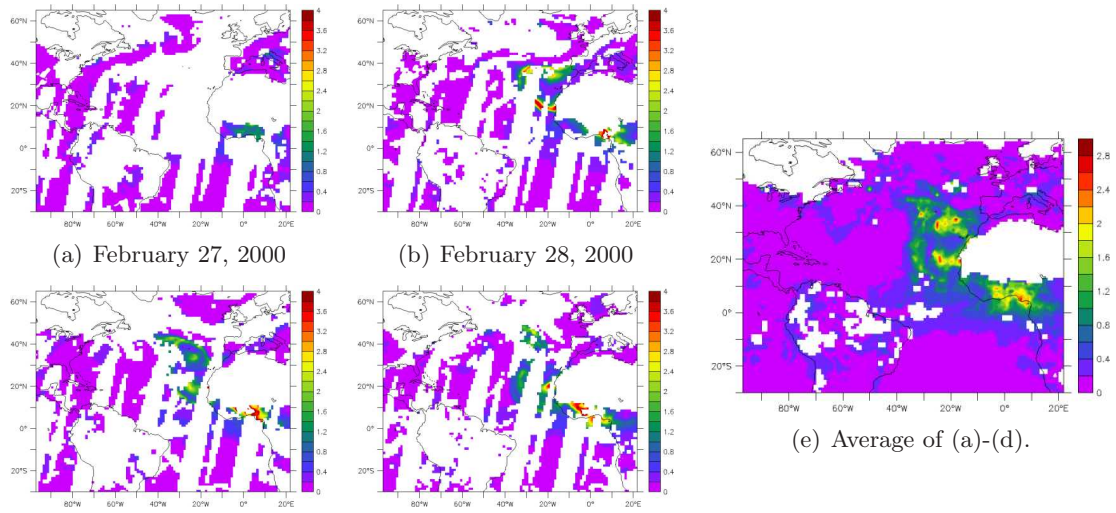

(a) February 27, 2000 (b) February 28, 2000

(c) February 29, 2000 (d) March 1, 2000

(e) Average of (a)-(d).

Figure 3.3: Distribution of daily MODIS-AOD for the period February 27, 2000 to March 1, 2000 (a-d), and distribution of the corresponding weekly mean for those days (e).

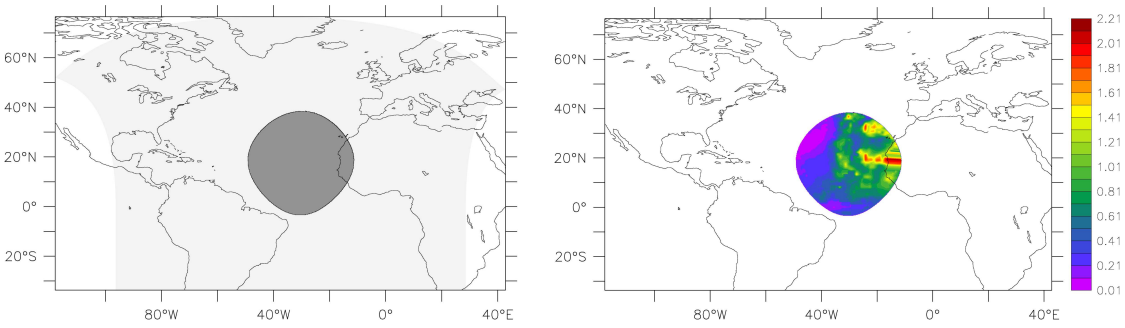

Figure 3.4: (left) Mask in the model grid and (right) the distribution of the Aerosol Optical Depth after the mask is applied. The AOD distribution showed here corresponds to March 1, 2000 and is the daily AOD interpolated from the "gap-free" weekly product.

We have thus constructed time series of dust-induced anomalies in the Q_{sw} fluxes according to Eq. 3.2, for the period February 26, 2000 to December 31, 2003. The start date of the perturbation was chosen according to the availability of the AOD product from MODIS.

Because the Q_{sw} anomalies depend on the AOD variability, we provide in Fig. 3.6 the distribution of the root-mean-square (rms) of the daily interpolated AOD. The largest variability is observed along the path of the seasonal Saharan dust, (i.e, zonal plume between ∼15° N - 25° N for high dust and ∼5° N - 10° N for low dust season) with the maximum (>0.25) located closer to the coast. Relatively large rms values (>0.09) can

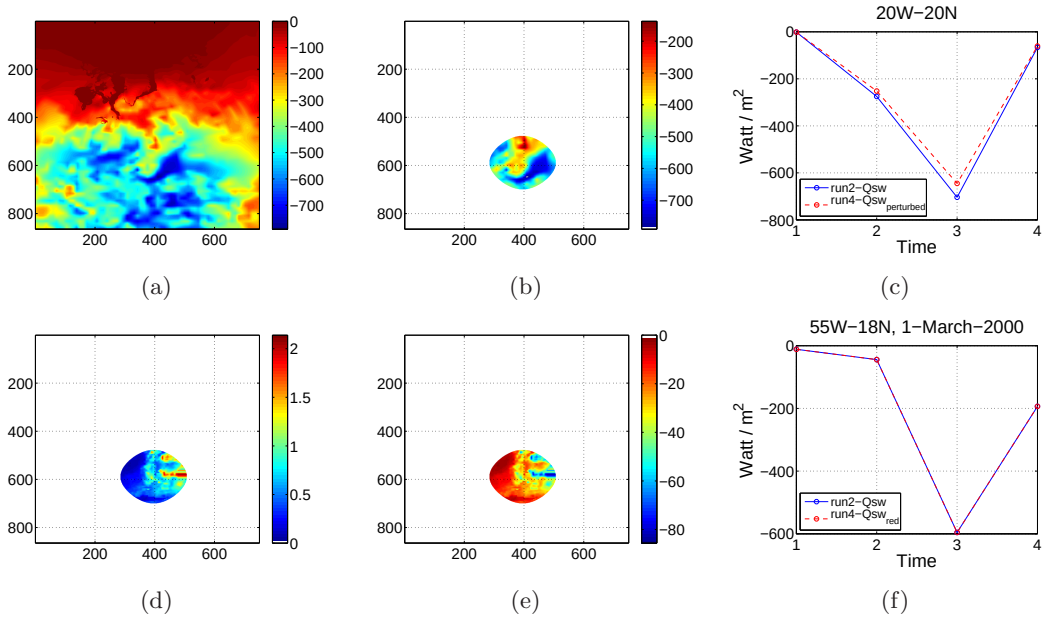

Figure 3.5: Distribution of: (a) Q_{sw}, (b) $Q_{sw_{max}}$, (d) MODIS-AOD, and (e) the reduction in Q_{sw} (i.e.: $f_e.AOD/Q_{sw_{max}}$) for March 1, 2000. Time series of the daily cycle of Q_{sw} (blue, run2) and $\tilde{Q_{sw}}$ (red, run3) for March 1, 2000, are shown in (c) and (f) at locations 20° W - 20° N and 55° W - 18° N, respectively.

also be found on the eastern side of the perturbation north of 25° N, which correspond to the location of the dust outbreaks.

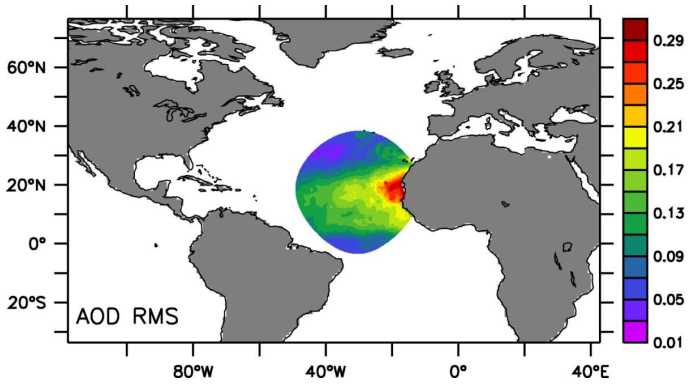

Figure 3.6: Distribution of the root-mean-square (rms) of the daily interpolated AOD in the perturbed region.

In addition to the radiation-induced forcing incorporated here, the dust accounts for other effects, such as:

(1) Enhanced longwave downward radiation from the dust's thermal emission (*Vogelmann et al.*, 2003; *Zhu et al.*, 2007);

(2) changes due to dust-induced fertilization in the ocean;

(3) enhanced turbidity in the ocean due to dust deposition and further sinking;

(4) changes in the vertical profile of absorption of light due to (2) and (3).

We are aware of these dust-induced changes in the system and that some of them might be equally important as the one taken into account in this work. However, an experiment that includes all these components is beyond the scope of this thesis and only the first order impact on the Q_{sw} is incorporated.

A summary of the experiments carried out in this chapter is displayed in Table 3.1.

Table 3.1: Summary of model experiments at 1/6° resolution performed in this work.

	Serra et al. (2009) modified (run1)	Control Run (run2)	Perturbed Run (run3)
Bulk formulae	YES	NO	NO
Sea ice package	YES	NO	NO
Relaxation	OFF	OFF	OFF
Forcing	NCEP/NCAR	Fluxes from run1	As run2 + $\tilde{Q}_{sw}$

3.3 Mean ocean circulation

In this section, we show and describe the state of the ocean at the moment the perturbation is switched on, as well as the mean circulation and sources of large variability in the ocean, as they result from the MITgcm control run. In every case, the variables were regridded from the model curvilinear grid onto a regular longitude-latitude grid and the averages for the entire simulated period (2000-2003) for the control run were computed.

Fig. 3.7 shows the surface density in March, 2000. The black circle indicates the region where the perturbation was imposed. This figure gives us an idea of how the ocean is likely to respond after the buoyancy perturbation on the east starts. The density outcrops inside the black circle present a strong meridional gradient, ranging from ~ 26 at about 30° N to ~ 22.5 at about 10° N. In addition, a vertical profile of σ_θ at 27° N (not shown) is homogeneous in the vertical, in contrast to the situation in the south. A deeper subduction of dust-induced anomalies is, therefore, expected in the northern part of the perturbed area.

The zonal and meridional velocities integrated in the first 100 m shown in Fig. 3.8a represent the surface/sub-surface velocity distribution. Also is the mean distribution of the streamfunction for the vertically integrated mass transport between the surface and 40 m depth (ψ_{sfc-40}, Fig. 3.8b) defined as:

$$\psi_{sfc-40}(x,y) = \int_{east}^{x} \int_{0}^{40m} v(x,y,z)\, dz\, dx \tag{3.3}$$

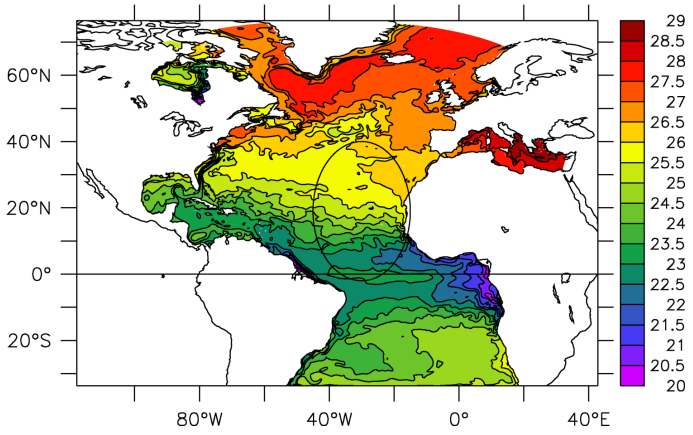

Figure 3.7: Average surface density in $kgm^{-3} - 1000$ for the control run in March 2000.

where $v(x, y, z)$ is the meridional component of the velocity at each grid point. The advantage of plotting the distribution of a streamfunction is that it is straightforward to interpret the characteristics of the flow: it flows parallel to the streamlines and the volume flow rate is numerically equal to the differences in their ψ values. In particular, the streamlines in the first 40 m of the ocean give us an idea about where we can expect the sea surface temperature anomalies generated by the perturbation to circulate.

The North Atlantic surface circulation is highly complex and it has been documented extensively in the literature. It is basically composed of an anticyclonic subtropical gyre, a cyclonic subpolar gyre and the equatorial system. We will provide here a description of those parts of the Atlantic on which our attention is focused. A blow up of Fig. 3.8a and/or schematic circulation sketches will be provided when needed.

Equatorial Atlantic Circulation

The equatorial Atlantic is a region dominated by the presence of large westward currents and eastward countercurrents (Fig. 3.9).

The equatorial Atlantic surface circulation is limited by the northern and southern edges of the southern and northern hemispheres subtropical gyres, respectively (see *Stramma et al.*, 2003). The classical view of the surface currents in the equatorial Atlantic can be seen in Fig. 3.9a: it shows westward flowing North and South Equatorial Currents (NEC, SEC), which respectively feed the poleward western boundary currents (i.e.: the Gulf Stream and the Brazil Current) and eastward flowing North and South Equatorial Counter Currents (NECC, SECC not shown in the surface distribution). Note that only the northernmost part of the Brazil Current can be seen in the simulated circulation.

The NEC originates from the northwestern coast of Africa and is found in our simulated circulation between 10° N - 23° N, which is 3° shifted to the north compared to *Schott et al.* (2002). As the NEC travels across the open ocean, it is joined by waters originating south of the equator thus entraining waters from the Southern Atlantic into the Northern Atlantic. The various pathways of cross-equatorial water mass exchange will not be discussed here. Most of the NEC water flows westward at a mean velocity between

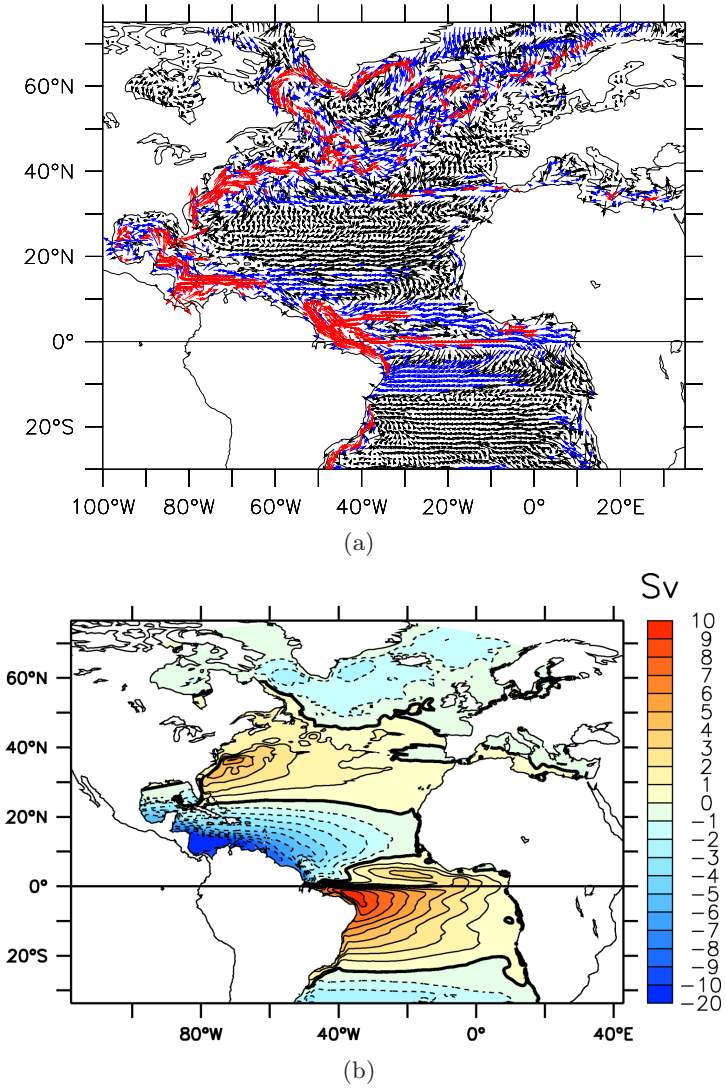

Figure 3.8: (a) Ocean velocity distribution averaged over the top 100 m. The red arrows represent velocities with an intensity between 150 and 15$cm\ s^{-1}$, the blue arrows between 15 and 5$cm\ s^{-1}$, and the black arrows represent velocities which intensity was lower than 5$cm\ s^{-1}$. (b) Stream function distribution integrated between the surface and 40 m. Positive (negative) values denote clockwise (anti-clockwise) circulation. In both cases, the calculation was performed from monthly averages calculated from the daily output of the control run, and then averaged over the 4 years of simulation (2000-2003).

4-8 $cm\ s^{-1}$ and feeding the Caribbean system and some of it is observed to retroflect cyclonically to join the NECC.

The SEC flows westward between 25° S and 4° N at a mean surface velocity of 11.3 $cm\ s^{-1}$. The southern branch of the SEC is fed by the Benguela Current flowing northward along the South African coast, which only shows its northernmost part in our

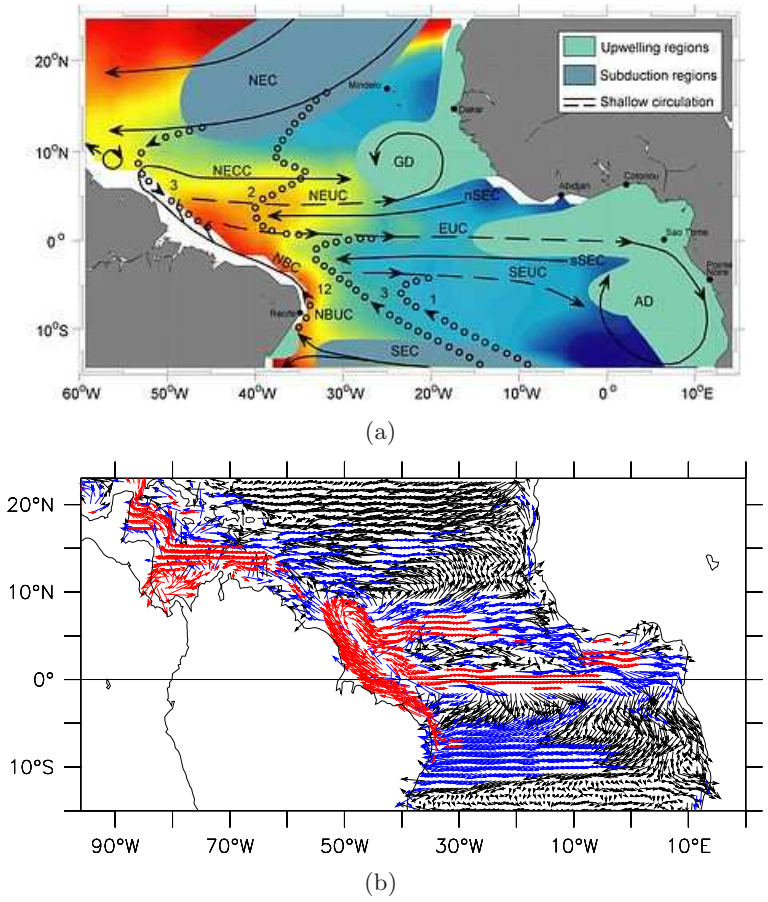

Figure 3.9: (a) Schematic (from *Schott et al.*, 2004) and (b) simulated mean surface circulation in the Equatorial Atlantic. In (a),the NEUC and SEUC not mentioned in the text, represent the North and the South Equatorial Undercurrent, respectively. In (b) the red arrows represent velocities with an intensity between 90 and $12cm\ s^{-1}$, the blue arrows between 12 and $5cm\ s^{-1}$, and the black arrows represent velocities which intensity was lower than $5cm\ s^{-1}$.

simulated portion of the Atlantic (Fig. 3.8b). The SEC then flows westward towards the Brazilian coast where it bifurcates (∼16° S) into the North Brazil Current (NBC) and the Brazil Current to the south. The NBC flows along the northern coast of Brazil and, when crossing the equator, a component retroflects eastward into the Equatorial Undercurrent (EUC). The NBC continues to flow northwestward until approximately 7° N, 48° W when it retroflects eastward to feed the NECC, which in turn helps feeding the SEC. The NBC retroflection is well represented by the model, which shows mean velocities larger than 30 $cm\ s^{-1}$. During the retroflection, eddies, called NBC Rings, are formed (*Condie*, 1991; *Schott et al.*, 1998; *Memery et al.*, 2000). These rings may be responsible for more than half of the interhemispheric exchange of mass and heat associated with the Meridional Overturning Circulation's upper limb (*Garzoli et al.*, 2003; *Lumpkin and Garzoli*, 2005), and are well represented by the model (see region between

60° W - 55° W; 7° N - 12° N in Fig. 3.9b).

The EUC is a strong subsurface current flowing eastward at the equator. It is fed by the NBC's retroflection and by the NEC. Our Fig. 3.8b represents the first 100 m and thus, the EUC is visible and shows eastward mean velocities larger than 20 $cm\ s^{-1}$ with a maximum located at 25° W, 2° N.

Western Boundary Circulation

In the equatorial Atlantic, water flows towards the Caribbean Sea from the east at a mean velocity of 45 $cm\ s^{-1}$ (Fig. 3.10a). The velocities rise up to 85 $cm\ s^{-1}$ in the counter-clockwise circulation of the Colombia-Panama Gyre, which is clear offshore of southern Central America (Nicaragua, Costa Rica, and Panama) and northern Colombia. The flow turns northwestward entering the Gulf of Mexico, where it splits into a western branch which recirculates inside the Gulf of Mexico, and an eastern one which becomes the Loop Current. The Loop Current then becomes the Florida Current as it exits the Gulf of Mexico through the Straits of Florida (*Molinari and Morrison*, 1998). The Florida Current then stretches up to Cape Hatteras ($\sim$ 35° N), showing mean surface velocities of 130 $cm\ s^{-1}$. The Gulf Stream (*Stommel*, 1958) begins upstream of Cape Hatteras, where the Florida Current ceases to follow the continental shelf.

The Gulf Stream separation at Cape Hatteras is clearly documented as a persistent feature by the available data (*Dengg et al.*, 1996, and references therein). Fig. 3.10a shows the Gulf Stream separation a couple of degrees shifted to the north. To the north and to the south of the separated Gulf Stream, we observe clearly the Northern and Southern Recirculation Cells (NRC, SRG), which recirculate 10-30 Sv and 20-25 Sv, respectively (Fig. 3.10b). The Gulf Stream transport varies not only in space, but also in time. According to Geosat altimetry results, the current transports a maximum amount of water in fall and a minimum in spring, (*Kelly and Gille*, 1990; *Kelly*, 1991; *Hogg and Johns*, 1995). The mean simulated Gulf Stream velocity and transport maxima are reached near 65° W, and are about 95 $cm\ s^{-1}$ and 60 Sv, respectively. After the separation from the coast, the Gulf Stream continues to flow eastward branching into the North Atlantic Current and the Azores Current.

Eastern Boundary Circulation

The eastward Azores Current is the main recirculating current in the eastern North Atlantic subtropical gyre and is located around 35° N (Fig. 3.8a). The Azores Current turns south, splitting into several branches, the easternmost branch becoming the Canary Current. The Canary Current flows south parallel to the African coast, and recirculates into the interior ocean at approximately 20° N - 25° N to feed the NEC (see *Stramma and Muller*, 1989; *Hernández-Guerra et al.*, 2002; *Knoll et al.*, 2002, and references therein). The simulated Azores Current shows a portion entering the Mediterranean Sea, but such characteristic has not yet been supported by observations.

Associated with the north and south equatorial subsurface counter currents are two cyclonic gyres observed in the eastern tropical Atlantic off Senegal and off Angola. These correspond, respectively, to the thermal upwelling domes called Guinea Dome (GD) and Angola Dome (AD). These domes are characterized by an upward movement of the thermocline, though it never reaches the surface (*Mazeika*, 1967), and are both represented in Fig. 3.9a and partially in Fig. 3.9b.

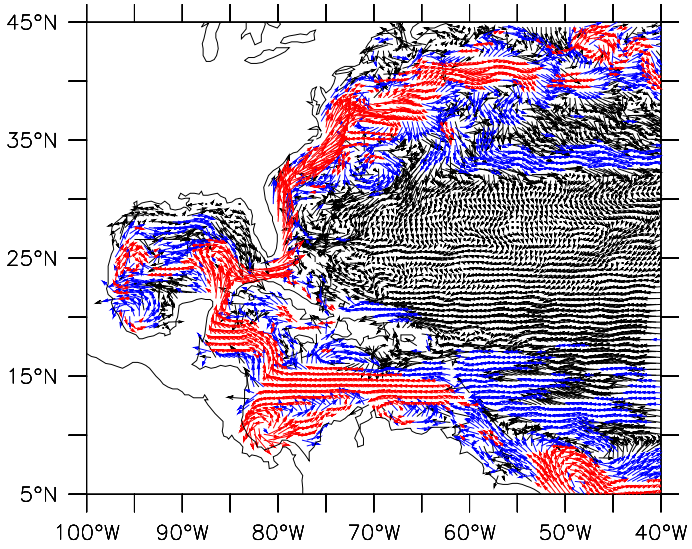

(a)

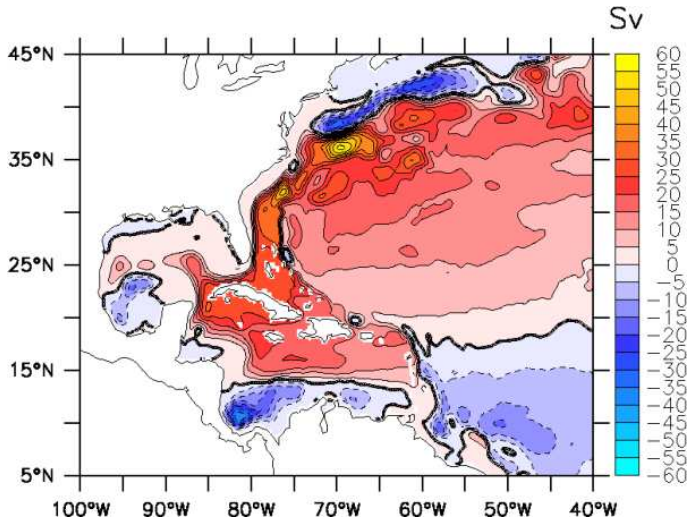

(b)

Figure 3.10: Circulation (a) and barotropic streamfunction (b) distribution for the western North Atlantic. In (a) the red arrows represent velocities with an intensity between 130 and 12$cm\ s^{-1}$, the blue arrows between 12 and 5$cm\ s^{-1}$, and the black arrows represent velocities which intensity was lower than 5$cm\ s^{-1}$.

Eddies, Instabilities and Waves in the North Atlantic

The large-scale ocean circulation is governed almost everywhere by a broad spectrum of intense low-frequency fluctuations (*Stammer and Böning*, 1996). The mesoscale part of the spectrum, roughly corresponding to time scales of 20 to 150 days and spatial scales of 50 to 500km, exhibits high concentration of energy. *Schmitz and Luyten* (1991) for instance, report the kinetic energy in the mesoscale (due to currents, meanders and eddies)

part of the spectrum to exceed that of the time-mean flow by an order of magnitude or more. Moreover, eddies transport heat and momentum and interact with the main flow field.

The simulations analyzed here (Table 3.1) are of spatial resolution of 15 km, therefore, eddy-resolving in the mid and low latitudes. The distribution of the root-mean-square (rms) of the sub-surface circulation and the SSH of the control run displayed in Fig. 3.11, show the tropics, the retroflexion of the North Brazil Current and the Gulf Stream system to present more variability.

So, in principle, we could expect those regions to be more sensitive to our imposed perturbation.

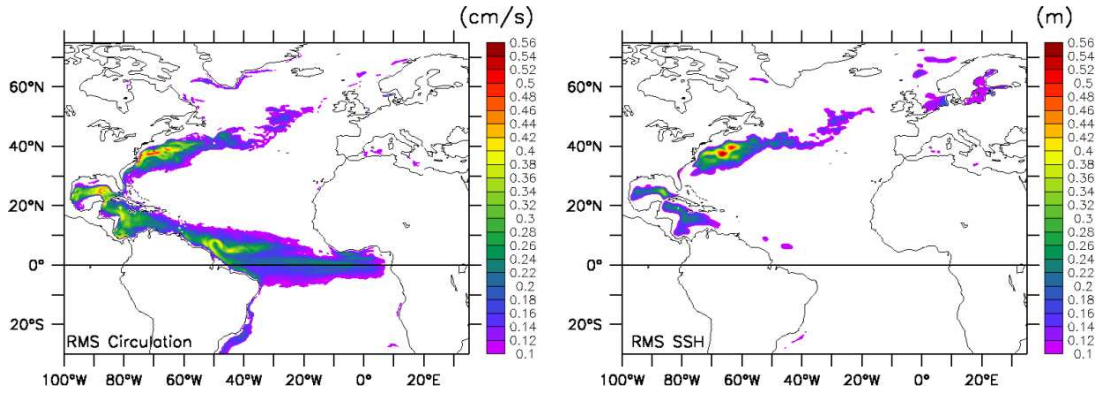

(a) rms of the surface velocity. (b) rms of the sea surface height.

Figure 3.11: Distribution of the rms of (a) the velocity averaged in the top 100 m depth (see Fig. 3.8a) and (b) of the sea surface height. Both fields are derived from the control run results.

3.4 Perturbed response

In this section we investigate the changes of the ocean circulation in response to the imposed dust-related perturbation in the subtropical eastern North Atlantic. The analysis is based on the changes in simulated sea surface temperatures and sea surface heights. We start by discussing their response on the large (basin) scale (Sec. 3.4.1), and then on the sub-basin and local (i.e., in the perturbed region) scales (Sec. 3.4.2).

3.4.1 Large-scale response

Sea Surface Temperature (SST)

The temperature of the first vertical level of the model represents the sea surface temperature (SST). Here, we investigate the SST differences between the perturbed (run3) and the control (run2) runs, which will be referred to as $\Delta(SST)$.

The distribution of the monthly averaged $\Delta(SST)$ for March, May, October and December in the first year of simulation (i.e., year 2000) are shown in Fig. 3.12. The first

order impact of the perturbation in the Q_{sw} fluxes on the eastern subtropical North Atlantic is to cool the ocean surface, here represented by negative values of $\Delta(SST)$. The perturbation in this experiment starts at the end of February 2000. At the very beginning (i.e., first week in March) the $\Delta(SST)$ is observed to be stronger along the coast and south of 30° N. The monthly mean $\Delta(SST)$ distribution in March 2000 (Fig. 3.12a) shows high values with a shape of a typical Saharan dust plume, with an offshore limit at 40° W and, in the northernmost part of the perturbation area, at 25° W. This last feature is most likely the response of the SST to the intense Saharan dust outbreak that took place during the last week in February 2000, which presented AOD values as large as 3.5 even at the latitude of the Gibraltar Strait (see Fig. 3.3). Furthermore, the non-uniform spatial distribution and the differences in magnitude observed in March 2000 are directly related to those of the AOD. We would like to remind that the forcing efficiency used to generate the shortwave flux anomalies was chosen to be constant (i.e.: $f_e = -40\ Wm^{-2}AOD^{-1}$), and therefore, in principle, the ocean surface response is expected to depend directly on the variations in AOD.

The dust-induced anomalies in SST are observed to start being advected at the end of March 2000. In the northeasternmost part of the perturbed area (note that, except in May, the original perturbed region is always denoted with the black circle in the plots) a displacement of $\Delta(SST)$ towards the Gibraltar Strait can be seen clearly starting in May 2000 (Fig. 3.12b). In addition, SST changes start to develop in the south and in the west, which are later observed to propagate towards the African coast and the northern coast of South America, respectively. This seems to follow the mean surface circulation pattern shown in Fig. 3.8 and Fig. 3.9b. The amplitudes of $\Delta(SST)$ become as large as 1° C by August 2000 (not shown). In October (Fig. 3.12c), $\Delta(SST)$ presents amplitudes of ± 1° C and eddy-like behavior in the equatorial region. A large elongated negative $\Delta(SST)$ ($\sim$ -0.8° C) is observed along the southwestern coast of Africa, into the Gulf of Guinea. By October, the signal can be seen along the whole northern coast of South America and has reached the Caribbean Sea. A weak surface signature in the SST is observed in the Gulf Stream region for the first time (i.e.: 7 months after the perturbation started). The previously mentioned advective zonal cold plume in the north has entered the Mediterranean Sea ($\sim$ -0.1° C). It is noted here that the advection of $\Delta(SST)$ to the north is limited by the Azores Current during the entire simulation. This is shown by the streamfunction drawn in Fig. 3.12b and the fact that the cooling at those latitudes is never large enough to produce subduction.

In December 2000 (Fig. 3.12d), $\Delta(SST)$ can be seen along the eastern coast of the United States up to 40° N and in the Gulf Stream region. The path taken by the $\Delta(SST)$ is to flow along the north coast of South America, then into the Caribbean Sea and Gulf of Mexico, and finally to arrive at the Florida Current and Gulf Stream after passing through the Florida Straits. An animation of the $\Delta(SST)$ shows, however, no connection on the surface between the signal in the Florida Straits and the Gulf Stream. This suggests a subduction of the anomalies in the Florida Straits and a further intensified vertical mixing with a consequent surface signal in the Gulf Stream system later on. This hypothesis will be discussed in Section 3.4.3. The elongated feature observed advecting towards the African coast in October, seems to have broken up into eddies and to have been advected further to the south.

A comparison of the average distribution of the $\Delta(SST)$ between years 2000 and 2001,

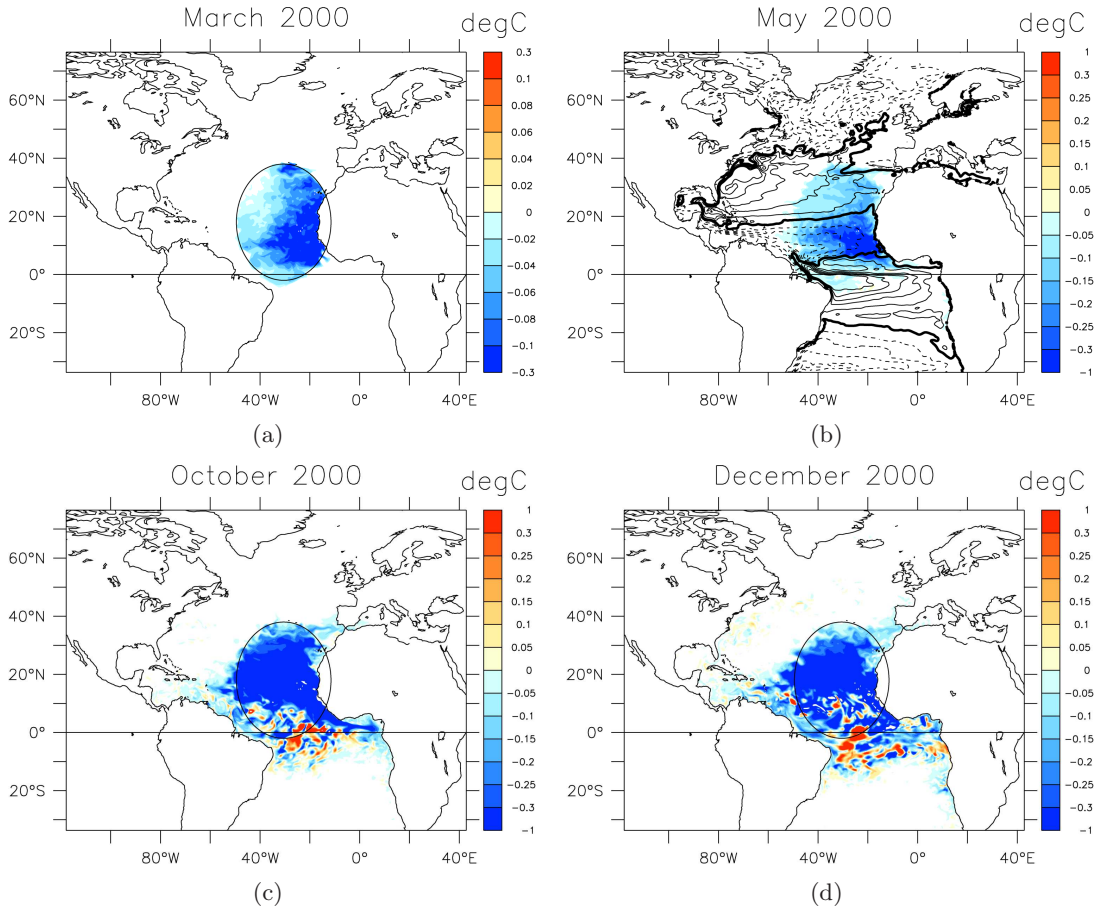

Figure 3.12: Distribution of $\Delta(SST)$ for (a) March, (b) May, (c) October, (d) December 2000. The black circle indicates the region that is being perturbed. The superimposed contours in (b) correspond to the streamfunction integrated between the surface and 150 m depth for that month. Values of $\Delta(SST)$ between $\pm$ 0.01° C are not drawn.

shown in Fig. 3.13, reveals an overall increase in the $\Delta(SST)$ magnitude in year 2001, and a general distribution that seems to follow the main path of the circulation. Furthermore, the evolution of the anomalies described for year 2000 is repeated every year triggered by the high dust season in summer and by dust outbreaks. However, a superposition to the previous years exists; therefore, year 2000 was chosen to describe the dynamics.

Sea Surface Height (SSH)

Changes in the sea surface height (SSH, η) can be attributed to changes of the total ocean mass or bottom pressure (p_b) and/or to changes of the ocean density at constant ocean mass (steric changes). Steric changes occur through heating or cooling of the ocean, and so it is what matters for the present analysis.

Because the MITgcm uses the Boussinesq approximation (see Chapter 2, Section 2.6), it will try to compensate the total mass gain (loss) from the cooling (warming) and

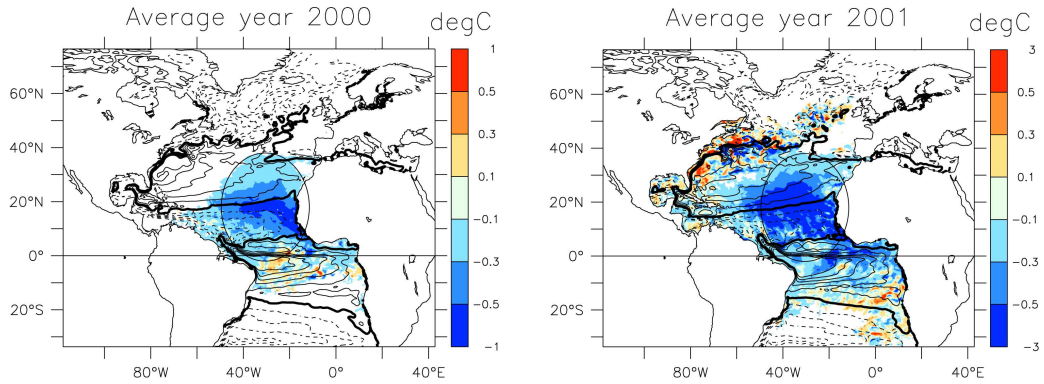

Figure 3.13: Distribution of $\Delta(SST)$, averaged for year 2000 (left) and year 2001 (right). The black circle indicates the region that is being perturbed. The contours correspond to the streamfunction integrated between the surface and 40 m. Values of $\Delta(SST)$ between $\pm$ 0.1° C are not drawn.

an adjustment and redistribution of mass in the basin will happen as a consequence (*Greatbatch*, 1994; *Ponte*, 1999). As an example, *Landerer et al.* (2007) found that p_b changes lead to a decreased length-of-day in a warming climate. The simulated η in this work does not distinguish between steric and ocean p_b changes, and so it needs to be corrected for p_b changes before any analysis of the perturbed η evolution can be done.

The time evolution of the bottom pressure (*Huang and Jin*, 2002) can be defined as follows:

$$\frac{\partial p_b}{\partial t} = \frac{\partial p_a}{\partial t} - \left(\frac{\partial}{\partial x} \int_{-H}^{\eta} \rho g u \, dz + \frac{\partial}{\partial y} \int_{-H}^{\eta} \rho g v \, dz \right) - (E - P) g \rho_w \tag{3.4}$$

where p_a is the atmospheric pressure at sea level, $(E - P)$ stands for evaporation minus precipitation, ρ_w is the fresh water density, g is the gravitational acceleration at the Earth's surface, and H is the total depth. The time evolution of p_b is thus controlled by:

- changes in p_a
- convergence of mass in the water column (2nd and 3rd terms on the right hand side of Eq. 3.4)
- local evaporation minus precipitation

For the Boussinesq ocean a source/sink term due to change in density is added:

$$\frac{\partial p_b}{\partial t} = \left(\frac{\partial p_b}{\partial t} \right)_{(\rho = \rho_0)} + g \int_{-H}^{\eta} \frac{\partial \rho}{\partial t} \, dz \tag{3.5}$$

Assuming that the global-integrated $(E - P)$ is zero, and given that p_a variations have no influence on the ocean dynamics (*Wunsch and Stammer*, 1997), the basin-averaged p_b becomes:

$$\overline{p_b} = \frac{g}{A} \overline{\int_V \frac{\partial \rho}{\partial t} \, dV} \tag{3.6}$$

so the basin-integrated bottom pressure anomaly is $\sim \partial\rho/\partial t$ meaning that it becomes positive (negative) when cooling (warming).

A global mean bottom pressure correction (*Greatbatch*, 1994) is applied to the sea surface height as follows:

$$\eta_{corrected} = \eta - \frac{1}{g\rho_0}\overline{\delta p_b} \tag{3.7}$$

where $\overline{\delta p_b} = \frac{1}{A}\iint_A \delta p_b \, dx \, dy$, and δp_b is the bottom pressure deviation from the initial value. The bottom dynamic height anomaly (phl) is defined as p_b/ρ_0. It has units of $m^2 s^{-2}$ and, as well as η, it is an output of the model. Because the differences in η between the control and the perturbed run are of interest here, $\Delta(SSH)(t_0)$ disappears and finally we get:

$$\Delta(SSH)(t) = \left(\eta(t) - \frac{\overline{phl(t)}}{g}\right)_{run3} - \left(\eta(t) - \frac{\overline{phl(t)}}{g}\right)_{run2} \tag{3.8}$$

Fig. 3.14 shows this time series in two different parts of the Atlantic basin (in blue) and the bottom pressure correction (in black). Clearly, the correction is needed in order to obtain a realistic response in the SSH. From here onwards, all the results shown regarding the sea surface height are bottom pressure corrected.

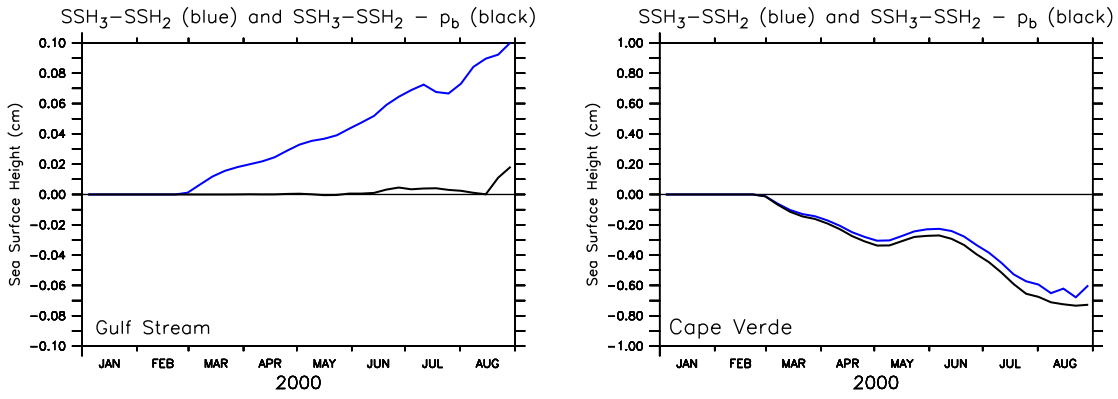

Figure 3.14: Time series of the differences between the perturbed and control runs for not corrected SSH (blue), and bottom pressure corrected SSH (black). Results are shown for a small region in the Gulf Stream (left) and around Cape Verde (right), for the first year of simulation. All the values are in cm.

The first order impact of the perturbation is to depress the ocean surface. Negative values of $\Delta(SSH)$ are observed in the perturbed area with a spatial distribution corresponding to the distribution of the AOD, in a similar way to what we saw for the $\Delta(SST)$ in Fig. 3.12. The distribution of $\Delta(SSH)$ averaged for year 2000 and 2001 is shown in Fig. 3.15. These results are similar to those of the SST in the sense that in the year 2001 the amplitude of the signal is larger, it reaches the western part of the basin and it further extends into the Gulf Stream and North Atlantic Current. In 2000, the $\Delta(SSH)$ shows a clear eddy-like activity in the tropics, especially in the northern

hemisphere, and in the North Brazil Current along the South American northern coast and following the path of the Caribbean Current. In addition, the dust-induced plume of negative $\Delta(SSH)$ (inside the circle) seems to have been advected towards the west. In year 2001, this advection is clear and positive eddy-like $\Delta(SSH)$ are found along the North African coast.

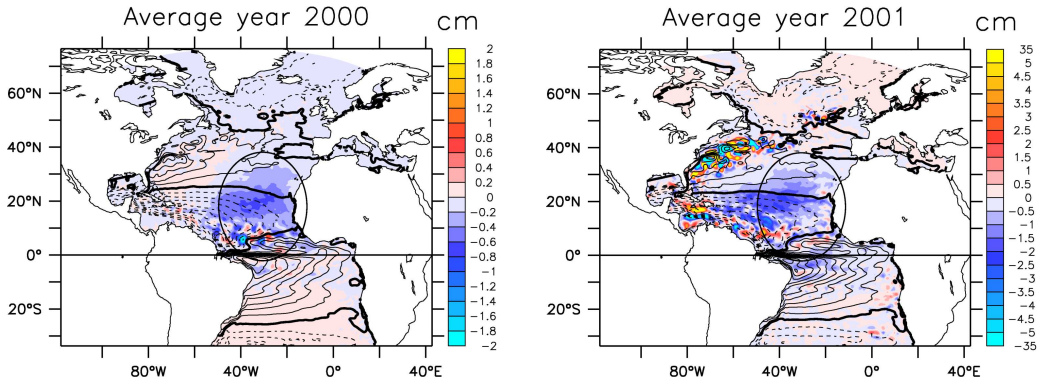

Figure 3.15: Distribution of bottom pressure corrected SSH difference between run3 and run2 ($\Delta(SSH)$), averaged for year 2000 (left) and year 2001 (right). The black circle indicates the region that is being perturbed. The contours correspond to the streamfunction integrated between the surface and 40 m depth, averaged over year 2000 (left) and 2001 (right).

Fig. 3.16 shows time series during the first 2 years of simulation for $\Delta(SSH)$ and for the Aerosol Radiative Forcing (ARF, i.e., the reduced Q_{sw}) averaged in areas representing the northern half (42° W - 20° W; 17.5° N - 30° N) and the southern half (42° W - 20° W; 5° N - 17.5° N) of the perturbation. A difference in the dynamics of the response can be seen already from this figure. Even though the ARF is stronger in the southern part, the SSH decreases in a much more homogeneous and stronger way in the north, at least during the shown period of time. In both panels a negative trend of the $\Delta(SSH)$ is observed in agreement with the constant dust-induced reduction of the Q_{sw} fluxes. The region in the south is more susceptible to mesoscale variability (i.e.: baroclinic instabilities). The spatial distributions of the $\Delta(SST)$ have already shown the SST to respond with more variability south of 15° N - 20° N (see for example Fig. 3.12d). The mechanisms associated with these differences will be analyzed next.

3.4.2 Sub-basin and local response

The animations of the dust-induced $\Delta(SST)$ and $\Delta(SSH)$ show the anomalies to leave the perturbed area in the southeast and to further flow westwards. Once they reach the coast of South America, a portion continues to be advected northwestward along the coast, and another portion retroflects towards the east, following the surface circulation displayed in Fig. 3.9. Fig. 3.17 shows the distribution of both variables in the area of the perturbation for the first half of January 2001. The superimposed streamfunction shows a cyclonic gyre south of 25° N which suggests that a return of the anomalies to

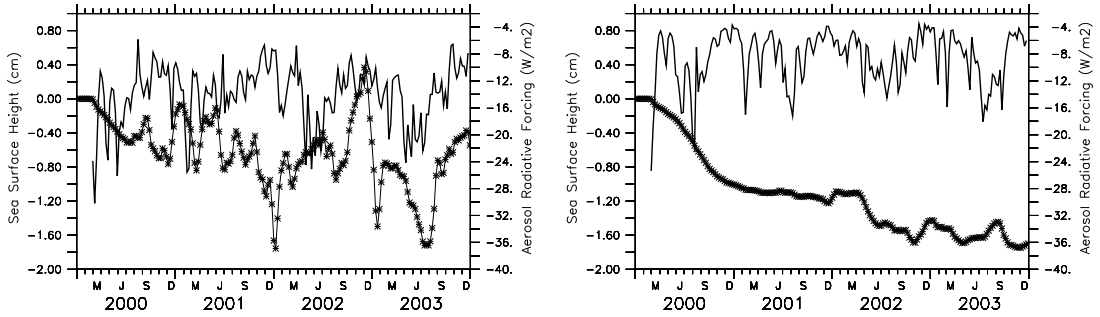

(a) SOUTH: 42° W - 20° W; 5° N - 17.5° N (b) NORTH: 42° W - 20° W; 17.5° N - 30° N

Figure 3.16: Time series of the $\Delta(SSH)$ (line with symbols) and of ARF (solid line), averaged on areas representing the (a) southern and (b) northern portions of the perturbed region.

the perturbed area could be possible as a result of the circulation. Fig. 3.17b shows anomalies of SSH along 10° N, suggesting that the signal is propagating zonally.

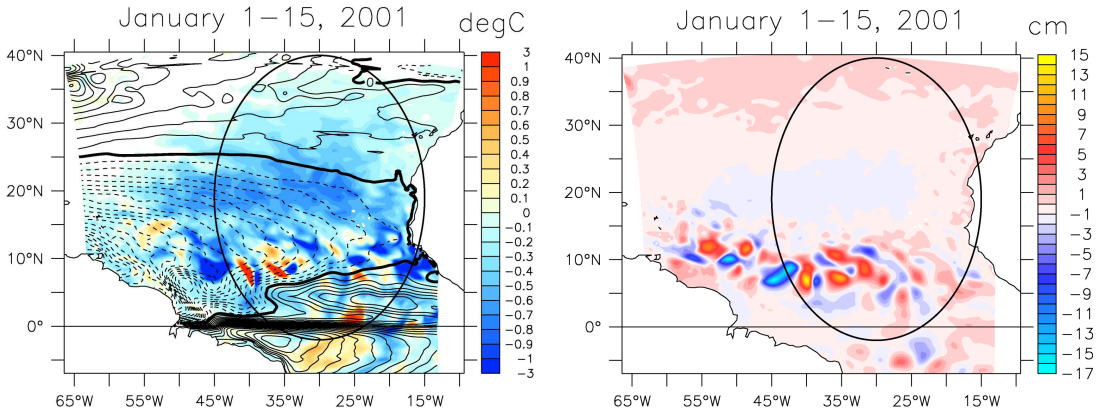

(a) (b)

Figure 3.17: Distribution of (a) $\Delta(SST)$ and (b) $\Delta(SSH)$, for the first half of January 2001. The black circles indicate the region where the perturbation is imposed. The contours correspond to the streamfunction integrated between the surface and 40 m averaged for the year 2000.

A large activity in $\Delta(SST)$ of $\sim \pm$ 3° C is observed south of 15° N (Fig. 3.17a) and values of about -0.7° C can be seen off the coast of Africa south of 20° N. To decrease the SST by 0.7° C in January (at about 20° N the mixed layer depth in January is of about 50 m), a radiative forcing of 240 Wm^{-2} over a week would be required, which, according to the perturbation here, is equivalent to an AOD of 6 which is not observed (Fig. 3.18a). Thus, in addition to a direct impact on the SST by dust-induced anomalies of the shortwave fluxes, a recirculation mechanism must exist for the $\Delta(SST)$.

Locally, the SST response to the dust-induced reduction in Q_{sw} fluxes decreases during

the first 2 years of perturbation (Fig. 3.18a). An uniform decrease is observed, however, only until September 2000 (i.e.: 7 months of perturbation) which seems to be interrupted by a relatively low dust period, until July 2001 when a high concentration of dust (AOD $\sim$ 1.4) is observed to be followed by a decrease in SST of about 2.5° C.

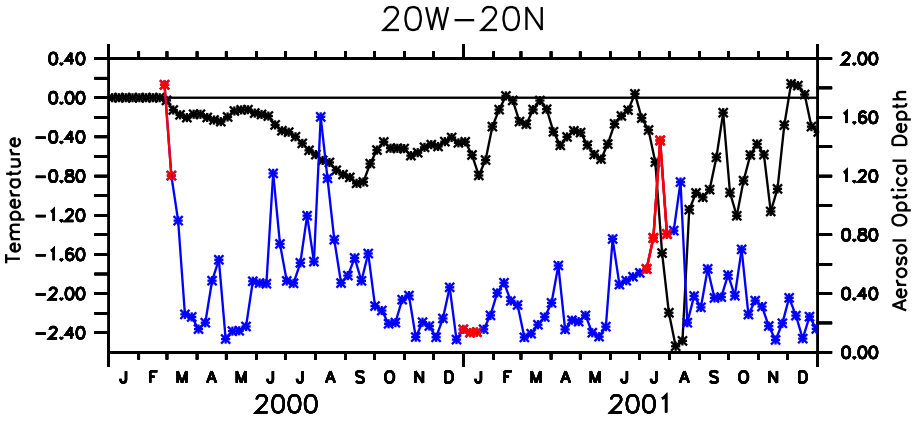

(a)

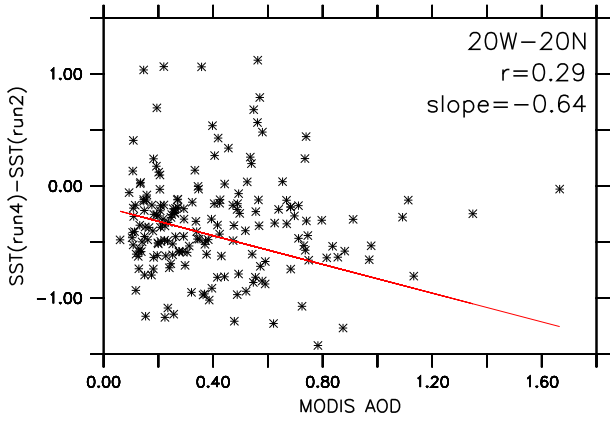

(b)

Figure 3.18: (a) Time series of $\Delta(SST)$ (black) and of weekly MODIS AOD (blue) at 20° W - 20° N for the first 2 years of simulation (2000-2001). The red segments are denoted to aid the discussion in the text. (b) Scatter plot of the MODIS AOD against $\Delta(SST)$ for the entire simulated period (2000-2003). The red line represents the least-squares linear regression.

During the period March - December 2000, $\Delta(SST)$ presents a variability that seems to be directly related to the concentration of dust in the atmosphere (i.e.: $\Delta(SST)$ decreases (increases) after an increase (decrease) in AOD). As discussed in the previous chapter, the dust effects on the SST can also be investigated with a bulk mixed layer model according to Eq. 2.4, which is written again here for convenience:

$$\frac{d(SST)}{dt} = \frac{ARF}{\rho_0 c_p MLD} \tag{3.9}$$

This relation allows us to quickly estimate the drops in SST due to a certain Q_{sw} forcing anomaly. The MLD in that location varies between 30 and 50 m in summer and winter, respectively, and the ARF can be calculated from the efficiency relation (i.e.: $ARF = f_e\ x\ AOD$). As an example, let us take the first dust event at the end of February 2000. According to Eq. 3.9, a forcing anomaly of -75 Wm^{-2} (AOD $\sim$1.9 and f_e=-40 $Wm^{-2}AOD^{-1}$), lasting over a week, would cool the 45 m thick upper ocean layer by about 0.25° C, which is in agreement with the corresponding SST drop revealed by the Fig. 3.18a. However, we saw before that the sole local effect of dust cannot induce the cooling observed in the first half of January 2001, so another effect must be superimposed.

Because the analysis here is based on the differences between the control and perturbed runs, the changes observed in the physical simulated variables of the ocean are due only to the anomalies in shortwave flux related to the dust variability in the atmosphere. A change in the local dynamics is to be expected after some time of persistent forcing in the eastern subtropical Q_{sw}. These changes could, in principle, lead to the propagation/advection of oceanic properties in such a way that the differences in SST and SSH can be reinforced. This is also clear from the scatter plot in Fig. 3.18b, in which, though significant correlated, the correlation coefficient is smaller than the one to be obtained if the variables were related only through Eq. 3.9.

We have identified two different behaviors in the eastern subtropical North Atlantic: north and south of 15° N, in response to changes in circulation due to dust-induced perturbations. The question remains, by which mechanisms the SST and SSH anomalies recirculate? And furthermore, what triggers these anomalies?

Zonal propagation/advection in the ocean can be observed in plots of longitude versus time at a given latitude, such as those displayed in Fig. 3.19. A clear difference in the dynamics can again be seen in those figures.

Propagating waves in this kind of diagrams appear as diagonal stripes. Traditionally, the wavelength, period and wave speed of the waves can be approximately determined by visual methods directly from the diagrams. The SST and SSH anomalies of alternating sign that were observed in the animation to advect towards (and also away from) the coast at the approximate latitude of 10° N, are now observed in Fig. 3.19a. The estimated eastward and westward velocities are 16 $cm\ s^{-1}$ and 11 $cm\ s^{-1}$, respectively. These characteristics agree with baroclinic instabilities at low latitudes in the North Atlantic (*Foltz and Carton*, 2004). Further north, Fig. 3.19b reveals several diagonal stripes with about the same slope, which could be a signal of westward propagating Rossby waves, and will be addressed later on. In addition, a northward advection/propagation of the signal along the African coast, which is apparent from Fig. 3.20 between 10° N and 22° N, was confirmed by the animation of $\Delta(SST)$.

So far, we have detected relatively fast $\Delta(SST)$ propagating zonally at about 10° N (Fig. 3.19a), a slower displacement at about 20° N starting at the African coast and continuing towards the west (Fig. 3.19b) and features propagating along the African coast between 10° N and 20° N (Fig. 3.20).

A number of studies have shown westward propagating anomalies in the eastern tropical and subtropical North Atlantic (*Chelton and Schlax*, 1996; *Polito and Cornillon*,

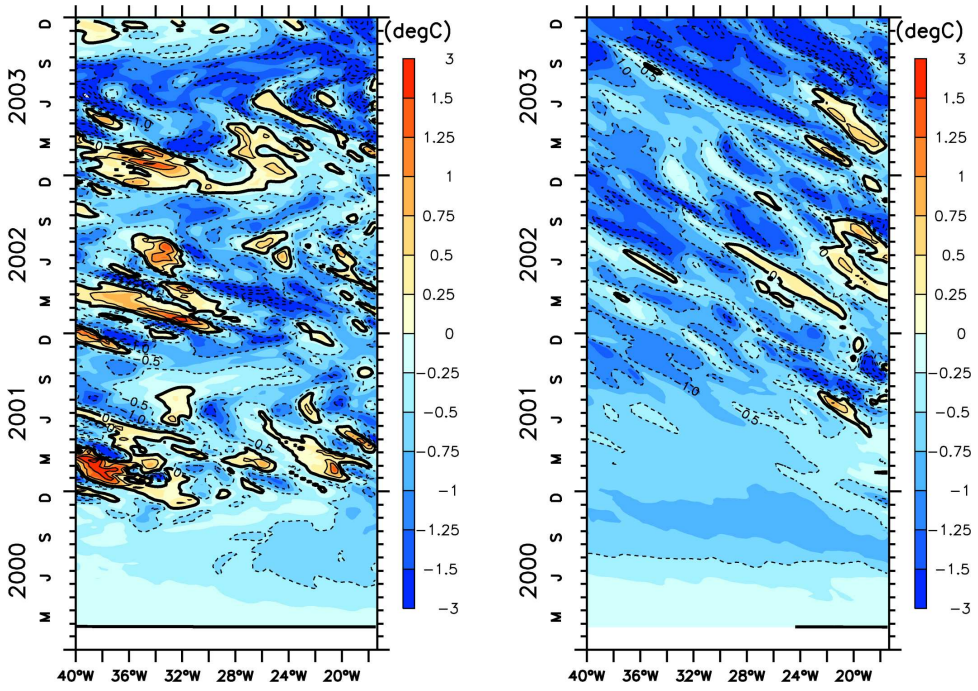

(a) $\Delta(SST)$, 10° N (b) $\Delta(SST)$, 20° N

Figure 3.19: Time-longitude diagrams of weekly $\Delta(SST)$ averaged between 9° N - 11° N (a), and between 18° N - 20° N (b). The plots span from the western African coast to 40° W and are shown for the entire simulated period (2000-2003).

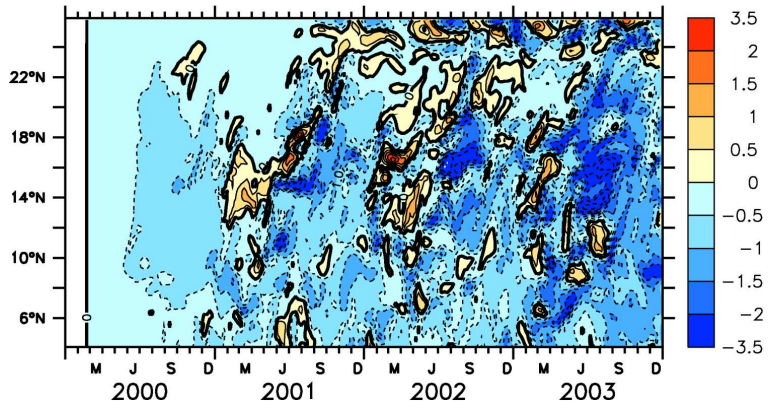

Figure 3.20: Time-latitude diagrams of weekly $\Delta(SST)$ along the African coast shown between 5° S and 35° N.

1997; *Cipollini et al.*, 1999; *Osychny and Cornillon*, 2004; *Chu et al.*, 2007). We tried to associate our model results to those findings, in particular, in relation to the phase speed, amplitude and triggering mechanisms for the first baroclinic mode of westward propagating Rossby waves.

Our goal here, is 1) to estimate the phase speed (C_p) of the simulated westward propagating anomalies in the eastern tropical North Atlantic (at 20° N, Fig. 3.19b and Fig. 3.21a), 2) to compare the results with theoretical characteristics of the first mode baroclinic Rossby waves (*Chelton et al.*, 1998) as well as to the results from observational studies, and 3) to identify the mechanism that triggers these waves.

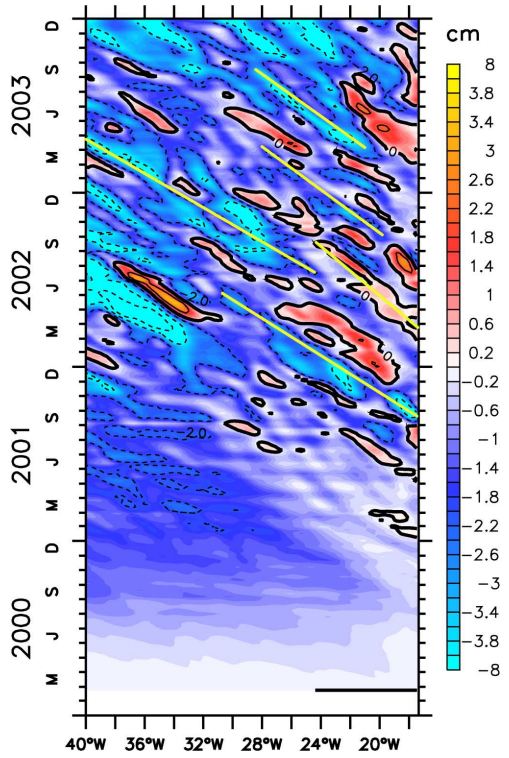

(a) Time-longitude at 20° N.

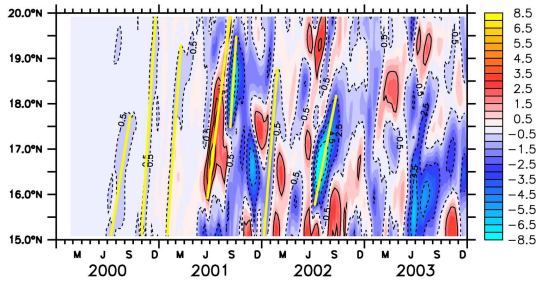

(b) Time-latitude along the African coast.

Figure 3.21: (a) Time-longitude diagram of weekly $\Delta(SSH)$ averaged between 18° N - 20° N shown from the western African coast to 40° W. (b) Time-latitude diagram of weekly $\Delta(SSH)$ along the coast shown from 15° N to 20° N. Both plots span the entire simulated period (2000-2003). The yellow straight lines denote propagating features.

We estimate the westward propagating speed of the dust-induced anomalies in SSH by fitting a straight line to the propagating features in Fig. 3.21a (some are denoted in yellow for clarity). The results are displayed in Table 3.2. The obtained average phase speed is -5.7 ± 0.5 $cm\ s^{-1}$, which is in good agreement with the results from the bibliography and the one expected from theory (see references in the Table). In this last regard, the ratio between the best-fit Rossby wave C_p and the one expected from theory estimated by *Osychny and Cornillon* (2004), varies from 1 to 1.5 beween 15° N and 25° N (their Fig. 7b), which would explain the close agreement between our estimation and the wave speed from the standard theory obtained here at 20° N.

Any physical mechanism that introduces a perturbation in the ocean potential vorticity field, such as variability of the wind stress curl, mean flow over topography (e.g.: changes when crossing the Mid-Atlantic Ridge), baroclinic instability or potential vor-

Table 3.2: Estimates of Rossby wave speed (C_p) in the eastern North Atlantic.

Reference	Region	Data	C_p ($cm\ s^{-1}$)
Gerdes and Wübber (1991)	African Coast 20° N	model	-3.0 to -4.0
Polito and Cornillon (1997)	African Coast 20° N	TOPEX/Poseidon	-5.9
Hill et al. (2000)	18°-20° N	ASST-GOSTA[a]	-5.5 to -7.0
Osychny and Cornillon (2004)	25° N	TOPEX/Poseidon	-4.0
Chu et al. (2007)	13° N	Argo floats	-11.0
Chelton et al. (1998)	20° N	theoretical	-6.0
this study	African Coast 20° N	model	-5.7 ± 0.5

[a]SST data derived from the ATSR (ASST) - Global Ocean Surface Temperature Atlas (GOSTA)

ticity advection, can generate a baroclinic Rossby wave. In this study, the observed anomalies are the result of the differences between the perturbed and the control runs, which are generated only by changes in the shortwave fluxes due to the presence of absorbing aerosols in the atmosphere. Thus, the experiment disregards changes in wind or topography as possible forcing mechanisms for the Rossby waves. So in principle, the simulated Rossby waves could be triggered by either tropical baroclinic instabilities observed south of 15° N, or coastal Kelvin waves which are known to travel northward along the African coast (*Lazar et al.*, 2006).

We found several Kelvin waves propagating eastward along the equator (not shown). Most of these propagating SSH anomalies had a period between 45 and 60 days and a speed between 1.5 and 2.1 $m\ s^{-1}$, which agrees with the characteristics of a first baroclinic mode Kelvin wave (*Katz*, 1997; *Illig et al.*, 2004; *Lazar et al.*, 2006). In particular, *Lazar et al.* (2006) found the equatorial Kelvin waves to develop in the western basin, to then propagate eastward and to split along the African coast. They then propagate polewards as coastal trapped Kelvin waves at about $1.8m\ s^{-1}$. In our work, we found no evidence of northward propagating features along the African coast starting in the equator. In Fig. 3.12 we identified an elongated anomaly of SST to "leak" from the perturbed area from the southeastern part and to advect southward along the coast. This could be a reason why we cannot see Kelvin waves propagating in the opposite direction of this strong (-1° C after 10 months of perturbation) anomaly.

Between 15° N and 20° N, however, we identified northward propagating SSH anomalies along the African coast (Fig. 3.21b and in the animation, not shown). Such anomalies are probably the forcing mechanism that triggers the westward Rossby waves at 20° N. The estimated phase velocity of these observed features is of about $30cm\ s^{-1}$ and becomes slower ($\sim 10cm\ s^{-1}$) after year 2001. These values are 3 times slower than those expected for trapped Kelvin waves in the subtropical eastern North Atlantic (*Lazar et al.*, 2006), and so these propagating features cannot be associated with Kelvin waves.

In this section, we have shown the response of the SST and SSH to an imposed perturbation in the shortwave fluxes on the eastern subtropical North Atlantic. Our findings can be summarized as follows:

- In a basin-scale, the perturbed SST and SSH are found to be redistributed according

to the main patterns of the surface circulation, and their magnitudes are largest in areas of highest variability in the ocean (see Fig. 3.11).

- The surface signal is observed to reach the Gulf Stream after 7 months since the start of the perturbation.

- Locally, the observed magnitude of $\Delta(SST)$ follows a bulk heat equation during the first 10 months of perturbation. Eddy-like $\Delta(SST)$ features are then observed to arrive at the coast from the west, consistent with baroclinic instabilities there. In fact, a simple heat equation as the one in Eq. 3.9 explains only 9% of the observed changes in SST (Fig. 3.18b).

- We have found a mechanism that relates: 1) eastward propagating features generated on the western side of the basin as a result of the modified circulation, which are consistent with baroclinic instabilities at low latitudes, with 2) eddies that advect anomalies along the coast from that latitude until approximately 20° N at a velocity of about 30 $cm\ s^{-1}$, triggering 3) westward propagating waves that are consistent with phase velocities of Rossby waves.

- The eastward propagating anomalies observed at 10° N are also the mechanism by which the anomalies return to the perturbed region.

3.4.3 Vertical structure of temperature anomalies

One way to analyse the evolution of the dust-induced simulated temperature anomalies, termed ΔTs, is through longitude-depth sections. Fig. 3.22 and 3.23 display two examples of east-west sections averaged between 18° N and 19° N (henceforth called the 18° N section) and at 27° N, for different dates. A section at 10° N will be analyzed later on. In every case, ΔTs are observed to start in March 2000 on the east and to further propagate towards the west. The $\Delta(SST)$ are observed to propagate westward following the tropical circulation paths. Therefore in principle, it seems more plausible to see temperature anomalies on the west, first in the 18° N section and later in the 27° N section.

At 18° N (Fig. 3.22a), the initial negative ΔTs observed in the easternmost part of the basin reaches a maximum value of -0.2° C and a vertical extension of 30 m at the coast and to 50 m offshore. The anomaly is then advected towards the west reaching a maximum zonal extension at 55° W and a depth of 100 m in December 2000 (Fig. 3.22b). At this stage, the anomalies take values of about 1° C. The ΔTs are observed at 27° N to reach a smaller zonal extent (∼45° W) and to be generally weaker. This characteristic can be explained with the differences in magnitude in the radiative forcing between these sections at the beginning of the perturbation, which were about 80 Wm^{-2} at 18° N and only about 20 Wm^{-2} at 27° N (see also Fig. 3.16).

In every case, positive ΔTs are generated beneath the vertically homogeneous negative ΔTs, which is an indication of the maximum deepening of the temperature anomalies generated at the surface. This depth is closely related to the vertical stratification of the water column. We saw in Fig. 3.7 that the surface density was higher at 27° N than at 18° N. In addition, the vertical profile of σ_θ is more homogeneous at 27° N (not

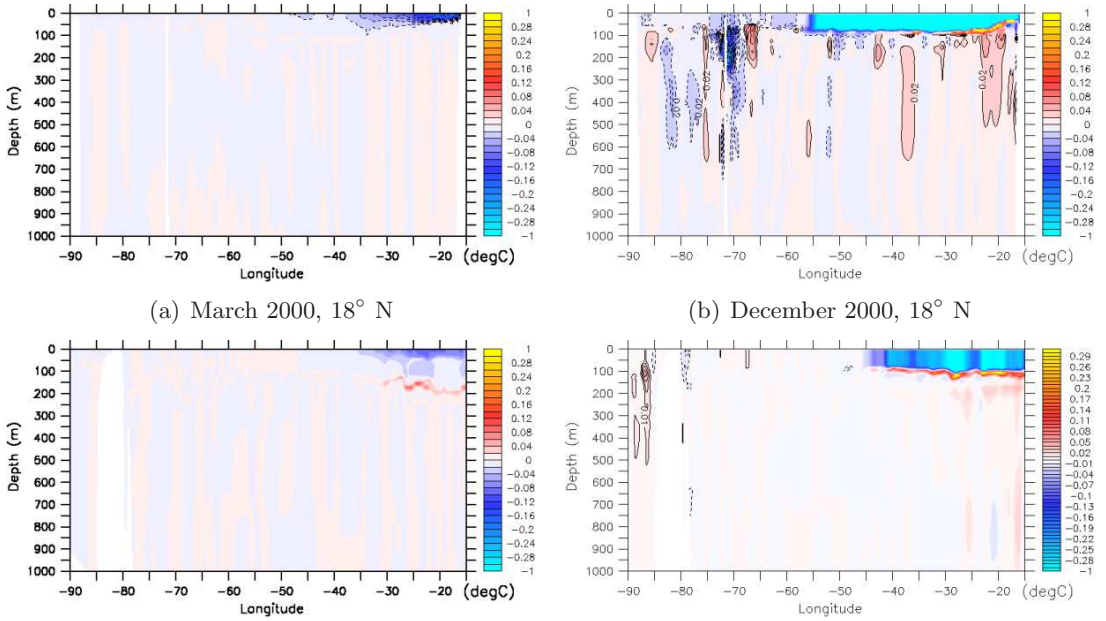

(a) March 2000, 18° N

(b) December 2000, 18° N

(c) March 2000, 27° N

(d) January 2001, 27° N

Figure 3.22: Vertical sections of ΔTs, at 18° N (a,b) and at 27° N (c,d). The dates are indicated at the bottom of each plot.

shown) and the mixed layer depth is twice as deep there. This could in turn facilitate the cold dust-induced ΔTs to reach relatively deeper waters and would explain why we see positive anomalies of temperature between 150 and 200 m (Fig. 3.22c). These anomalies are in fact, observed in the vertical profiles of temperature and salinity at 150 m in that region, and at 60 m at 18° N (not shown).

In the 18° N section, the ΔTs are observed in the western part of the basin for the first time in September 2000, which suggests a time scale of 6 months for the perturbation to reach the Caribbean Sea. In December (Fig. 3.22b), temperature anomalies of ± 0.02° C are observed inside the Caribbean Sea (between 85° W and 75° W) from 100 to 700 m depth. In the following months, the ΔTs there are observed to extend homogeneously in the vertical and alternate their sign in time and location. This could explain why we saw the signature of the SST to start a month later (i.e., in October 2000, Fig. 3.12c).

In the 27° N section, a weak signal of ΔTs is observed east of 85° W, (i.e.: outside the Florida Straits where the Florida Current begins) 3 months later than at 18° N (Fig. 3.12d). This seems to be the time that it takes for the signal to reach the Florida Current from the Caribbean Sea, following a path through the Gulf of Mexico and Florida Straits.

In December 2000 (Fig. 3.22b), positive anomalies of about 0.02° C can be seen on the eastern side at 18° N extending from 100 m to 650 m deep, which is a sign of changes in the vertical stratification as a response to the imposed cooling on the eastern side.

Fig. 3.23 displays longitude-depth sections for year 2001. Note that some of the just mentioned anomalies have vanished as a consequence of the change in color scale of

the plots. The separation of the perturbation from the coast, already observed in the distribution of SSH anomalies, is manifested in the vertical temperature at 18° N at the beginning of 2001 (Fig. 3.23a). As a consequence, positive ΔTs subduct from the coast under the negative ΔTs and travel westward. By October 2001 (Fig. 3.23b), these anomalies are one order of magnitude larger, are found all over until 60° W, and have developed a vertical extension of up to 700 m. Previously, we found anomalies in the SST and in the SSH near this latitude to propagate westward from the African coast which shared their characteristics with those of Rossby waves. We seemed to have found now, anomalies in the temperature that are propagating towards the west between 100/150 m and 700 m. Fig. 3.23b shows only a snapshot of these anomalies.

ΔTs in the western side continue to grow and alternate sign, noticeable in both sections. The blank observed at 27° N at all times between 80° W and 85° W, corresponds to the Florida peninsula, so the anomalies west of 85° W are, most likely, recirculating inside the Gulf of Mexico.

An interesting difference between the sections on the western side, is the vertical extension of the ΔTs. They extend from the surface up to 1000 m at 27° N but only from 100 to 700 m at 18° N. Because the same characteristic is observed in the salinity (not shown), such behaviour could be due to the fact that the isopycnals on the west are observed to be steeper at 27° N than at 18° N, thus enabling the ΔTs to deepen more there.

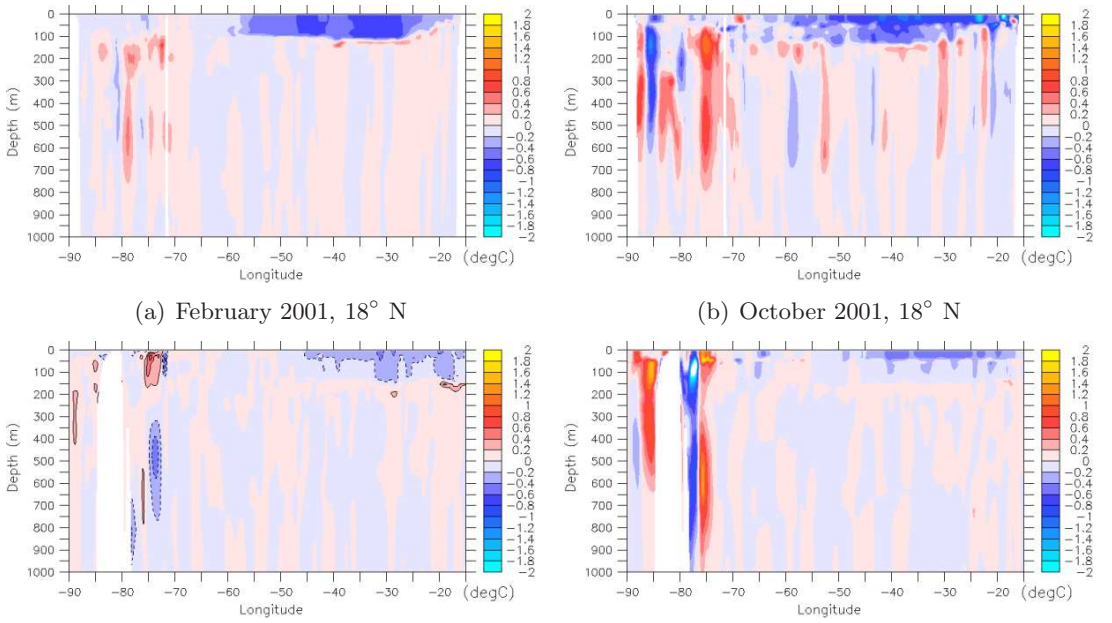

(a) February 2001, 18° N

(b) October 2001, 18° N

(c) June 2001, 27° N

(d) October 2001, 27° N

Figure 3.23: Vertical sections of ΔTs, at 18° N (a,b) and at 27° N (c,d). The dates are indicated at the bottom of each panel.

In summary, the imposed perturbation on the east has an impact on the local temperature in depth interval 30 to 50 m in the first 6 months, and further deepens up to

150 m afterward. The amplitude varies from -0.2° C at the beginning of the perturbation, to -3° C after 22 months of simulation. Positive significant anomalies beneath the negative anomalies, start at 18° N after a separation from the coast is observed, but immediately at 27° N. It has been discussed that these differences are most likely related to the background vertical distribution of σ_θ in winter in both areas.

The negative ΔTs at 27° N in the upper-layer show smaller amplitudes and less zonal extent than those at 18° N. The differences in magnitude are probably due to the differences in amplitude of the perturbation, and the zonal extent to the distribution of the streamlines integrated between 0 and 150 m (not shown). The ΔTs take 6 months to reach the west at 18° N and 9 months at 27° N, which is related to the advection path that the anomalies take. The amplitude of the ΔTs in the west are of 0.02° C at the beginning and grow with time to up to 7° C. The sign of the anomalies alternate in position and in time.

Fig. 3.24 shows the longitude-depth section at 10° N. It can immediately be seen from the figure that the evolution and distribution of the ΔTs are quite different from the ones further north just discussed. The anomalies in this case show a larger zonal extent at the beginning and, though shallower, they are of similar magnitude as those at 18° N (Fig. 3.24a). Already in May 2000, some activity can be seen at 55° W between 50 and 400 m (not shown). This increments in June 2000 displaying maxima ΔTs at 250 m. This agrees with the activity of eddies observed already in the $\Delta(SST)$ along the northern coast of South America (see Fig. 3.12). In December 2000, the signal has reached the west and becomes stronger with time. Fig. 3.24b shows the situation in June 2001. In opposition with the sections at 18° N and 27° N, the activity on the west is observed to be confined to a region off the coast of Central America. The ψ_{0-40} (Eq. 3.3) distribution shows a closed cyclonic gyre in this area suggesting that the anomalies are not likely to propagate northward, but to stay in the Caribbean Sea.

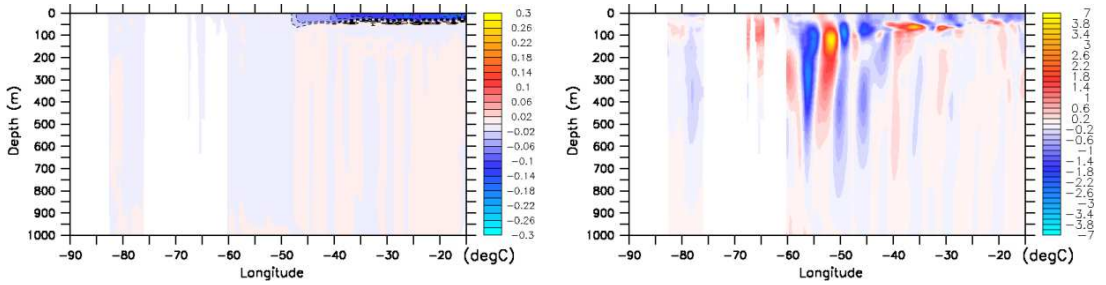

(a) March 2000, 10° N

(b) June 2001, 10° N

Figure 3.24: Vertical sections of ΔTs at 10° N for (a) March 2000, and (b) June 2001. Note the changes in color scale.

3.4.4 Meridional Overturning and Heat Transport in the Atlantic

- ***Atlantic Meridional Overturning Circulation***

The AMOC is the meridional volume transport as a function of latitude and depth integrated zonally in the Atlantic basin. It represents a streamfunction (ψ_{AMOC}), defined according to:

$$\psi_{AMOC}(y,z,t) = \int_{East}^{West} \int_{H}^{h(z)} v\, dz\, dx \tag{3.10}$$

$$where = \begin{cases} v & \text{is the meridional velocity field, } v=v(x,y,z,t) \\ \int_{East}^{West} dx & \text{represents the zonal integration of the velocity} \\ h(z) & \text{is the depth at which the transport there is the total } \psi_{AMOC} \text{ integrated between the bottom (H) and h(z)} \\ H & \text{is the total depth at each grid point} \end{cases}$$

In models, the overturning is derived from the actual velocity field. From *in-situ* observations, the overturning is defined as the sum of the northward flowing Gulf Stream derived from cable voltage measurements across the Florida Straits[2], Ekman transport derived from wind field data, and mid-ocean transport estimated from current meter, CTD and bottom pressure measurements (RAPID[3] *Cunningham et al.*, 2007; *Kanzow et al.*, 2007, and references therein).

Fig. 3.25 shows the AMOC estimated with the MITgcm for the control run, averaged over the period January 2000 - December 2003. Below the Ekman cells in the upper 500 m, there is a northward transport down until about 1000 m. The transport commonly associated with the North Atlantic Deep Water (NADW) flows southward between 1000 m and the σ_θ level represented by the zero transport contour in our plot (Fig. 3.25a).

The maximum simulated AMOC transport results in about 13 Sv at 39° N between 700 and 900 m depth, and presents a standard deviation (STD, not shown) of 3.5 Sv. The maximum AMOC obtained with measurements from the RAPID/MOCHA array is underestimated here. *Baehr et al.* (2009) found the observed time-mean of the AMOC to be also underestimated by the ECCO-GODAE[4], which are results from the MITgcm that were brought together to consistency with observations via data assimilation (*Wunsch*, 2007; *Köhl et al.*, 2007).

The largest STD (> 4 Sv) of our simulated ψ_{AMOC} is located in low latitudes in the northern hemisphere (Fig. 3.25b).

We obtain differences in ψ_{AMOC} between the perturbed and unperturbed runs ($\Delta\psi_{AMOC}$) of about -0.6 Sv for the first time in August 2000 at about 5° N and 1000 m. These differences grow in magnitude and spatial extent in the following 2 months when values of ψ_{AMOC} larger than ±1 Sv are observed between 10° S and 10° N. During the

[2]http://www.aoml.noaa.gov/phod/floridacurrent
[3]http://www.noc.soton.ac.uk/rapidmoc,
[4]ECCO-GODAE stands for the project "Estimating the Circulation and Climate of the Ocean - Global Ocean Data Assimilation Experiment"

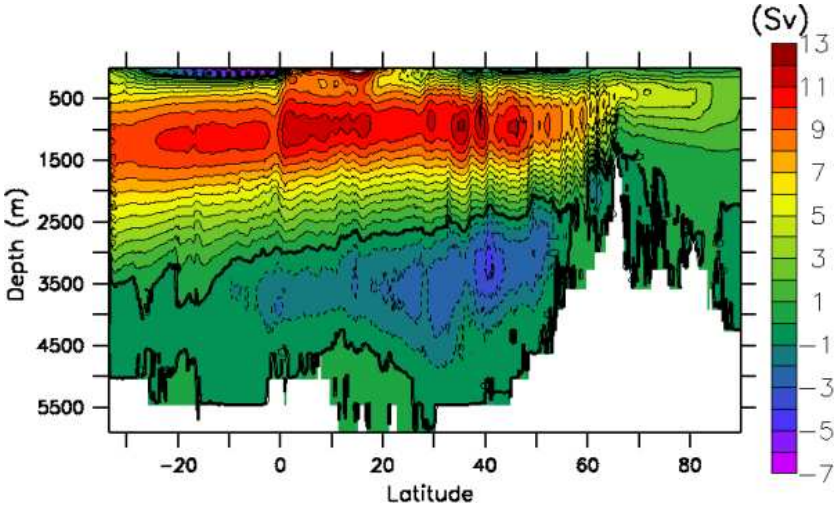

(a)

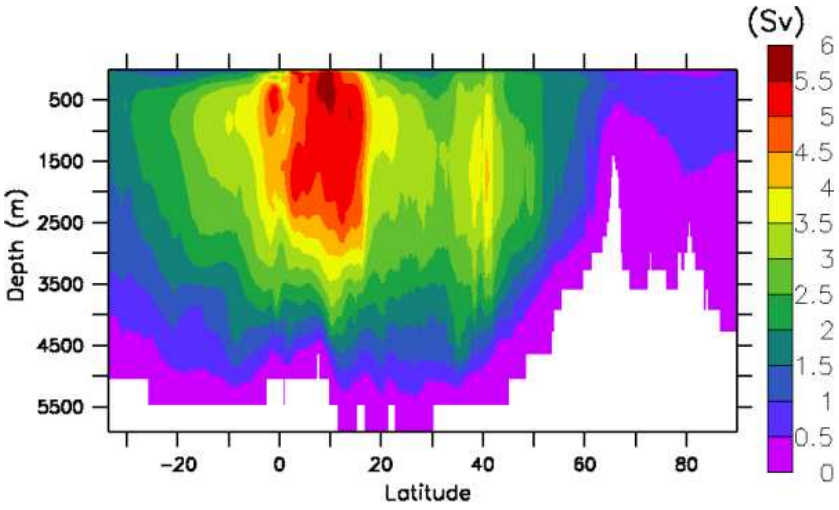

(b)

Figure 3.25: (a) Simulated 2000-2003 time-mean ψ_{AMOC} for the control run (in Sv), shown in the Atlantic north of 30° N. Positive values denote clockwise circulation; contour interval is 1 Sv and the thick black line indicates the zero contour. (b) Standard deviation of the simulated MOC.

remaining simulated period, this signal remains strong in that area. These changes are most likely associated with the instabilities and eddy-like activity that we observed in the tropics in the animation of the SST and SSH. Moreover, we saw in Fig. 3.24 that the differences in temperature extended in the vertical at 10° N. The imposed perturbation in the eastern subtropical North Atlantic, triggers changes in the circulation with which high eddy-activity in the tropics is associated. As a consequence, we obtained an increased interhemispheric exchange of mass and heat which is manifested in changes in the AMOC (see *Garzoli et al.*, 2003; *Lumpkin and Garzoli*, 2005). That area is also

where the highest STD were found (Fig. 3.25b), so the response of the AMOC changes there should be taken with care.

Fig. 3.26 shows time series of $\Delta\psi_{AMOC}$ at 1000 m and at different latitudes. We can see from the figure, that the changes in AMOC at 9° N (Fig. 3.26a in purple) start about 7 months earlier than in other latitudes and show the largest amplitudes. Changes in the AMOC centered around 37° N appear in January 2001, but reach values larger than 1 Sv by April of the same year. The further variability of changes in mass transport can be seen in the time series at 37° N in Fig. 3.26b represented in blue.

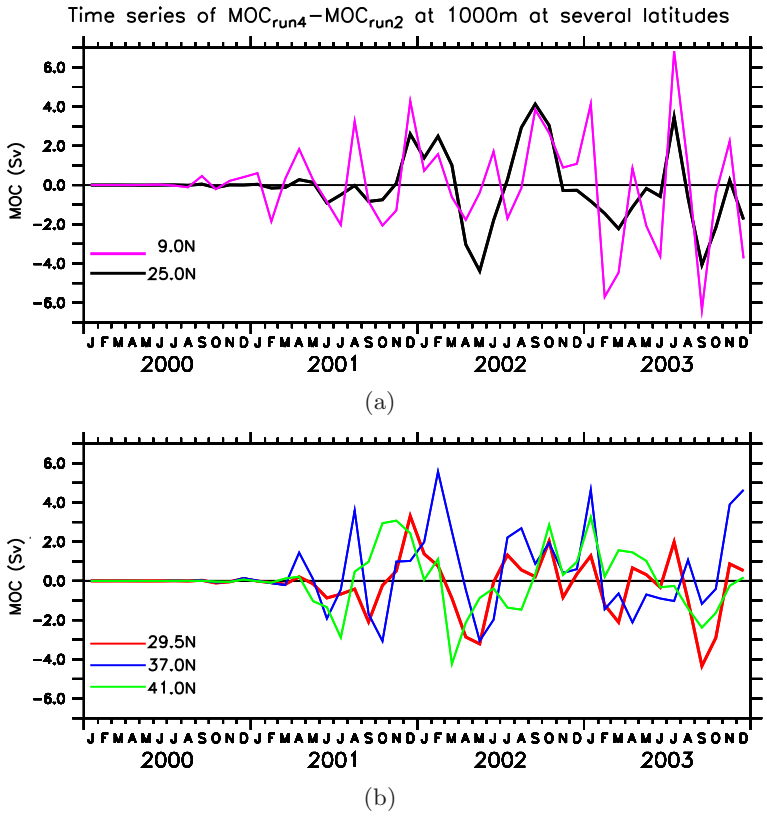

Figure 3.26: Time series of $\Delta\psi_{AMOC}$ at 1000 m for the period 2000-2003 at several latitudes: (a) 9° N (purple) and 25° N (black), and (b) 29.5° N (red), 37° N (blue) and 41.0° N (green).

The observed changes in Fig. 3.26 and in latitude-depth plots (not shown), show a change in the sign of $\Delta\psi_{AMOC}$ that varies between 2 and 6 months. Such oscillation of sign is most likely a result of the presence of eddies in the southern and western branches of the North Atlantic anticyclonic gyre and the Gulf Stream system that were discussed earlier in this chapter. Whether the east-west density gradient generated by the perturbation imposed in the eastern Atlantic is large enough to generate changes in the AMOC or not, is masked by the larger changes that arise from the presence of eddies. So the net impact of the perturbation on the AMOC results difficult to study from time-varying plots. For this reason, the 2000-2003 time-mean changes in the AMOC are

investigated from Fig. 3.27. Superposed to the distribution of the time-mean $\Delta\psi_{AMOC}$ are the contours of the differences of the STD between the runs. In the following, only results that are larger than the STD differences are discussed. The effects of the perturbation in the AMOC averaged over the 4 years of simulation are:

- to increase the AMOC as much as 0.55 Sv between 35° N and 39° N, and as much as 0.45 Sv at about 43° N;
- to decrease the AMOC in 0.2 Sv at 40° N (note that this change is significant from the surface down to 3500 m only);
- to decrease in about 0.2 Sv a cell centered in 45° N and between 200 and 1500 m.

The remaining regions that show positive (negative) differences are all lower (larger) than 0.15 (-0.15) Sv.

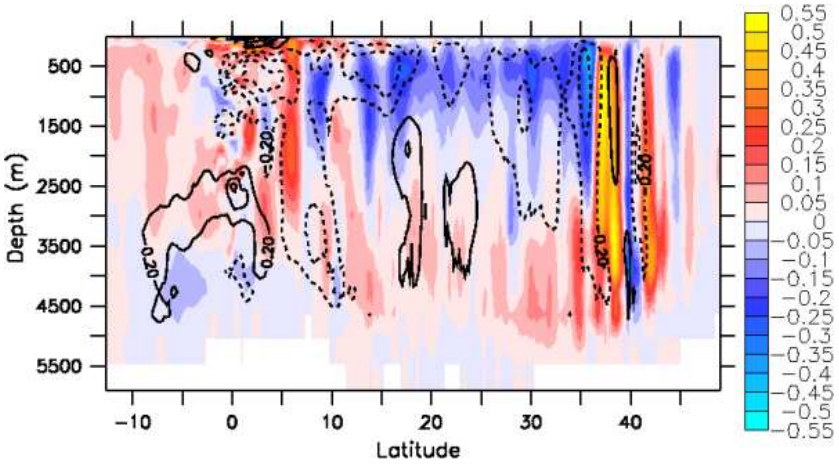

Figure 3.27: Distribution of the differences in the simulated 2000-2003 time-mean ψ_{AMOC} between the perturbed and the control runs, shown between approximately 10° S and 45° N. The black contours represent the differences in the STD of ψ_{AMOC} between the runs. They take values between ±0.8 Sv. The contour interval is 0.2 Sv.

- ***Meridional Heat Transport***

The total heat transport (HT_{total}) by the meridional flow in the oceans across any latitude may be defined as:

$$HT_{total}(y,t) = \int_{East}^{West} \int_{H}^{0} \rho_0 \,.\, c_p \,.\, v(x,y,z,t) \,.\, T(x,y,z,t)\, dz\, dx \qquad (3.11)$$

where v and T denote the meridional component of velocity and potential temperature field, respectively, ρ_0 is a reference density, and c_p is the specific heat.

Fig. 3.28 shows the simulated HT_{total} as a function of latitude for each year and the average over the entire simulated period. The location of the maximum northward heat transport varies from year to year. The model produces a time-mean maximum

northward HT_{total} of 0.72 PW (1 PW = 10^{15} W) across 29.5° N, which agrees with the location obtained by *Marotzke et al.* (1999). The latitude and magnitude of the maximum meridional HT_{total} presents a year to year variability. The largest difference is observed in year 2000 when a maximum value of meridional HT of 0.94 PW is obtained across 15° N.

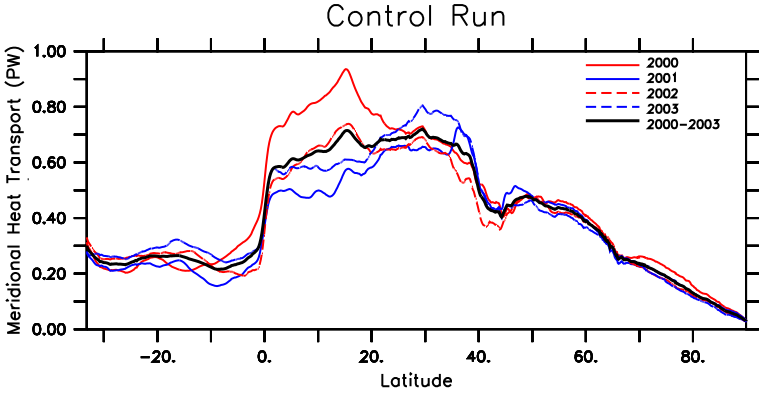

Figure 3.28: Simulated total meridional heat transport as a function of latitude estimated according to Eq. 3.11 averaged for each year, and for the entire simulated period for the control run. The units are peta Watts (PW=10^{15} W).

From Fig. 3.25 we can see that the heat in the Atlantic is being transported by water flowing northward at a certain temperature and returning southward at a lower temperature. So the HT_{total} (Eq. 3.11) may be separated into two components according to (*Hall and Bryden*, 1982; *Bryden and Imawaki*, 2001):

$$HT_{total} = \rho_0 c_p \int\int \bar{v}\bar{T}\, dz\, dx + \rho_0 c_p \int\int v'T'\, dz\, dx = HT_{over} + HT_{gyre} \qquad (3.12)$$

where $(\bar{v}, \bar{T})$ are the zonal means and (v', T') are the deviations from the zonal means. HT_{over} represents the overturning component due to the zonal mean circulation and HT_{gyre} is the horizonal circulation component. The averages over the 2000-2003 simulated period are shown in Fig. 3.29. We can see from the figure that in the North Atlantic, the HT_{over} is the most important component to the HT_{total}, until about 45° N where it decays to zero.

There are several estimates of the heat transport in the Atlantic near 25° N based on oceanographic measurements (see for example, *Hall and Bryden*, 1982; *Roemmich and Wunsch*, 1985; *Ganachaud and Wunsch*, 2000). In addition, we wish to compare our results with the intercomparison carried out by *Jia* (2003) regarding the meridional heat transport at 25° N and maxima ψ_{AMOC} with different coupled models. The results for the HT_{total}, HT_{over} and HT_{gyre} at 25° N are, respectively, 0.7, 0.6 and 0.1 PW. The model underestimates the HT_{total} of 1.1-1.3 PW obtained from oceanographic-based-measurements, as well as most of the model results published by *Jia* (2003) (see the author's Table 2). There are, however, some coupled models that also underestimate the ψ_{AMOC}.

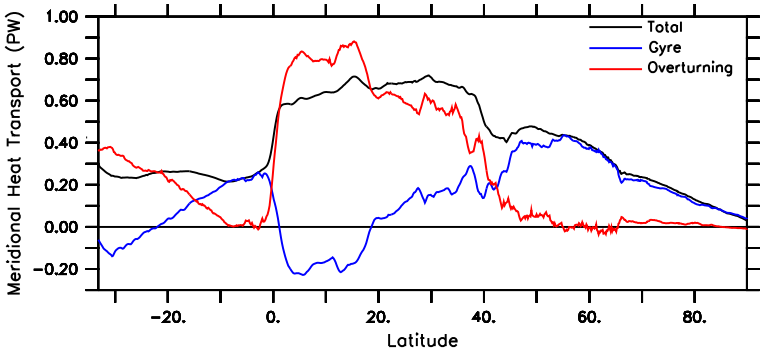

Figure 3.29: Meridional heat transport as a function of latitude: overturning (red), horizontal gyre (blue) components and total (black), averaged over the entire simulated period (2000-2003).

Latitude	Mean $\Delta(HT)$ (in TW)
9.0° N	+0.2
25.0° N	-7.6
29.5° N	-9.1
37.0° N	+18.6
41.0° N	-5.3

Table 3.3: $\Delta(HT)$ averaged over the 2000-2003 simulated period at various latitudes.

We are interested in evaluating the impact of the imposed perturbation on the heat transport in the Atlantic. Similarly to the analysis of the AMOC, we analyse the differences between the perturbed and unperturbed runs, termed $\Delta(HT)$. The time series of $\Delta(HT)$ at different latitudes (not shown) indicate, generally, a predominance of the overturning component. The HT_{gyre} becomes important north of 40° N as it is expected from Fig. 3.29.

The time variability of the changes in heat transport results similar to the one we saw for the AMOC, and thus we do not show them here. The sign of the $\Delta(HT)$ changes also from 2 to 6 months and starts at the beginning of year 2001. The largest changes in heat trasport are observed at 37° N, where, for example, for the period 2001-2002, the $\Delta(HT)$ varies from -200 TW to +300 TW. The results for the estimated 2000-2003 average of $\Delta(HT)$ at various latitudes are displayed in Table 3.3. In every case, the standard deviation exceeds the mean values shown in the table, which would suggest that the changes in heat transport obtained are more a result of the non-linear response of the ocean due to the perturbation, than to the buoyancy source that we impose.

Fig. 3.30 shows the time-mean components of the $\Delta(HT)$ as a function of latitude. The effect of the perturbation is to decrease the HT_{total} between 10° N and 35° N in about 10 TW, and to increase it everywhere else with maxima of 25 TW at 5° N and 37° N. The horizontal component (in blue) increased everywhere as a result of the changes in the circulation. The overturning component on the other hand, behaves in the same way

as the HT_{total}, reaching a maximum decrease of 35 TW at about 18° N. The noticeable variability that the components present in contrast to what we saw in Fig. 3.29, is the result of the fast-time varibility mentioned above.

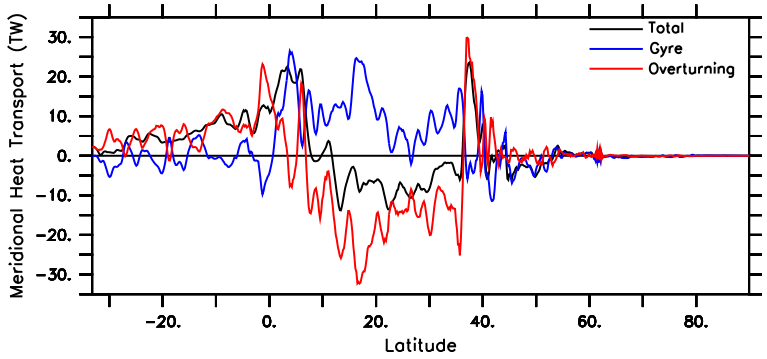

Figure 3.30: Horizontal Gyre (blue), Overturning (red) and Total (black) components of the meridional heat transport as a function of latitude.

We have found that even though the imposed perturbation in the eastern North Atlantic is always on the same direction (i.e.: negative buoyancy source), the response in the meridional overturning and heat transport in the Atlantic alternate sign and location quite rapidly. This suggests that the simulated changes that we are able to see from the time series, are the result of changes in the western side of the basin which arise from the perturbed anomalies that are being advected by eddies. The time that it takes to the $\Delta\psi_{AMOC}$ and $\Delta(HT)$ to show values different from zero, agrees with the time-scale that it takes the circulation to change in the west. Accordingly, we have found an increase of the horizontal component of the heat transport which was larger between the equator and 37° N. An estimation of the overall impact of the perturbation can be obtained by analyzing the distribution of the time-mean $\Delta\psi_{AMOC}$, in which the eddies' time-variability are averaged out. The results show an increase of the meridional transport of mass of as much as 0.55 Sv and 0.45 Sv centered at 38° N and 43° N, respectively, and a decrease of 0.2 Sv centered at 40° N and 45° N.

3.5 Discussion and Conclusions

Our main goal in this chapter was to study the changes of circulation in the North Atlantic forced by the Saharan dust loads in the atmosphere imposed in the subtropical eastern part of the basin. The most important findings are listed below:

- The ocean responds to the perturbation with a westward advection of the main perturbed region, and with mesoscale features, such as eddies. The dust-induced anomalies of SST and SSH evolve following the main paths of the ocean circulation. In particular, the equatorial circulation plays an important role in redistributing the anomalies, locally and triggering a large-scale response.

- The first order impact of the reduced shortwave flux due to Saharan dust is to depress and cool the ocean surface. During the first months the locally induced SST and SSH anomalies show clearly the shape of a typical Saharan dust plume. Such plume starts to be advected westward and eddy-like activity starts to develop in the tropics. This pattern repeats every year triggered by the high Saharan dust season in summer. The superposition of mesoscale activity, however, makes it difficult to see and therefore only the first 18 months of simulation are useful to study the ocean response evolution. In this sense, a clearer response was observed in the 1° x 1° resolution simulation (see Fig. 3.2).

- The anomalies in SSH and SST propagate towards the west and towards the south-easternmost part of the perturbation region along the African coast. There, they are trapped in a sub-surface anticyclonic loop shown by the $\psi_{sfc-150}$ distribution in Fig. 3.12b, and recirculate westward as part of the equatorial circulation. These anomalies take then 3 different paths:

  1. They retroflect towards the east along the equator, furthering enhancing the recirculation of anomalies along the African coast in the southern hemisphere.
  2. They continue to be advected along the northern South American coast further joining the Caribbean Current into the Caribbean Sea and Gulf of Mexico, eventually arriving to the Florida Current, Gulf Stream system and North Atlantic Current. The time-scale of the SST and SSH anomalies to reach the Gulf Stream system is of 7 months.
  3. They recirculate eastern shaped by a superficial cyclonic gyre (Fig. 3.8b) at a speed of 16 $cm\ s^{-1}$ which is compatible with baroclinic instabilities at low latitudes (*Foltz and Carton*, 2004), and so returning to the original perturbed area. As a result of this recirculation the SST cooling is amplified. Moreover, the changes in AOD explain only 9% of the variability in the simulated SST, which confirms the impact of the recirculation on the observed ocean surface cooling in the subtropical eastern North Atlantic.

- The baroclinic instabilities observed to propagate eastward along about 10° N, trigger northward advection of eddies which travel at a speed of about 30 $cm\ s^{-1}$ until 20° N, further initiating westward propagation at a mean phase speed of 5.7 $cm\ s^{-1}$ which is compatible with first mode baroclinic Rossby waves (see Table 3.2).

- Locally, the impact of the perturbation has quite different characteristics south and north of 15° N, mostly due to the meridional differences in Saharan dust concentration and ocean density background.

- The dust-induced anomalies generated locally on the east, recirculate as mentioned above and return to the original perturbed area near the African coast in 10 months.

- The local cooling is homogeneous in the vertical. It extends from 40 m to 100 m at 18° N and 150 m at 27° N, after 10 months. It further subducts towards the west reaching a maximum zonal extension of 55° W and 45° W at 18° N and 27° N, respectively. Positive anomalies of SST are observed below this homogeneous

cooling immediately at 27°N but only after 10 months at 18° N, when a separation of the perturbation from the coast occurs. The initial vertical extension of the cooling at 10° N is much smaller, but there is a quickly development of eddies that extends across the whole basin from 50-m up to 700-m depth.

- The time series of the differences between the perturbed and unperturbed simulated AMOC and total heat transport show an immediate change at 9° N, most likely due to the fast response of the tropics to the perturbation. The change north of 25° N appears after 7 months of perturbation. This time-scale agrees with the one found for the dust-induced anomalies to reach the Florida Straits.

- Our simulation produces a time-mean maximum total northward heat transport of 0.72 PW across 29.5° N. The largest HT component in the North Atlantic is the overturning until about 40° N, where it decays to zero and the horizontal component of the heat transport becomes larger. A comparison with published model results on the heat transport shows a good agreement with models that underestimate the maximum overturning. The meridional distribution of the heat transport presents interannual variability.

- The anomalies in AMOC and heat transport do not show a change in a constant direction with time, but they vary their sign between 2 and 6 months, as a result of the large eddy-activity. The overall impact of the perturbation is therefore analyzed from the time-mean differences:

    1. The AMOC increases in as much as 0.55 Sv and 0.45 Sv at 38° N and 43° N, respectively, and decreases in 0.2 Sv at 40° N and 45° N.
    2. The heat transport increases 18.6 TW across 37° N. This result should be taken with care, however, as the STD exceeds the mean.
    3. The HT decreases between 10° N and 35° N of about 7 TW, and it increases everywhere else. The overturning component behaves in the same way, but the decrease is larger, i.e., 15 TW, with a maximum of about 30 TW at 18° N. The horizontal component increases by about 8 TW, with a maximum of 25 TW around 18° N, balancing in part the decrase in the overturning component.

The large mesoscale activity that arises from the perturbation and the oscillations of alternate sign registered in the time series of the AMOC and HT, strongly suggests the non-linearities of the 1/6° simulation to be important. The time series of the resulting differences in HT obtained from the pilot 1° x 1° simulation with the analytic Gaussian imposed on the east (not shown), show the HT to increase or decrease in the same constant direction until the end of 1993 when eddy-like activity appears on the west. The amplitude of the Gaussian and the realistic perturbation are similar, and so such differences are probably mostly due to the spatial resolution differences. Note also the differences in magnitude of the changes in HT between both runs.

The (non-) linearity of the response to a perturbation on the east, was investigated by analyzing the differences between the anomalies in SSH ($\Delta(SSH)$) obtained with our perturbation, and the ones obtained with a perturbation of the same magnitude but with opposite sign. The results are shown in Fig. 3.31. We can see from Fig. 3.31a

that the initial response of the $\Delta(SSH)$ is linear (i.e.: responds with opposite sign to both perturbations). This response holds for about the first year (Fig. 3.31b), when we start seeing different varibility in the $\Delta(SSH)$. This is specially clear in the time series extracted on the western side of the basin, where only eddies are present.

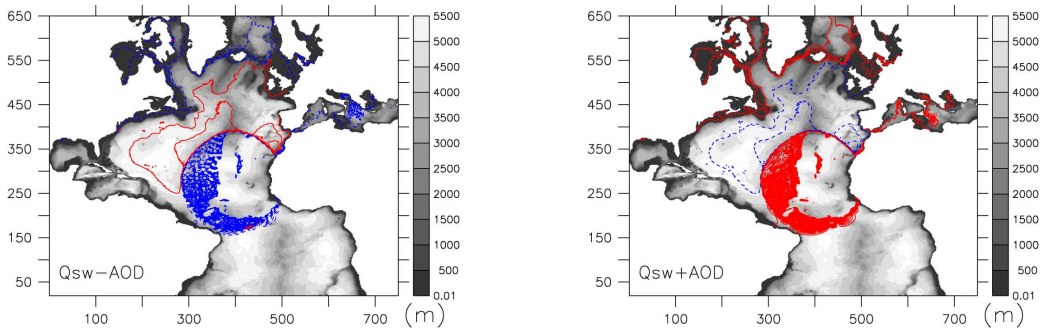

(a) $\Delta(SSH)$ distribution for negative (left) and positive (right) perturbation for the week centered on February 29, 2000. Positive contours are drawn in red and negative in blue. In the background is the bathymetry of the model.

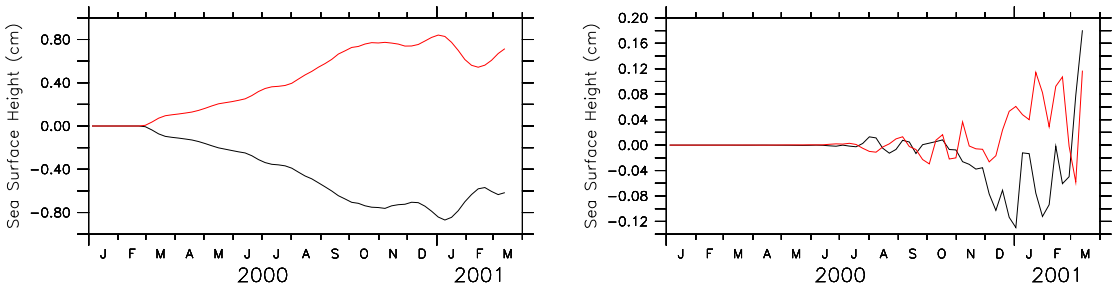

(b) Time series of $\Delta(SSH)$ for negative (black) and positive (red) perturbation, for a region on the east ($\sim$ 25° W - 27° N, left) and on the west ($\sim$ 80° W - 27° N, right).

Figure 3.31: Test for non-linearity in the SSH response.

The ocean is expected to show a non-linear response in regions of large variability, such as the Gulf Stream system (see Fig. 3.11), and furthermore, to respond with mesoscale features to a given perturbation. Our imposed perturbation on the east is realistic in the sense that it was constructed with realistic dust loads. However, we disregarded dust concentrations in the entire Atlantic, the effect of dust in other parameters than that of the shortwave fluxes, as well as the effect of clouds. The experiment presented here does not pretend to simulate realistic measurable dust-induced anomalies in the variables of the ocean. Our analysis should be taken as a theoretical study of the impact on the oceanic circulation of a buoyancy perturbation generated by realistic dust concentrations in the atmosphere on the eastern subtropical North Atlantic.

Chapter 4

Conclusions

The primary goal of this study was to investigate the impact of Saharan dust on the local sea surface temperature of the eastern subtropical North Atlantic, and on the ocean circulation on a sub-basin to basin scale.

- We have found significant support for a SST decrease associated with the cooling effect of Saharan dust due to reduced shortwave heating, through a comparison of SST observations with results from a numerical simulation not affected by dust-induced cooling (Chapter 2). These findings were supported by various independent simulations specifically designed to isolate the Saharan dust impact in the North Atlantic (Chapter 2 and 3).
- We have shown anomalies of SSH and SST that were generated in the eastern subtropical North Atlantic by imposing anomalies on the net shortwave flux, to be advected westward towards the western Atlantic following the main ocean circulation. These anomalies further returned via the equatorial circulation to the African coast where the effect was twofold: 1) to reinforce the amplitude of the local SST change, and 2) to trigger westward propagating Rossby waves. Changes in the time-mean Atlantic Meridional Overturning Circulation (AMOC) and Meridional Heat Transport (MHT) were also detected as a result of the buoyancy source imposed on the eastern North Atlantic basin (Chapter 3).

Next, we present a summary of the work carried out in this thesis and we provide answers to the questions formulated in the Introduction. We will finish the dissertation with an Outlook.

4.1 Summary

Changes in the solar radiative transfer into the ocean due to the presence of dust and aerosols in the atmosphere alter the forcing of the ocean circulation. We have seen in the Introduction that the dust in the atmosphere and its transport over (and input into) the oceans can impact the latter in several ways (see Fig. 1.1). The dust-induced changes in the ocean can interact among themselves for different time-scales and amplitudes and can, in turn, feed back onto the atmosphere. At the same time, dust-unrelated atmosphere and ocean dynamics, such as wind-stirring, upwelling, eddies, etc., are interplaying and affect the oceanic properties (e.g., the ocean surface temperature). Therefore, isolating the impact of dust in the ocean from other existing dynamical features is a challenge. In this study, we chose the effect of Saharan dust in the incoming shortwave fluxes at

the eastern subtropical North Atlantic as the forcing mechanism for changes in ocean properties and ocean circulation. The advantages and disadvantages of implementing other equally important dust-related factors will be discussed in the Outlook.

A combination of aerosol optical depth (AOD) and sea surface temperature (SST) retrievals from different sensors (MODIS, TMI, AVHRR, AMSR-E), *in-situ* data (AEROSE campaign), a one-dimensional mixed layer model of the ocean and a few versions of a three-dimensional general circulation model, were used to understand and isolate the signature of Saharan dust in the ocean. The questions addressed in the Introduction are answered next.

Observed SST and AOD anomalies

A combined analysis of weekly-averaged AOD anomalies from the MODIS sensor and weekly-averaged SST anomalies from the TMI sensor, was carried out to address the question whether Saharan dust and its associated cooling (postulated before by *Miller and Tegen*, 1999) can be detected from existing satellite SST datasets. The analyzed region was the eastern subtropical North Atlantic between Cape Verde and the Canary Islands, and the period was 2000-2006. In several instances we found decreasing tendencies of the SST (either as cooling or reduced warming) during, or right after (1-2 weeks time-lag), strong Saharan dust events lasting for several days. Furthermore:

- During the strongest dust events occurring in winter, a reduction of 0.2° to 0.4° C was observed in the SST.
- About 30% of the SST variance could be explained by the time-integrated AOD.

Remote Sensing Observations

To obtain further confidence in the quality of the SST from the TMI sensor, we performed a comparison between SST anomalies as inferred from the TMI and AMSR-E microwave radiometers, and from the AVHRR infrared radiometer, over the period 2002-2005. While the *rms* difference between both microwave datasets was only 0.17° C, it deviated substantially from the AVHRR SST data, resulting in a rms difference (TMI-AVHRR) of 0.78° C. Cold biases in the AVHRR dataset by as much as 2° C were obtained from the difference with TMI, as well as a clear seasonality that presented cold biases of as much as 1° C during summer months. A further comparison with the AOD data suggested that:

- The impact of dust clouds on the AVHRR sensor measurements in the subtropical eastern North Atlantic, was the primary agent for causing the AVHRR SST to be biased cold.

1D Ocean Mixed Layer Model Simulations

The remaining 70% of the variance that the analysis of AOD and SST observations was not able to explain, arise from other processes that lead to SST changes, most of them not related to dust. The advective processes in the ocean can be evaluated by the use of numerical models (dust not included) and further substracted from the observations, which are also containing the dust information. A first step, was to use a state-of-art

1D mixed layer model of the upper ocean based on the coupled KPP mixed layer model (*Large et al.*, 1994). We performed two simulations: a control run and a perturbed run, in two different locations (only Station 5 is shown in the thesis) and for two different years. The perturbed run incorporated the dust effects as a reduction of the NCEP/NCAR reanalysis shortwave flux with which the model was forced. This reduction, also termed aerosol radiative forcing (ARF), was calculated according to the efficiency relation of Eq. 2.1 (*Ramanathan et al.*, 2001). To this end, several radiation parameters measured in our studied area during the AEROSE-I campaign, were used to estimate the forcing efficiency (f_e). The perturbation was then constructed with time series of MODIS AOD, shortwave fluxes from NCEP/NCAR and the estimated f_e at 380 nm leading to -73.5 $\pm$ 7.1 $Wm^{-2}AOD^{-1}$. The impact of the Saharan dust on the local SST was then evaluated from the differences between the perturbed and the unperturbed model run.

- The simulation results support the magnitude of the dust-induced cooling that was observed in the TMI SST data, under the simultaneous conditions of strong dust events, low wind stirring and shallow ocean mixed layer.

Low wind conditions are unlikely to persist for more than a few days. Therefore, in principle, it would be difficult to observe the simulated cooling in the weekly SST data. In addition, one should be careful when comparing SST data from the TMI sensor, which represent the temperature of the skin layer of the ocean, with model output where the SST is represented by the first model vertical layer, which was 5 m in our study. Even though the simulated magnitude and phase of the dust-induced cooling of the ocean surface agreed with the observations, a definite proof of them being generated by dust, could not be given. For that reason, we have used a full 3D ocean circulation model.

Isolating dust-induced anomalies: 3D eddy-permitting OGCM simulations
The goal here was to discriminate dust-induced SST anomalies from dynamically-induced SST anomalies. For that purpose, we used an eddy-permitting ocean general circulation model (OGCM) simulation of the North Atlantic, which was run over the period 1948 through present, and analyzed the period 2000-2006. Results were given for the differences between SST observations (from the TMI sensor) and simulated SST (from the model).

- The largest differences in the rms SST variability ($> 0.55^\circ$ C) between the model and the observations, found close to the coast and seen to extend offshore at about 18° N, were attributed to the inability of the model at its horizonal resolution to simulate small-scale coastal processes like the upwelling filament off Cape Blanc.

Therefore, areas of high rms differences, low AOD and/or poor amount of AOD retrievals, were disregarded from the analysis.

- Significant correlations between the AOD anomalies and the observed minus simulated SST anomalies could be observed in an area between 27° W - 21° W and 19° N - 26° N, suggesting that about 10% of the SST differences there could be explained by the dust variability.

The correlations for the variables including their respective seasonal cycle remain of the same order. This suggested that 1) the AOD seasonal cycle in that region was not strong,

and 2) the model simulated well the SST seasonality there, so that the residual seasonal cycle was close to zero when performing the differences.

Response in Ocean Circulation

A modified version of the OGCM just discussed was used to evaluate the response of the ocean circulation to an imposed realistic dust-induced buoyancy perturbation in the eastern subtropical North Atlantic. The philosophy of this conceptual study was similar to the one applied with the 1D KPP model, in the sense that a perturbation was constructed using the AOD data, and that the differences between a perturbed and an unperturbed run were analyzed. The runs were performed over the 2000-2003 period, during which the f_e was chosen to be constant and equal to -40 $Wm^{-2}AOD^{-1}$ (see Section 3.2.2 for details).

The first order response of the ocean surface in the perturbed area was to cool and to depress. Such response was manifested by negative anomalies of SST and SSH, respectively, which evolved, locally and initially, in a pattern with the shape of a typical Saharan dust plume.

- On basin-scale, the anomalies of SSH and SST were redistributed and advected, mostly by existing eddies, following the main ocean circulation patterns.

The time evolution of the advection/propagation of SST and SSH differences showed the anomalies to leave the perturbed area in the southeast part where they were advected westward, by the north equatorial circulation. Once they reached the South American coast, they basically were split into: (a) a northwestward flowing branch along the coast that eventually reached the Gulf Stream; and (b) a second branch that advects eastward as a consequention of taking part of the Brazil retroflection. This eastward velocity was compatible to those for baroclinic instabilities at low latitudes in the North Atlantic. The estimated time-scales for (a) and (b) were 7 and 10 months, respectively.

- The experiment showed that a reinforcement of the SST anomalies can be expected in the subtropical eastern North Atlantic 10 months after the start of the perturbation.

This last result compares well with the one obtained during the previous mentioned observations minus model comparisons. In these sensitivity simulations however, we did not have the influence of possible model biases in the differences, since the comparison is made between two model (the same models) runs. Therefore, we were able to show that:

- Part of the local SST variability off the African coast that could not be explained by the local effects of AOD when comparing the model output with the SST observations, could arise from the recirculation and consequent reinforcement of the SST anomalies due to an indirect impact of Saharan dust. This mechanism is, however, not straightforward nor linear and thus not represented by results from correlation coefficients.

As a consequence of the signal advected in (b),

- Westward propagating anomalies of SST and SSH were triggered at about 20° N at the African coast. These anomalies propagated westward at a mean speed of 5.7

$\pm$ 0.5 $cm\ s^{-1}$ which agreed well with the theoretical wave speed of the first mode baroclinic Rossby waves, as well as with various estimates from observations (see Table 3.2).

The zonal evolution of the temperature anomalies in the vertical was different according to the meridional location.

- At 27° N and 18° N, negative anomalies deepened up to 150 m and were subducted westward until 45° W and 55° W, respectively. In both cases, positive temperature anomalies developed at the base of the mixed layer and further extended in the vertical. At 10° N, however, anomalies of alternating sign developed quite rapidly across the basin reaching depths of up to 700 m, as a consequence of the high baroclinic instabilities and eddies at low latitudes that were discussed before.

Sensitivity of AMOC and Meridional Heat Transport

We studied the response of the AMOC and the MHT to the imposed perturbation on the east, which acted as a buoyancy source.

- We have found that the east-west density gradient generated by the perturbation was not large enough to produce large changes in either the meridional transport of volume or heat.

Time series at different latitudes showed to alternate sign every 2 to 6 months, a characteristic of mesoscale variability. The impact of the dust-induced perturbation was evaluated through time-mean states.

- The average AMOC increased as much as 0.55 Sv and 0.45 Sv at 38° N and 43° N, respectively, and decreased by 0.2 Sv at 40° N and 45° N. These values represent between 1 and 4% of the mean simulated MOC amplitudes, and about 10% of the simulated MOC standard deviation.

- The total MHT decreased between 10° N and 35° N by about 7 TW, which resulted from the balance between a decrease by the overturning component of 15 TW, and an increase of the horizontal component by 8 TW.

In conclusion, the ocean response to the perturbation was mainly an advection of SSH and SST anomalies by mesoscale features which followed the main ocean circulation. As part of the redistribution of the signal, westward propagating Rossby waves were triggered, which, in principle, could transmit the effects of the perturbation at the African coast into the mid-latitude oceanic interior. MChanges in large-scale processes such as the AMOC and MHT have also been detected. We have found significant support for a SST decrease associated with the cooling effect of Saharan dust through a comparison of TMI SST observations with results from a numerical simulation not affected by dust-induced cooling. In addition, we have seen that part of the variance of the observed minus simulated SST that could not be explained by the AOD with linear correlation maps, could be explained by the presence of SST anomalies that recirculate and return to the African coast, being "indirect" impacts of Saharan dust. We conclude that models should incorporate the effect of Saharan dust. One possible way could be through corrections in

the shortwave forcing. The model used here presented biases due to the neglect of dust loading in the atmospheric forcing. In addition, models often relax their SST towards datasets that include AVHRR SST products. We have found the AVHRR SST to be biased cold in the subtropical eastern North Atlantic due to the presence of high dust loads in the atmosphere. The relaxation would thereby bring the simulation results closer to the observations, which were generally colder. This is, however, an artifact of the AVHRR biases and should be taken into account when including dust corrections in the forcing, specially in regions subject to high dust loads in the atmosphere.

4.2 Outlook

We would like to discuss here some important aspects that we think are necessary to take into account to improve the understanding of the Saharan dust effects on the ocean circulation.

The first one is regarding the enhanced turbidity of the upper ocean due to dust deposition at the ocean surface, either via enhanced productivity or due to the presence of dust particles in the water. By absorbing or blocking the incoming radiation in the top few meters of the ocean, the dust aerosols can again lead to subsurface temperature gradients and thus to modified currents. Enhanced biological productivity can be expected from dust fertilization, specially through nitrogen fixation (*Mills et al.*, 2004; *Moore et al.*, 2009). Its effects could be incorporated into model simulations by changing the vertical profile of light absorption in the water column as a function of the chlorophyll-a (Chl-*a*) concentrations at the surface (*Sweeney et al.*, 2005).

Using the available Sea-viewing Wide Field-of-view Sensor (SeaWiFS) sensor Chl-*a* retrievals, we attempted to identify impacts of Saharan mineral dust on the primary productivity of the ocean. In several cases, we found an increased Chl-*a* concentration during and shortly after high concentrations of dust in the atmosphere. The quality of Chl-*a* retrievals, however, decreases significantly underneath strong dust layers (*Moulin et al.*, 2001; *Claustre et al.*, 2002; *Davenport et al.*, 2002). As an example, *Gregg and Casey* (2004) obtained a 15.3% bias in SeaWiFS data in the subtropical eastern North Atlantic, very likely caused by absorbing aerosols from the Sahara desert. Even when the concentration of dust decreased in the atmosphere, we were not able to distinguish between real phytoplankton response and artifacts in the data due to residual dust in the atmosphere or water; at least, not by using weekly composites of AOD from the MODIS sensor and Chl-*a* from the SeaWiFS sensor (see *Volpe et al.*, 2009).

Changes in biological productivity can, in turn, feed back on the atmosphere through altered gas exchange. Hence, atmospheric impacts on the ocean represent Earth System linkages with potentially major implications for future atmospheric CO_2 levels, marine ecosystem behaviour and atmospheric chemistry.

What really matters in this context is the spectral dependence of the shortwave flux anomaly. Because solar radiation is absorbed in the top 100 m depending on the wavelength, it is important to know which frequency bands are most affected. In order to understand the impact of soil dust and for that matter, any type of aerosol present in the atmosphere, one needs to understand and measure the spectral characteristics of dust attenuation on the downward radiation.

In addition, we have seen that the magnitude of the estimation of the ARF depended directly on the estimation of the f_e. In this work, a f_e estimated from radiometric measurements was used in the 1D mixed layer model simulation, which was run for only 60 days. Because we did not have available a climatology of f_e, a constant accepted value was used to force the 3D OGCM when investigating the impact on the ocean circulation. It is clear that better estimations of f_e, as well as its dependency with time, are needed to better estimate the impact of Saharan dust in the ocean. A first step in this direction has already been taken.

In March 2008, four integrated UV-VIS hyperspectral radiometers were installed at the Cape Verde Atmospheric Observatory "Humberto Duarte Fonseca", as part of the SOPRAN and international SOLAS projects. The volcanic archipelago of Cape Verde is a group of 10 islands and 5 islets in the northeastern Atlantic Ocean, located about 600 km west of Senegal and near major north-south sea routes (Fig. 4.1). This region is data-poor but plays a key role in atmosphere-ocean interactions of climate-related and biogeochemical parameters including greenhouse gases. The location is also ideal for investigating impacts of dust on marine ecosystem. The sensors measure radiance for

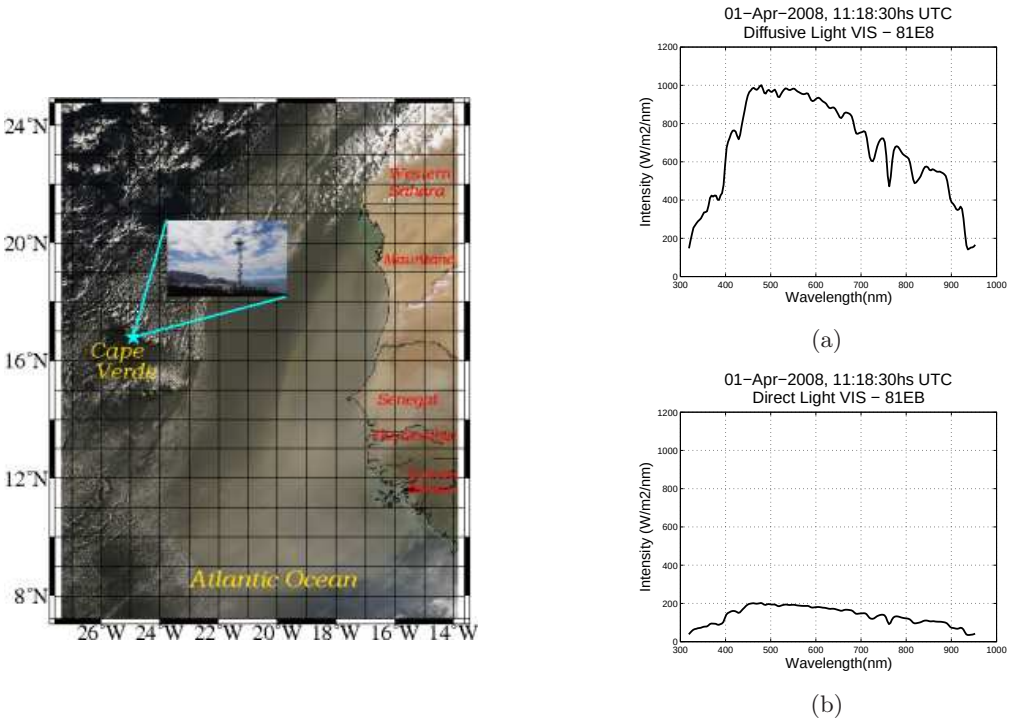

Figure 4.1: (left) MODIS Rapid Response System image from March 29, 2008, showing Cape Verde and part of the Western African coast. The blue star indicates the location of the Cape Verde Atmospheric Observatory "Humberto Duarte Fonseca" where the radiometers were installed. (right) Spectra measured by one of the irradiance sensors (a) and by one of the radiance sensors (b) for the spectral band 320-950 nm. These measurements were taken on April 1, 2008 at 11:18:30 UTC.

the UV-VIS spectral range and irradiance for the UV-VIS and UVA/UVB spectral range every 5 minutes from 06:00 UTC to 22:00 UTC, accounting for about 192 spectra per day (Fig. 4.1a-b).

In this thesis, we have shown how the ocean responds to the effect of Saharan dust in the shortwave fluxes. We believe that a next step should be to include the effects of enhanced Chl-a due to dust fertilization effects, and to better estimate the f_e. Specially, when new satellite datasets are becoming available through projects like the European project GlobColour (http://www.globcolour.org/) and *in-situ* measurements are carried out within through SOLAS and SOPRAN.

Acronyms

AEROSE trans-Atlantic Aerosol and Ocean Science Expeditions

AI Aerosol Index

AMOC Atlantic Meridional Overturning Circulation

AMSR-E Advanced Microwave Scanning Radiometer for EOS

AOD Aerosol Optical Depth

AVHRR Advanced Very High Resolution Radiometer

Chl-*a* Chlorophyll-*a*

ECCO Estimating the Circulation and Climate of the Ocean

EOS Earth Observing System

gcm/GMC General Circulation Model

INDOEX Indian Ocean Experiment

IR Infrared

KPP "*k profile*" parameterization

MIT Massachusetts Institute of Technology

MLD Mixed Layer Depth

MODIS Moderate Resolution Imaging Spectroradiometer

MW Micro Wave

NASA National Aeronautics and Space Administration

NCEP National Centers for Environmental Prediction

NCAR National Center for Atmosphere Research

NOAA National Oceanic and Atmospheric Administration

OGMC Ocean General Circulation Model

rms**/RMS** root-mean-square

SAL Saharan Air Layer

SeaWiFS Sea-viewing Wide Field-of-view Sensor

SSH Sea Surface Height

SOLAS Surface Ocean Lower Atmosphere Study

SOPRAN Surface Ocean Processes in the Anthropocene

SSS Sea Surface Salinity

SST Sea Surface Temperature

STD Standard Deviation

TOMS Total Ozone Mapping Spectrometer

TMI TRMM Microwave Imager

TRMM Tropical Rainfall Measuring Mission

UTC Coordinated Universal Time

List of Figures

List of Tables

Bibliography

Adcroft, A., C. Hill, and J. Marshall (1997), The representation of topography by shaved cells in a height coordinate model, *Month. Weath. Rev.*, *125(9)*, 2293–2315.

Adcroft, A., C. Hill, J.-M. Campin, J. Marshall, and P. Heimbach (2004b), Overview of the formulation and numerics of the MITgcm, in *Proceedings of the ECMWF seminar series on Numerical Methods, Recent developments in numerical methods for atmosphere and ocean modelling*, pp. 139–149, ECMWF. Available from: http://mitgcm.org/pdfs/ECMWF2004-Adcroft.pdf.

Astronomical Applications Department (1990), Astronomical almanac. U.S. Naval Observatory, Washington, DC, and Her Majesty's Nautical Almanac Office, *Royal Greenwich Observatory,529 pp.*

Baehr, J., S. Cunningham, H. Haak, P. Heimbach, T. Kanzow, and J. Marotzke (2009), Observed and simulated estimates of the meridional overturning circulation at 26.5°n in the Atlantic, *Ocean Sci.*, *5*(3), 575–589.

Blain, S., et al. (2007), Effect of natural iron fertilization on carbon sequestration in the Southern Ocean, *Nature*, *446*, 1070–1075, doi:10.1038/nature05700.

Boussinesq, J. (1903), *Théorie Analytique de la Chaleur*, vol. 2, 172 pp., Gauthier-Villars.

Boyd, P. W. (2007), Biogeochemistry: Iron findings, *Nature*, *446*, 989–991, doi:10.1038/446989a.

Boyer, T., S. Levitus, H. Garcia, R. A. Locarnini, C. Stephens, and J. Antonov (2005), Objective analyses of annual, seasonal, and monthly temperature and salinity for the World Ocean on a 0.25°grid, *Int. J. Climatol.*, *25(7)*, 931.

Bryan, F. O., B. Kauffman, W. Large, and P. Gent (1996), The NCAR CSM flux coupler, *Technical Note TN-425+STR,NCAR.*

Bryden, H. L., and S. Imawaki (2001), Ocean Heat Transport, in *Ocean Circulation & Climate: Observing and Modelling the Global Ocean*, vol. 77, edited by G. Siedler, J. Church, and J. Gould, pp. 455–474, International Geophysics Series.

Chelton, D. B., and M. G. Schlax (1996), Global observations of oceanic Rossby waves, *Science*, *272*, 234–238.

Chelton, D. B., and F. J. Wentz (2005), Global Microwave Satellite Observations of Sea Surface Temperature for Numerical Weather Prediction and Climate Research, *Bulletin of the American Meteorological Society*, *86*, 1097–1115.

Chelton, D. B., M. G. Schlax, K. El Naggar, and N. Siwertz (1998), Geographical variability of the first baroclinic Rossby radius of deformation, *J. Phys. Oceanogr.*, *28*, 433–460.

Chu, P. C., L. M. Ivanov, O. V. Melnichenko, and N. C. Wells (2007), On long baroclinic Rossby waves in the tropical North Atlantic observed from profiling floats, *J. Geophys. Res.*, *112*, C05,032, doi:10.1029/2006JC003698.

Cipollini, P., D. Cromwell, and G. D. Quartly (1999), Observations of Rossby wave propagation in the northeast Atlantic with TOPEX/Poseidon altimetry, *Adv. Space Res.*, *22*(11), 1553–1556.

Claustre, H., et al. (2002), Is desert dust making ologotrophic waters greener?, *Geophys. Res. Lett.*, *29(10)*, 1469, doi:10.1029/2001GL014056.

Coale, K. H. (2004), Southern Ocean iron enrichment experiment: Carbon cycling in high- and low-Si waters, *Science*, *304*, 408–414, doi:10.1126/science.1089778.

Colarco, P. R., et al. (2003), Saharan dust transport to the Caribbean during PRIDE: 2. Transport, vertical profiles, and deposition in simulations of in situ and remote sensing observations, *J. Geophys. Res.*, *108(D19)*, 8590, doi:10.1029/2002JD002659.

Condie, S. A. (1991), Separation and recirculation of the North Brazil Current, *Journal of Marine Research*, *49*(1), 1–19.

Conkright, M. E., R. A. Locarnini, H. Garcia, T. O. Brien, T. Boyer, C. Stephens, and J. Antonov (2002), World Ocean Atlas 2001: Objective Analyses, Data Statistics, and Figures, *CD-ROM Documentation. National Oceanographic Data Center, Silver Spring, MD,*, p. 17.

Corlett, G., et al. (2006), The accuracy of SST retrievals from AATSR: An initial assessment through geophysical validation against in situ radiometers, buoys and other SST data sets, *Advances in Space Research*, *Volume 37, Issue 4, Natural Hazards and Oceanographic Processes from Satellite Data*, 764–769, doi:10.1016/j.asr.2005.09.037.

Cunningham, S. A., et al. (2007), Temporal Variability of the Atlantic Meridional Overturning Circulation at 26.5°n, *Science*, *317*, 935–938, doi:doi:10.1126/science.1141304.

Davenport, R., S. Neuer, P. Helmke, J. Perez-Marrero, and O. Llinas (2002), Primary productivity in the northern Canary Islands region as inferred from SeaWiFS imagery, *Deep-Sea Res. II*, *49*, 3481–3496.

de Boyer Montégut, C., C. Madec, A. Fischer, A. Lazar, and D. Iudicone (2004), Mixed layer depth over the global ocean: An examination of profile data and a profile-based climatology, *J. Geophys. Res.*, *109*, C12,003, doi:10.1029/2004JC002378.

Dengg, J., A. Beckmann, and R. Gerdes (1996), The Gulf Stream Separation Problem, in *The Warmwatersphere of the North Atlantic Ocean*, edited by W. Krauss, pp. 253–290, Gebrüder Borntraeger, Berlin, Stuttgart.

Dunion, J. P., and C. S. Velden (2004), The impact of the Saharan air layer on Atlantic tropical cyclone activity, *Bull. Am. Meteorol. Soc.*, *85*, 353–365.

Erickson, D. J., III, J. L. Hernandez, P. Ginoux, W. W. Gregg, C. McClain, and J. Christian (2003), Atmospheric iron delivery and surface ocean biological activity in the Southern Ocean and Patagonian region, *Geophys. Res. Lett.*, *30(12)*, 1609, doi: 10.1029/2003GL01724.

Evan, A. T., A. K. Heidinger, R. Bennartz, V. Bennington, N. M. Mahowald, H. Corrada-Bravo, C. S. Velden, G. Myhre, and J. P. Kossin (2008), Ocean temperature forcing by aerosols across the Atlantic tropical cyclone development region, *Geochem. Geophys. Geosyst.*, *9*, Q05V04, doi:10.1029/2007GC001774.

Evan, A. T., D. J. Vimont, A. K. Heidinger, J. P. Kossin, and R. Bennartz (2009), The Role of Aerosols in the Evolution of Tropical North Atlantic Ocean Temperature Anomalies, *Science*, *324. no. 5928*, 778 – 781, doi:10.1126/science.1167404.

Foltz, G. R., and J. A. Carton (2004), Tropical instability vortices in the Atlantic Ocean, *J. Geophy. Res.*, *109*, C03,029, doi:10.1029/2003JC..1942.

Foltz, G. R., and M. J. McPhaden (2008), Impact of Saharan Dust on tropical North Atlantic SST, *J. Clim.*, *21*, 5048–5060.

Ganachaud, A., and C. Wunsch (2000), Improved estimates of global ocean circulation, heat transport and mixing from hydrographic data, *Nature*, *408*(453-456).

Garzoli, S. L., Q. Yao, and A. Ffield (2003), North brazil current rings and the variability in the latitude of retroflection., in *Interhemispheric Water Exchange in the Atlantic Ocean*, edited by G. J. Goni and P. Malanotte-Rizzoli, pp. 357–374, Elsevier, Amsterdam.

Gerdes, R., and C. Wübber (1991), Seasonal variability of the North Atlantic Ocean–a model intercomparison, *J. Phys. Oceanogr.*, *21*, 1300–1322.

Gill, A. E. (1982), *Atmosphere-Ocean Dynamics*, 662 pp., Academic Press.

Ginoux, P., M. Chin, I. Tegen, J. Prospero, B. Holben, O. Dubovik, and S.-J. Lin (2001), Sources and distributions of dust aerosols simulated with the GOCART model, *J. Geophys. Res.*, *106*(D17), 20,255–20,273.

Gouretski, V. V., and K. P. Koltermann (2004), WOCE Global Hydrographic Climatology, *Tech. rep.*, Berichte des Bundesamt fur Seeschifffart und Hydrographie, Hamburg und Rostock, Germany, 52 pp.

Greatbatch, R. J. (1994), A note on the representation of steric sea level in models that conserve volume rather than mass, *J. Geophys. Res.*, *99*, 12,767–12,771.

Gregg, W. W., and N. W. Casey (2004), Global and regional evaluation of the SeaWiFS chlorophyll data set, *Remote Sensing Environment*, *93*, 463–479.

Hall, M. M., and H. L. Bryden (1982), Direct estimates and mechanisms of ocean heat-transport, *Deep-Sea Res.*, *29*, 339–359.

Hanafin, J., and P. J. Minnett (2001), Cloud forcing of surface radiation in the North Water Polynya, *Atmosphere-Ocean*, *39*, 239–255.

Hawkins, M., V. Morris, N. Nalli, and E. Joseph (2007), Comparison of AEROSE-I and AEROSE-II surface level ozone measurements and ozonesonde profiles within Saharan dust and biomass burning plumes, *Extended Abstracts, Ninth Conference on Atmospheric Chemistry, 19th Conference on Climate Variability and Change, AMS Forum: Climate Change Manifested by Changes in Weather, San Antonio, TX, Amer. Meteor. Soc.*

Heimbach, P., C. Hill, and R. Giering (2002), Automatic Generation of Efficient Adjoint Code for Parallel Navier-Stokes Solver, in *Lecture Notes in Computer Science (LNCS)*, vol. 2330, part II, edited by J. Dongarra, P. Sloot, and C. T. (Eds), pp. 1019–1028, Springer-Verlag.

Hernández-Guerra, A., et al. (2002), Temporal variability of mass transport in the Canary Current, *Deep Sea Research II*, *49*, 3415–3426.

Hill, C., A. Adcroft, D. Jamous, and J. Marshall (1999), A strategy for terascale climate modeling, in *Proceedings of the 8th ECMWF Workshop on the Use of Parallel Processors in Meterorology*, pp. 406–425.

Hill, K. L., I. S. Robinson, and P. Cipollini (2000), Propagation characteristics of extra-tropical planetary waves observed in the ATSR global sea surface temperature record, *J. Geophys. Res.*, *105(C9)*, 21,927–21,945.

Hogg, N., and W. E. Johns (1995), Western boundary currents. U.S. National Report to Internatonal Union of Geodesy and Geophysics 1991-1994, *Supplement to Reviews of Geophysics*, *33*, 1311–1334.

Huang, R. X., and X. Jin (2002), Sea Surface Elevation and Bottom Pressure Anomalies due to Thermohaline Forcing. Part I: Isolated Perturbations, *J. Phys. Oceanogr.*, *32*, 2131–2150, doi:10.1175/1520-0485(2002)032<2131:SSEABP>2.0.CO;2.

Hunke, E., and W. H. Lipscomb (2002), CICE: the Los Alamos Sea Ice Model Documentation and Software User's Manual., *T-3 Fluid Dynamics Group, Los Alamos National Laboratory, Tech. Rep. LACC-98-16 v.3.*

Illig, S., B. Dewitte, N. Ayoub, Y. du Penhoat, G. Reverdin, P. De Mey, F. Bonjean, and G. S. E. Lagerloef (2004), Interannual long equatorial waves in the tropical Atlantic from a high-resolution ocean general circulation model experiment in 1981-2000, *J. Geophys. Res.*, *109*, C02,022, doi:10.1029/2003JC001771.

Jia, Y. (2003), Ocean heat transport and its relationship to ocean circulation in the CMIP coupled models, *Climate Dynamics*, *20*(2), 153–174, doi:10.1007/s00382-002-0261-9.

Jickells, T. D., et al. (2005), Global Iron Connections Between Desert Dust Ocean Biogeochemistry and Climate, *Science*, *308. no. 5718*, 67–71, doi:10.1126/science.1105959.

Kalnay, E., et al. (1996), The NCEP/NCAR 40 Year Reanalysis Project, *Bull. Amer. Meteor. Soc.*, *77*, 437–471.

Kalu, A. E. (1979), The African dust plume: Its characteristics and propagation across west Africa in winter, *SCOPE*, *14*, 95–118.

Kanzow, T., et al. (2007), Observed Flow Compensation Associated with the MOC at 26.5°n in the Atlantic, *Science*, *317*, 938–941, doi:10.1126/science.1141293.

Katz, E. J. (1997), Waves along the Equator in the Atlantic*, *J. Phys. Oceanogr.*, *27*, 2536–2544, doi:10.1175/1520-0485(1997)027<2536:WATEIT>2.0.CO;2.

Kaufman, Y. J., I. Koren, L. A. Remer, D.Tanré, P. Ginoux, and S. Fan (2005), Dust transport and deposition observed from the Terra-Moderate Resolution imaging spectroradiometer (MODIS) spacecraft over the Atlantic Ocean, *J. Geophys. Res.*, *110*, D10S12, doi:10.1029/2003JD004436.

Kawanishi, T., et al. (2003), The advanced microwave scanning radiometer for the earth observing system (AMSR-E), NASDA's contribution to the EOS for global energy and water cycle studies, *IEEE Transactions on Geoscience and Remote Sensing*, *vol. 41, issue 2*, 184–194, doi:10.1109/TGRS.2002.808331.

Kelly, K. A. (1991), The meandering Gulf Stream as seen by the Geosat altimeter: surface transport, position and velocity variance from 73° to 46°w, *Journal of Geophysical Research*, *96*, 16,721–16,738.

Kelly, K. A., and S. T. Gille (1990), Gulf Stream surface transport and statistics at 69°w from the Geosat altimeter, *Journal of Geophysical Research*, *95*, 3149–3161.

Key, E. L., and P. J. Minnett (2006), Implications of cloud forcing and feedbacks in the Southern Ocean, *Annals of Glaciology*, *44*, 15–22.

Kilpatrick, K. A., G. P. Podestá, and R. H. Evans (2001), Overview of the NOAA/NASA Pathfinder algorithm for Sea Surface Temperature and associated Matchup Database, *J. of Geophys. Res.*, *106*, 9179–9198.

Knobelspiesse, K. D., C. Pietras, G. S. Fargion, M. Wang, R. Frouin, M. A. Miller, A. Subramaniam, and W. M. Balch (2004), Maritime aerosol optical thickness measured by handheld sub photometers, *Remote Sens. Environ.*, *93*, 87–106.

Knoll, M., A. Hernández-Guerra, B. Lenz, F. López-Laazen, F. Machín, T. J. Müller, and G. Siedler (2002), The Eastern Boundary Current System between the Canary islands and the African coast, *Deep Sea Research II*, *49*(17), 3427–3440.

Köhl, A. (2005), Anomalies of Meridional Overturning: Mechanisms in the North Atlantic, *J. Physical Oceanography*, *35*(8), 1455–1472, doi:10.1175/JPO2767.1.

Köhl, A., D. Stammer, and B. Cornuelle (2007), Interannual to decadal changes in the ECCO global synthesis, *J. Phys. Oceanogr.*, *37*, 313–337.

Koren, I., Y. Kaufman, R. Washington, M. C. Todd, Y. Rudih, J. V. Martins, and D. Rosenfeld (2006), The Bodélé depression: a single sopot in Sahara that provides most of the ineral dust to the Amazon forest, *Environ. Res. Lett*, *1*, 014,005, doi: 10.1088/1748-9326/1/1/014005.

Kostianoy, A. G., and A. G. Zatsepin (1996), The west african coastal upwelling filaments and cross-frontal water exchange conditioned by them, *Journal of Marine Systems*, *7*(2-4), 349 – 359, doi:DOI:10.1016/0924-7963(95)00029-1, the Coastal Ocean in a Global Change Perspective.

Kundu, P. K. (1990), *Fluid Mechanics*, 638 pp., Academic Press.

Lacis, A., and J. E. Hansen (1974), A parameterization for the absorption of solar radiation in the earth's atmosphere, *J. Atmos. Sci.*, *31*, 118–133.

Landerer, F. W., J. H. Jungclaus, and J. Marotzke (2007), Ocean bottom pressure changes lead to a decreasing length-of-day in a warming climate, *Geophys. Res. Lett.*, *34*, L06,307, doi:10.1029/2006GL029106.

Large, W. G., J. C. McWilliams, and S. C. Doney (1994), Ocean vertical mixing: A review and a model with a nonlocal boundary layer parameterization, *Reviews of Geophysics*, *32*, 363–403.

Lau, K., and K. M. Kim (2007), Cooling of the Atlantic by Saharan dust, *Geophys. Res. Lett.*, *34*, L23,811, doi:10.1029/2007GL031538.

Lazar, A., I. Polo, S. Arnault, and G. Mainsant (2006), Kelvin waves activity in the eastern tropical atlantic, in *Proceedings of the Symposium on 15 Years of Progress in Radar Altimetry*, Venice, Italy (ESA SP-614, July 2006).

Li, F., A. M. Vogelmann, and V. Ramanathan (2004), Saharan Dust Aerosol Radiative Forcing Measured from Space, *J. Climate*, *17*, 2558–2571.

Lumpkin, R., and S. L. Garzoli (2005), Near-surface circulation in the Tropical Atlantic Ocean, *Deep Sea Research I*, *52*, 495–518.

Mahowald, N. M., and C. Luo (2003), A less dusty future?, *Geophys. Res. Lett.*, *30(17)*, 1903, doi:10.1029/2003GL017880.

Mahowald, N. M., A. Baker, G. Bergametti, N. Brooks, R. Duce, T. Jickells, N. Kubilay, J. Prospero, and I. Tegen (2005), Atmospheric global dust cycle and iron inputs to the ocean, *Global Biogeochemical Cycles*, *19*, GB4025, doi:10.1029/2004GB002402.

Marchesiello, P., and P. Estrade (2009), Eddy activity and mixing in upwelling systems: a comparative study of Northwest Africa and California regions, *International Journal of Earth Sciences*, *98*(2), 299–308, doi:10.1007/s00531-007-0235-6.

Marotzke, J., R. Giering, K. Zhang, D. Stammer, C. Hill, and T. Lee (1999), Construction of the adjoint MIT ocean general circulation model and application to Atlantic heat transport sensitivity, *J. Geophys. Res.*, *104(C12)*, 29,529–29,547.

Marshall, J., C. Hill, L. Perelman, and A. Adcroft (1997a), Hydrostatic, quasi-hydrostatic, and nonhydrostatic ocean modeling, *J. Geophys. Res.*, *102(C3)*, 5733–5752.

Marshall, J., A. Adcroft, C. Hill, L. Perelman, and C. Heisey (1997b), A finite-volume, incompressible Navier Stokes model for studies of the ocean on parallel computers, *J. Geophys. Res.*, *102*, 5753–5766.

Marshall, J., A. Adcroft, J. Campin, C. Hill, and A. White (2004), Atmosphere-Ocean Modeling Exploiting Fluid Isomorphisms, *Mon. Wea. Rev*, *132*, 2882–2894.

Martínez Avellaneda, N., N. Serra, P. Minnett, and D. Stammer (), Response of the eastern sub-tropical Atlantic SST to Saharan Dust: a modelling and observational study, *J. Geophys. Res.*, *submitted*.

Marzeion, B., A. Timmermann, R. Murtugudde, and F. Jin (2005), Biophysical Feedbacks in the Tropical Pacific, *J. Climate*, *18*, 58–70.

May, D. A., L. L. Stowe, J. D. Hawkins, and E. P. McClain (1992), A Correction for Saharan Dust Effects on Satellite Sea Surface Temperature Measurements, *J. Geophys. Res.*, *97(C3)*, 3611–3619.

Mazeika, P. A. (1967), Thermal domes in the eastern Atlantic Ocean, *Limnology and Oceanography*, *12*, 537–539.

Memery, L., M. Arhan, X. A. Alvarez-Salgado, M. J. Messias, H. Mercier, C. G. Castro, and A. F. Rios (2000), The water masses along the western boundary of the south and equatorial Atlantic, *Progress in Oceanography*, *47*, 69–98.

Menemenlis, D., and C. Wunsch (1997), Linearization of an oceanic general circulation model for data assimilation and climate studies, *J. Atmos. ocean Tech.*, *14*, 1420–1443.

Menemenlis, K., I. Fukomori, and T. Lee (2005), Using green's functions to calibrate an ocean general circulation model, *Mon. Weather Rev.*, *133*, 1224–1240.

Miller, R. L., and I. Tegen (1998), Climate Response to sol dust aerosol, *J. Clim.*, *11*, 3247–3267.

Miller, R. L., and I. Tegen (1999), Radiative forcing of a tropical direct circulation by mineral dust aerosol, *J. Clim. Sci.*, *56*, 2403–2433.

Mills, M. M., C. Ridame, M. Davey, J. LaRoche, and R. J. Geider (2004), Iron and phosphorus co-limit nitrogen fixation in the eastern tropical North Atlantic, *Nature*, *429*, 292–294, doi:10.1038/nature02550.

Minnett, P. J. (1999), The influence of solar zenith angle and cloud type on cloud radiative forcing at the surface in the Arctic, *Journal of Climate*, *12*, 147–158.

Molinari, R. L., and J. Morrison (1998), The separation of the Yucatan Current from the Campeche Bank and the intrusion of the loop current into the Gulf of Mexico, *Journal of Geophysical Research*, *93*, 10,645–10,654.

Moore, C. M., et al. (2009), Large-scale distribution of Atlantic nitrogen fixation controlled by iron availability, *Nature Geosci.*, doi:10.1038/ngeo667.

Morris, V., P. Clemente-Colón, E. J. N. R. Nalli, R. A. Armstrong, Y. Detrés, M. D. Goldberg, P. J. Minnett, and R. Lumpkin (2006), Measuring Trans-Atlantic Aerosol Transport From Africa, *EOS*, *87(50)*, 565.

Moulin, C., H. R. Gordon, R. M. Chomko, V. F. Banzon, and R. H. Evans (2001), Atmospheric correction of ocean color imagery through thick layers of Saharan dust, *Geophys. Res. Lett.*, *28*, 5–8.

Nalli, N. R., et al. (2005), Profile observations of the Saharan air layer during AEROSE 2004, *Geophys. Res. Lett.*, *32*, L05,815, doi:10.1029/2004GL022028.

Nalli, N. R., et al. (2006), Ship-based measurements for infrared sensor validation during Aerosol and Ocean Science Expedition 2004, *J. Geophys. Res.*, *111*, D09S04, doi:10.1029/2005JD006385.

O'Neill, L., D. B. Chelton, and S. Esbensen (2003), Observations of SST-Induced Perturbations of the Wind Stress Field over the Southern Ocean on Seasonal Timescales, *J. Climate*, *16*, 2340–2354, doi:10.1175/2780.1.

Osychny, V., and P. Cornillon (2004), Property of Rossby Waves in the North Atlantic Estimated from Satellite Data, *J. Phys. Oceanogr.*, *34*, 61–76, doi:10.1175/1520-0485(2004)034<0061:PORWIT>2.0.CO;2.

Pfister, G., R. L. McKenzie, J. B. Liley, A. Thomas, B. W. Forgan, and C. N. Long (2003), Cloud coverage based on all-sky imaging and its impact on surface solar irradiance, *Journal of Applied Meteorology*, *42*, 1421–1443.

Polito, P., and P. Cornillon (1997), Long baroclinic Rossby waves detected by TOPEX/POSEIDON, *J. Geophys. Res.*, *102(C2)*, 3215–3235.

Ponte, R. M. (1999), A preliminary model study of the large-scale seasonal cycle in borttom pressure over the global ocean, *J. Geophys. Res.*, *104*, 1289–1300.

Prospero, J. M., and T. N. Carlson (1981), Saharan air outbreaks over the tropical North Atlantic, *Pure Appl. Geophys.*, *119*, 677–691.

Prospero, J. M., P. Ginoux, O. Torres, S. E. Nicholson, and T. E. Gill (2002), Environmental characterization of global sources of atmospheric soil dust identified with the NIMBUS 7 Total Ozone Mapping Spectrometer (TOMS) absorbing aerosol product, *Rev. Geophys.*, *40(1)*, 1002, doi:10.1029/2000RG000095.

Ramanathan, V., et al. (2001), Indian ocean experiment: An integrated analysis of the climate forcing and effects of the great Indo-Asian haze, *J. Geophys. Res.*, *106*, 28,371–28,398.

Remer, L. A., Y. J. Kaufman, and R. G. Kleidman (2006), Comparison of Three Years of Terra and Aqua MODIS Aerosol Optical Thickness Over the Global Oceans, *IEEE Geosci. Remote Sens. Lett.*, *3(4)*, 537–540.

Remer, L. A., et al. (2005), The MODIS aerosol algorithm, product and validation, *J. Atmos. Sci.*, *62*, 947–973, doi:10.1175/JAS3385.1.

Roemmich, D., and C. Wunsch (1985), Two transatlantic sections: meridional circulation and heat flux in the subtropical North Atlantic Ocean, *Deep-Sea Res*, *32*, 619–664.

Sassen, K., P. J. DeMott, J. M. Prospero, and M. R. Poellot (2003), Saharan dust storms and indirect aerosol effects on clouds: CRYSTAL-FACE results, *Geophys. Res. Lett.*, *30(12)*, 1633, doi:10.1029/2003GL017371.

Schepanski, K., I. Tegen, and A. Macke (2009a), Saharan dust transport and deposition towards the Tropical Northern Atlantic, *Atmos. Chem. Phys.*, *9*, 1173–1189.

Schepanski, K., I. Tegen, M. C. Todd, B. Heinold, G. Bönisch, B. Laurent, and A. Macke (2009b), Meteorological processes forcing Saharan dust emission inferred from MSG-SEVIRI observations of subdaily dust source activation and numerical models, *J. Geophys. Res*, *114*, D10,201, doi:10.1029/2008JD010325.

Schmitz, W. J., Jr., and J. R. Luyten (1991), Spectral time scales for mid-latitude eddies, *J. Mar. Res.*, *49*, 75–105.

Schott, F. A., J. Fischer, and L. Stramma (1998), Transports and pathways of the upper-layer circulation in the western tropical Atlantic, *Journal of Physical Oceanography*, *28*(10), 1904–1928.

Schott, F. A., P. Brandt, M. Hamann, J. Fischer, and L. Stramma (2002), On the boundary flow off brazil at 5-10°s and its connetion to the interior tropical Atlantic, *Geophys. Res. Lett.*, *29*(17), 1840.

Schott, F. A., J. P. McCreary, and G. C. Johnson (2004), Shallow overturning circulation of the tropical -subtropical oceans, *Earth Climate: The Ocean-Atmosphere Interaction, Geophysical Monograph Series 147, AGU*, pp. 261–304.

Serra, N., R. Käse, A. Köhl, D. Stammer, and D. Quadfasel (2009), On the low-frequency phase relation between the Denmark Strait and the Faroe-Shetland Channel dense overflows, *Tellus A.*, *accepted*.

Smith, T. M., R. W. Reynolds, T. C. Peterson, and J. Lawrimore (2008), Improvements to NOAA's Historical Merged Land-Ocean Surface Temperature Analysis (1880-2006), *J. Climate*, *21*, 2283–2296, doi:10.1175/2007JCLI2100.1.

Smith, W., and D. T. Sandwell (1997), Global seafloor topography from satellite altimetry and ship depth sounding, *Science*, *277*, 195–196.

Stammer, D., and C. W. Böning (1996), Generation and Distribution of Mesoscale Eddies in the North Atlantic Ocean, in *The Warmwatersphere of the North Atlantic Ocean*, edited by W. Krauss, pp. 159–193, Gebrüder Borntraeger, Berlin, Stuttgart.

Stammer, D., F. J. Wentz, and C. Gentemann (2003), Validation of Microwave Sea Surface Temperature Measurements for Climate Purposes, *J. Clim.*, *16*, 73–87.

Stommel, H. (1958), *The Gulf Stream: A Physical and Dynamial Description*, 202 pp., University of California Press, Berkely and Los Angeles. Cambridge University Press, London.

Stramma, L., and T. Muller (1989), Some observations of the Azores Current and the North Equatorial Current, *Journal of Geophysical Research*, *94*, 3181–3186.

Stramma, L., J. Fischer, P. Brandt, and F. Schott (2003), Circulation, variability and near-equatorial meridional flow in the central tropical Atlantic, in *Interhemispheric Water Exchange in the Atlantic Ocean*, edited by G. J. Goni and P. Malanotte-Rizzoli, pp. 1–22, Elsevier, Amsterdam.

Sweeney, C., A. Gnanadesikan, S. M. Griffies, M. J. Harrison, A. J. Rosati, and B. L. Samuels (2005), Impacts of Shortwave Penetration Depth on Large-Scale Ocean Circulation and Heat Transport, *Journal of Physical Oceanography*, *35(6)*, 1103–1119.

Tegen, I., M. Werner, S. P. Harrison, and K. E. Kohfeld (2004), Relative importance of climate and land use in determining present and future global soil dust emission, *Geophys. Res. Lett.*, *31*, L05,105, doi:10.1029/2003GL019216.

Vázquez-Cuervo, J., E. Armstrong, and A. Harris (2004), The Effect of Aerosols and Clouds on the Retrieval of Infrared Sea Surface Temperatures, *J. Climate*, *17*, 3921–3933, doi:10.1175/1520-0442(2004)017<3921:TEOAAC>2.0.CO;2.

Vogelmann, A. M., P. J. Flatau, M. Szczodrak, K. M. Markowicz, and P. J. Minnett (2003), Observations of large aerosol infrared forcing at the surface, *Geophys. Res. Lett.*, *30*(12), 1655, doi:10.1029/2002GL01682.

Volpe, G., V. F. Banzon, R. H. Evans, R. Santoleri, A. J. Mariano, and R. Sciarra (2009), Satellite observations of the impact of dust in a low-nutrient, low chlorophyll region: Fertilization or artifact?, *Global Biogeochemical Cycles*, *23*, GB3007, doi:10.1029/2008GB003216.

Washington, R., M. Todd, N. J. Middleton, and A. S. Goudie (2003), Dust-storm source areas determined by the Total Ozone Monitoring Spectrometer and surface observations, *Annals Assoc. Am. Geogr.*, *93*, 297–313.

Wentz, F. J. (1998), Algorithm theoretical basis document: AMSR ocean algorithm, *Remote Sensing Systems Tech. Rep. 110398*, *Santa Rosa, CA*, 28 pp.

Wentz, F. J., C. Gentemann, D. Smith, and D. Chelton (2000), Satellite Measurements of Sea Surface Temperature Through Clouds, *Science*, *288*, 847–850.

Won, J.-G., S.-C. Yoon, S.-W. Kim, A. Jefferson, E. G. Dutton, and B. N. Holben (2004), Estimations of direct radiative forcing of asian dust aerosols with sun/sky radiometer and lidar measurements at Gosan, Korea., *J. of the Met. Soc. of Japan*, *82*, 115–130.

Wu, L. (2007), Impact of Saharan air layer on hurricane peak intensity, *Geophys. Res. Lett.*, *34*, L09,802, doi:10.1029/2007GL029564.

Wunsch, C. (1996), *The ocean circulation inverse problem*, 442 pp., Cambridge Univ. Press, New York.

Wunsch, C. (2007), On measuring mass transport, variability in an eddy-filled ocean, *Nat. Geosci.*, *1*, 165–168.

Wunsch, C., and D. Stammer (1997), Atmospheric Loading and the Oceanic "Inverted Barometer" Effect, *Rev. Geophys.*, *35(1)*, 79–107.

Yoon, S.-C., J.-G. Won, A. H. Omar, S.-W. Kim, and B.-J. Sohn (2005), Estimation of the radiative forcing by key aerosol types in worldwide locations using a column model and AERONET data, *Atm. Environ.*, *39*, 6620–6630.

Yoshioka, M., N. Mahowald, A. Conley, W. Collins, D. Fillmore, C. Zender, and D. Coleman (2007), Impact of Desert Dust Radiative Forcing on Sahel Precipitation: Relative Importance of Dust Compared to Sea Surface Temperature Variations, Vegetation Changes, and Greenhouse Gas Warming, *J. Climate*, *20*, 1445–1467.

Zhu, A., V. Ramanathan, F. Li, and D. Kim (2007), Dust plumes over the Pacific, Indian, and Atlantic oceans: Climatology and radiative impact, *J. Geophys. Res.*, *112*, D1620, doi:10.1029/2007JD008427.

Zimmerman, J. C. (1981), Sun-pointing programs and their accuracy. SAND81 -0761, *Tech. rep.*, Experimental Systems Operation Division 4721,Sandia National Laboratory, Albuquerque, NM, Available from National Technical Information Service, U.S. Department of Commerce, Springfield, VA 22161.

Acknowledgments

I would like to thank my advisor Detlef Stammer for his support during my Ph.D. studies. Thanks for the infinite patience, for encouraging me to publish, for all the help, and for always having had time for me.

Thanks to Nuno Serra for making the corrections of most of this thesis, for sharing his scripts, for always motivating me with science: thanks for all your amazing help!

Thanks to Armin Köhl, Peter Minnett, Ina Tegen, Johannes Quaas, Steffen Kine and Jochem Marotzke for several valuable discussions and suggestions.

Thanks goes to the NOAA Center for Atmospheric Sciences (NCAS) at Howard University Washington, D. C., and the University of Puerto Rico, Mayagüez, for providing the Microtops AOD and CTD data from the AEROSE-I cruise. Bill Large and Steven Yeager provided the one-dimensional version of the KPP model. Axel Cholewa and Armin Köhl did the German translation of the Abstract. Thanks to the IT support group of CIS and DKRZ. This work was supported through the BMBF project SOPRAN, TPSTA410/7-1, and partly through the International Max Planck Research School (IMPRS) of the University of Hamburg and the Max-Planck-Institution for Meteorology.

Thanks to my colleagues from the Ocean Modeling and Remote Sensing group of the IFM for their support and encouragement.

Many thanks to Conni Kampmann, Antje Weitz and Karin Ziemann-Cohrs for always having had time to help and to listen.

Thanks to Alberto Piola for his useful advice and help, and for always calming me down.

Thanks to my friends Gunnar, Marin, Gabi, Luca, Elías, Daniela, Ingrid, Alvaro, Miren, Luis, Tomas, Jordi, Mario, Steffen and Nikolay, for making my stay in Hamburg much more fun and for their emotional support.

Thanks to my friends Anahí, Andrea, Sandra, Sofía, Virna and Uriel for always having had something nice to say to me to cheer me up. Gracias por estar.

Thanks to Marcos for always having made some disgusting acid comment that would cheer me up. Thanks for making such a difference in my life in Hamburg.

Thank you Matt, for your everyday support and love and for taking care of me. Thanks for your amazing good mood and patience, specially during the thesis writing stage.

I would have to add an extra chapter to be able to express my gratitude to María Paz. Thanks Mer, for being such a good friend, for not letting me giving up, in many ways, and for never being condescending. This was fun, I could not imagine this present without you being in my life.

Thanks to my siblings Darío and Diana, for their understanding and support during my leave and during these years in Hamburg. Thanks for shortening the distance.

Thanks to my mum Mary and my dad Eloy for all those long talks on the phone, for helping me not to loose focus, for coming to visit, for all their love. Thank you for all your sacrifice that brought me here and made this Ph.D. possible.